博士論文
(Ph.D. Thesis)

A Study on Intelligent Boundary Detection with Application to Medical Images
(知的境界線抽出法と その医用画像への応用に関する研究)

平成27年3月
(March 2015)

SYAIFUL ANAM

山口大学大学院理工学研究科
Yamaguchi University
Graduate School of Science and Engineering

YAMAGUCHI UNIVERSITY
GRADUATE SCHOOL OF SCIENCE AND ENGINEERING

Ph.D Thesis

A Study on Intelligent Boundary Detection with Application to Medical Images

Specialty: Information and System Science

by

SYAIFUL ANAM
ADVISOR : Prof. EIJI UCHINO
March 2015

Committee Members :
Prof. EIJI UCHINO - Graduate School of Science and Engineering
Prof. KOJI NOZAKI - Graduate School of Science and Engineering
Prof. KENTA FUJISAWA - Graduate School of Science and Engineering
Prof. KOJI WAKITA - Graduate School of Science and Engineering
Associate Prof. NORIAKI SUETAKE - Graduate School of Science and Engineering

Ph.D Thesis

A Study on Intelligent Boundary Detection with Application to Medical Images

Specialty: Information and System Science

by

SYAIFUL ANAM

A dissertation submitted to
the Graduate School of Science and Engineering of Yamaguchi University
in partial fulfilment of requirement for the degree of Doctor of Philosophy

Advisor: Prof. EIJI UCHINO

Committee Members :
Prof. EIJI UCHINO
Prof. KOJI NOZAKI
Prof. KENTA FUJISAWA
Prof. KOJI WAKITA
Associate Prof. NORIAKI SUETAKE

YAMAGUCHI UNIVERSITY
GRADUATE SCHOOL OF SCIENCE AND ENGINEERING

Acknowledgements

Achieving a Ph.D in Japan has been my dream since I got master degree. Pursuing a Ph.D. project is both a painful and enjoyable experience. It is just like climbing a high peak, step by step, accompanied by bitterness, hardships, frustration, encouragement and trust, and with so many kind people's help. All praise and glory to almighty God who gave me the courage and patience to carry out the Ph.D project. This Ph.D. thesis appears in its current form due to the support, assistance and guidance of many people. Though it will not be enough to express my gratitude in words to all those people who helped me, I would still like to give my many thanks to all these people.

First of all, I would like to give my sincere thanks to my supervisor, Uchino Sensei, who accepted me as his Ph.D. student. Thereafter, he offered me so much advice, patiently supervising me, and always guiding me in the right direction. I have learned a lot from him, and without his help I could not have finished my Ph.D. thesis successfully.

Secondly, I would like to thank to Suetake Sensei who gave me much advice. He also supported me to finish my Ph.D degree.

I also appreciate the advice of the committee members, Prof. Eiji Uchino, Prof. Koji Nozaki, Prof. Kenta Fujisawa, Prof. Koji Wakita and Associate Prof. Noriaki Suetake for their critical comments, which enabled me to notice the weaknesses in my Ph.D. thesis and make the necessary improvements according to their comments.

During my research, Mr. Misawa and Mr. Tokunaga offered me a lot of friendly help. They transferred to me their research links and recommended the necessary readings for pursuing Ph.D. research. Our conversations enlightened my way of thinking, and so I would like to give my sincere thanks to Mr. Misawa and Mr. Tokunaga for their generous help.

I also would like to thank Ms. Beka, Ms. Joice, Mr. Markus and Ms. Rina. In the last stage of my journals, conference papers and Ph.D. thesis, they helped me correct grammar mistakes in my journals, conference papers, Ph.D. thesis, and suggested possible improvements. They also helped enable me to present my journals, conference papers and Ph.D. thesis more fluently and clearly in English. It is not sufficient to express my gratitude with only a few words.

Thanks are due to all staff of Yamaguchi University who help me since I am studying at Yamaguchi University. They always serve me with friendly attitudes and patiently.

My sincere thanks go to all the organizations, who gave me their indispensable generous sponsoring, including the Directorate General of Higher Education (DGHE) postgraduate scholarship of Indonesia, the Iizuka Research and Development Organization under the Project No. 24102, and the Grant-in-Aid for Scientific Research (B) of the Japan Society for Promotion of Science under the Contract No. 23300086. The DGHE postgraduate scholarship of Indonesia gave a scholarship to support my stay at Yamaguchi University, Japan. The DGHE postgraduate scholarship has helped me to realize my dream to study abroad. The Iizuka Research and Development Organization and the Grant-in-Aid for Scientific Research (B) of the Japan Society for Promotion of Science supported finance for these researches and publication in the international conferences and the international journals. Without their support and financial help, it would not have been

possible for me to pursue and to complete this Ph.D. project successfully.

All members of the information science laboratory, Yamaguchi University and all my friends have helped and supported me during my study at university Yamaguchi. Without your kind assistance, I could not finish my study smoothly in Japan. Especially, Mr. Tanaka, Mr. Miwa, Mr. Nakao, Mr. Kubosaka, Mr. Furukawa, Mr. Tohma, Mr. Yamada, Mr. Fujita, Mr. Shigenaga, Mr. Kuong and Mr. Inudzuka have helped and taught me, hence, I would like to thank them.

Finally, I am very grateful for my mother. Her understanding and her love encouraged me to work hard and to continue pursuing a Ph.D. project abroad. Her firm and kind-hearted personality has affected me to be steadfast and never to bend to difficulty. She always lets me know that she is proud of me, which motivates me to work harder and do my best.

Yamaguchi University
March 2015

SYAIFUL ANAM

Abstract

Medical imaging has developed into one of the most important fields within scientific imaging for computerized medical image visualization and computer-aided diagnosis. Medical image analysis is needed to provide invaluable information for diagnosing diseases. Image boundary detection is one of the most crucial steps in the medical image analysis. Since medical images contain much noise, it is difficult to distinguish the exact boundary of object from noise. Manual boundary detection is very time-consuming and the results suffer from intra-observer and inter-observer variability. For those reasons, medical images strongly require a sophisticated method that enhances visual interpretation. An automatic boundary detection of tissues with high accuracy is also required to provide information for diagnosis diseases and treatment.

Level set method has been widely applied for detecting image boundaries. It has several advantages over other segmentation methods. However, the level set method cannot work well to detect the medical image boundaries, because the medical images tend to contain heavy noise. The Perona-Malik diffusion (PMD) filter is a noise reduction method known for an effective edge-preserved smoothing method. However, when the normal PMD filter is applied to some medical images, the boundary cannot be preserved in several areas.

In this paper, the fuzzy inference is applied because the fuzzy inference can handle the problems with imprecise, noisy, in-consistent and incomplete data set. The parameter tuning of the membership functions (MSFs) of the fuzzy inference can be regarded as an optimization problem. Particle swarm optimization (PSO) is especially useful when the other optimization techniques such as the gradient descent method are not applicable. This paper proposes the intelligent boundary detection methods for the medical images.

Chapter 1 is an introduction.

Chapter 2 presents an overview of the intravascular ultrasound (IVUS) technology and the hand bone radiograph. Chapter 2 also presents the review of the previous methods related to the proposed method, i.e., PMD filter, image separability, texture analysis, level set method, fuzzy inference and PSO.

Chapter 3 presents a boundary detection method by combining PSO and Takagi-Sugeno (T-S) fuzzy inference for coronary plaque in IVUS image. To obtain the search area, the seed points are placed by heuristic rules. The parameters of the membership functions (MSFs) are tuned by using PSO. After tuning the parameters of MSFs, the T-S fuzzy inference is applied to approximate the coronary plaque boundaries by using the statistical discriminant measures (image separability) in

the search area. After the experiments, it has been found that the proposed method gives better performance than the previous works and the gradient descent method in terms of the calculation accuracy. Additionally, the proposed method works automatically, i.e., it does not need any set of the training data, the seed points, nor the initial areas which had to be given manually in the conventional methods. However, this method has weakness. If the seed points are placed in the wrong positions, the accuracy decreases. The boundaries cannot be preserved at some areas after applying the normal PMD filter.

Chapter 4 describes the modification of PMD filter in order to improve the performance of the normal one in Chapter 3. The PMD filter is modified by considering the plaque direction in the IVUS image. The method in Chapter 3 requires the seed points which affect the accuracy of boundary detection. For this reason, in Chapter 4 a hybrid method based on the modified level set method and the T-S fuzzy inference is proposed for a coronary plaque boundary detection. This method doesn't require any seed points. The Gaussian filter in the level set method is replaced by the modified PMD filter, and the gradient of image is replaced by the image separability for calculating the speed function of the modified level set method. The method in Chapter 4 considers the guide wire shadow, which was not considered in Chapter 3. The plaque boundaries hided by the guide wire shadow are inferred by the T-S fuzzy inference. They are calculated by the information obtained by the modified level set method. The present method was compared with the previous methods and the method in Chapter 3. The boundary detection accuracy of the present method was significantly better.

Chapter 5 describes the modified level set method for a hand bone radiograph boundary detection. Two points in the level set method are modified. The first point is on the filtering. The normal PMD filter is employed to replace the Gaussian filter. The second point is on the speed function of the level set method, which is modified to improve the motion of the level set contour. An entropy method-based texture analysis is further employed for preprocessing. The normalization of the gradient of image and the exponent function are employed for the calculation of the speed function of the modified level set method. After evaluating the experimental results, it is found that the accuracy of the proposed method is better than that of the conventional methods.

Chapter 6 contains the conclusion and future work for the thesis.

Contents

List of Figures

List of Tables

Chapter 1

Introduction

1.1 Motivation

Medical imaging is a valuable tool in medicine. It has developed into one of the most important fields within scientific imaging for computerized medical image visualization and computer-aided diagnosis [1]. Medical imaging is a part of the biological imaging and incorporates radiology which uses imaging technologies, e.g., computed tomography (CT), positron emission tomography (PET), magnetic resonance imaging (MRI), ultrasound imaging (US) and other techniques. Imaging technologies provide more effective information about the anatomy of the human body. Medical imaging can visualize internal structures hidden by the skin and bones for diagnosing and treating diseases. It also builds a database of normal anatomy and physiology to make it possible to identify abnormalities. These technologies become more critical in disease diagnosis and treatment planning.

Medical imaging technologies have been widely applied to various medical procedures. Compared to traditional medical diagnosis, they provide non-invasive yet powerful means to investigate the internal structures and activities of human bodies. With the help of imaging technologies, doctors can obtain multi-dimensional information such as 2-D slices, 3-D volumetric images and videos of regions of interest (ROI), which facilitates the performance of both qualitative and quantitative analysis. This analysis provides invaluable information for diagnosing and treating diseases as well as surgical planning.

However, medical images need to be analyzed to provide invaluable information. Medical image analysis is a wide concept that includes several processing and analysis methods applied to a number of different imaging modalities [2]. Generally, image analysis can be divided into different steps such as: image enhancement, segmentation, registration, quantification and classification.

One of the important steps in image analysis is image segmentation. Image segmentation is a process of partitioning an image into multiple segments. It is used to divide an image into two or several different regions of interest. The image segmentation is used to simplify and/or change the representation of an image into

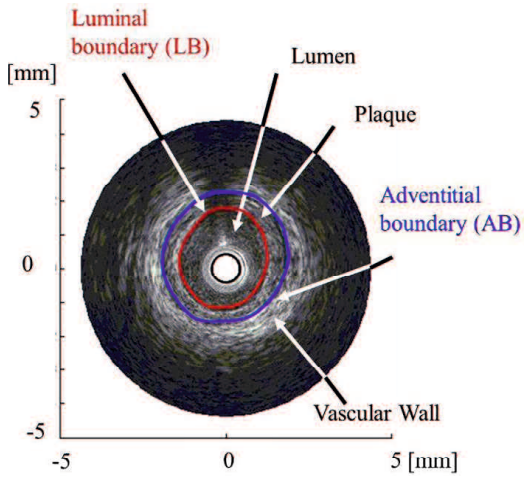

Figure 1.1: Coronary plaque segmentation (coronary plaque boundary detection) in the IVUS image.

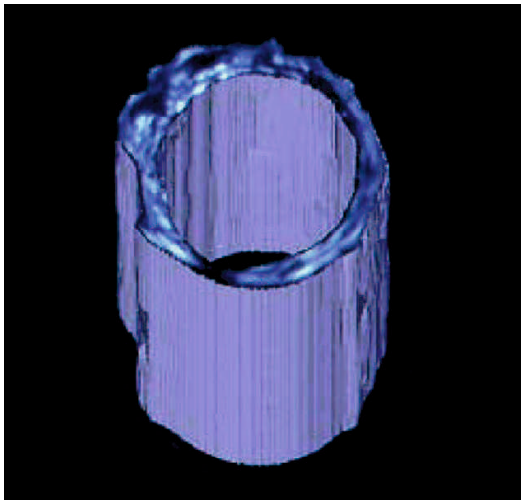

Figure 1.2: Coronary plaque visualization in 3 dimensions (http://electronicimaging.spiedigitallibrary.org/).

another form that is more significant. It makes an image easier to be analysed. The human organ segmentation of a medical image is beneficial to many areas of medicine, including measurements of tissue volume, computer-guided surgery, diagnosis, treatment planning, and research and teaching [3].

Medical image segmentation is also a crucial step that determines the final result of the entire application, since the rest of the analysis fully relies on the data from this step. One of the examples of the medical image segmentation is a construction of 3-D volumetric model from a series of medical images. The segmentation in 2-D images should be as accurate as possible, otherwise the volume of the reconstructed model would be incorrect, and visualization of this model would be meaningless.

One common type of image segmentation method is the boundary detection method. It plays a fundamental role in image analysis and computer vision. Boundary detection of an image results are important information for the analysis of image interpretation [4]. Image boundaries provide a clear outline or shape of an object. Since the boundary of a medical image provides valuable information for further medical image analysis and interpretation tasks, the correct medical image boundary detection has become one of the most important and necessary tasks in medical image processing.

Medical image boundary detection has been applied in various areas. In the application of coronary plaque diagnosis [5], the coronary plaque segmentation in intravascular ultrasound (IVUS) image in consecutive slices can be used for reconstructing the 3-D volumetric models of coronary artery. By making a model of the inside of the coronary vessel, doctors can pinpoint the narrowing blood vessel problem and assess the risk quantitatively. To obtain an IVUS image segmentation

Figure 1.3: Bone segmentation (bone boundary detection) in hand radiograph.

for the quantitative assessment of the compositions of coronary plaque, the luminal boundary (LB) and the adventitial boundary (AB) of the coronary plaque need to be detected and evaluated precisely as shown in Figure 1.1. Visualization of the coronary artery in 3 dimensions can further aid doctors to make an assessment of a coronary plaque which is very important for a diagnosis of acute coronary syndrome (ACS) as shown in Figure 1.2.

In the application of an arthritis diagnosis, an automatic boundary detection of the hand bones radiograph is an important process to detect bone erosion and to analyse bone density. To give the arthritis diagnosis, a radiograph of the patient's hand is taken [6], and it is analyzed to detect bone erosion caused by arthritis. The boundaries of the hand bones radiograph, which is shown in Figure 1.3, need to be detected for the hand bone radiograph analysis. The hand bones radiograph analysis is needed for diagnosing and treating arthritis.

Manual boundary detection is very time-consuming and the results may not be reproducible or suffer from intra-observer and inter-observer variability. This is not only because the boundary of image is difficult to be recognized, but also because the number of images to be processed and evaluated by a medical doctor is very large. In real life application, medical images also contain object boundaries, object shadows, and noise. Therefore, the medical doctors may find it difficult to distinguish the exact boundary from noise or trivial geometric features. For these reasons, the medical images strongly require sophisticated image processing methods that enhance visual interpretation, and image analysis methods that provide an automatic boundary detection of tissues, measurement and characterization with high accuracy.

Several boundary detection methods that have been proposed and applied to medical images. These methods however have limitations and cannot work well when applied to medical images. Several algorithms have been applied to the coronary

plaque boundary have been proposed in the references [5, 7, 8, 9, 10, 11, 12]. Methods in the references [7, 8, 9, 10, 11] need an initial area and a set of training data which are manually segmented by an expert.

Active contour models have been widely applied for detecting image boundaries [13, 14, 15, 16, 17, 18, 19]. They detect image boundaries based on energy optimization. The active contour models have several advantages over the conventional image segmentation methods such as gradient-based algorithm (Sobel algorithm, Prewitt algorithm and Laplacian of Gaussian operator), and template-based algorithm [20]. The first advantage of the active contour models is that they can achieve sub-pixel accuracy of object boundaries [13]. The second advantage is that the active contour models can be easily formulated under a principled energy minimization framework, and allow incorporation of various prior knowledge, such as shape and intensity distribution, for robust segmentation [17]. The third advantage is that they can give smooth and closed contours as a segmentation result, which is necessary for many applications.

Active contour models can be classified into two categories, i.e., the classical snakes and the level set method. The level set method has been applied successfully in many cases in image segmentation. It has several advantages over other segmentation methods such as the snake method, region growth and thresholding. The advantages of the level set method over the snake method are that the curve may break or merge naturally during an evolution that causes topological changes are automatically handled.

However, the level set method cannot work well to detect medical image boundaries, because medical images tend to contain heavy noise. It often leads to either a complete breakdown or a premature termination in the curve evolution process, resulting in unsatisfactory results. This is because the speed function cannot properly detect the boundary and its detected boundary is dull even after filtering. The Gaussian filter is used for reducing noise in the standard level set method. It is a high possibility that the image boundary becomes dull after applying the Gaussian filter.

Therefore, a noise reduction and an edge enhancement of the medical image are very important tasks in the case of preprocessing of medical images. As the representative conventional noise reduction methods, the median filters [21], morphology analysis [22], bilateral filters [23] are well-known, but at the same time the image boundary also becomes unexpectedly dull by applying these methods.

Above all these methods, the Perona-Malik diffusion (PMD) filter [24] is known as an effective edge-preserved smoothing method and is broadly used in the references [9, 11, 12, 25, 26, 27, 28]. However, when the normal PMD filter is applied to medical images such as an IVUS image [5, 11, 12, 28], the coronary plaque boundary cannot be preserved in several areas.

Medical image boundaries also are often missing in several areas. In this paper, the fuzzy inference will be applied because it can handle problems with imprecise, noisy, in-consistent and incomplete data sets [29]. Additionally, the Takagi-Sugeno

(T-S) fuzzy inference [30] has been successfully applied in many areas and has several advantages over the conventional methods in the boundary detection of image [31].

The parameter tuning of the membership functions (MSFs) of the fuzzy inference can be regarded as an optimization problem. However, this optimization was not done in the conventional method [5, 11, 12]. Particle swarm optimization (PSO) [32] is especially useful when other techniques such as gradient descent or direct analytical discovery are not applicable [33].

Based on the problem of boundary detection in medical images, this paper proposes the intelligent boundary detection methods for medical images which are constructed by taking advantages of the set of existing image processing methods, and modifying and combining several image processing methods. Chapter 3 presents a boundary detection method by combining PSO and T-S fuzzy inference for coronary plaque in IVUS image. Chapter 4 proposes a modified PMD filter, and a hybrid method based on modified level set method and the T-S fuzzy inference for coronary plaque boundary detection. Chapter 5 presents modified level set method for hand bone radiograph boundary detection. The proposed methods are applied to several medical images. The kinds of medical images that have been used are:

1. IVUS image.

   IVUS imaging [34] is a unique imaging clinic tool that provides a real time cross-sectional inside view of a coronary artery in a living individual and thus, allows a complete study of its morphology; such as the arterial wall, lumen and plaque. The IVUS method helps diagnosis and treatment of ACS, so long as a tissue characterization and plaque volume calculation are available. For the first step in a diagnosis of ACS, the inner and outer coronary plaque boundaries in the IVUS image have to be detected for evaluating the quantitative assessment of the coronary plaque compositions.

2. Hand bone radiograph.

   The hand bone radiograph is the gold standard for an assessment of joint damage in arthritis [35]. The hand bone radiograph of Figure 1.3 is used not only for the initial diagnosis but also for the monitoring of disease progression and assessment of the therapeutic effect of various drugs. The boundaries of the hand bones need to be detected first for the hand bone radiograph analysis.

They have been selected to apply to proposed methods in analysis and display, in the hope that the methodologies may be transferred to other applications.

1.2 Bright spots

The Ph.D thesis is organized as follows:

1. Bright spots in Chapter 2.

Chapter 2 presents an overview of the IVUS technology and the hand bone radiograph. Chapter 2 also presents the review of the previous methods related to the proposed method.

2. Bright spots in Chapter 3.

   Chapter 3 presents a boundary detection method for coronary plaque in IVUS image. This method combines PSO and the T-S fuzzy inference. This method needs seed points. Those points are placed by heuristic rule.

3. Bright spots in Chapter 4.

   Chapter 4 presents a modified PMD filter and hybrid method for detecting coronary plaque boundary. The hybrid method is a combination between the modified level set method and the T-S fuzzy inference. This method doesn't require seed points, while the method in Chapter 3 requires seed points. The guide wire shadow is considered here, while it is not considered in Chapter 3. The PMD filter is modified by considering the plaque boundary direction, while the normal PMD filter in Chapter 3 doesn't consider the plaque boundary direction.

4. Bright spots in Chapter 5.

   Chapter 5 presents texture analysis and modified level set method for automatic detection of bone boundaries in hand radiographs. The erosion operation and an entropy method-based texture analysis method are used for preprocessing. The speed function of the modified level set method is calculated by using the normalization of the gradient of image and the exponent function, but the speed function of the modified level set method in Chapter 4 is calculated by using the separability of image.

5. Bright spots in Chapter 6.

   Chapter 6 contains the conclusion and future work for the thesis.

Chapter 2

Preparation of Knowledge

2.1 Medical imaging and disease diagnosis

Medical imaging refers to the techniques and processes used to create images of the human body for various clinical purposes, such as medical procedures and diagnosis or medical science, including the study of normal anatomy and function. With the growth of computer and image technology, medical imaging has greatly influenced medical science.

The medical imaging technologies produce medical images which play an important role in clinical diagnosis, therapy, teaching, and researching etc. Medical images are often used to visualize anatomical structures of the body for the diagnosis of diseases. The proper and correct diagnosis of diseases are a primary necessity before the treatment. However, the medical images cannot be used directly. Therefore, image processing is needed to enhance and to analyse the medical images to provide valuable information for the diagnosis of diseases and treatment of diseases. Since the quality of medical imaging affects the proper and correct diagnosis of diseases, an advanced medical image processing is strongly required.

2.1.1 Coronary artery disease and intravascular ultrasound method

Coronary artery disease is the most common type of heart disease and cause of heart attacks. This disease is caused by plaque building up along the inner walls of the arteries of the heart, which narrows the arteries and reduces blood flow to the heart.

Acute coronary syndromes (ACS) are the consequence of the development of coronary artery disease, which is the leading cause of death worldwide [36]. ACS is a coronary artery disease, which is caused when arteries that supply oxygen-rich blood to heart muscle become narrowed or hardened. This chapter is divided into two sections; the coronary artery diseases and the IVUS method which is a method for examining a coronary artery disease.

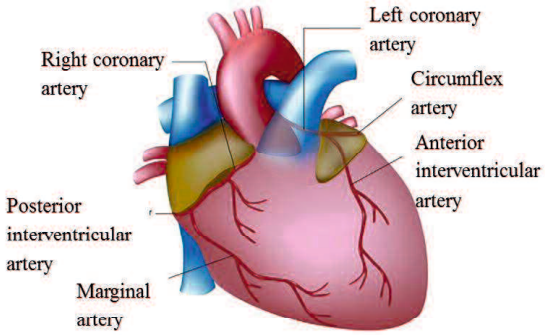

Figure 2.1: Coronary arteries of the heart http://www.jamesdisabilitylaw.com).

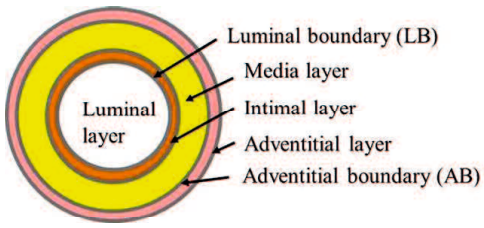

Figure 2.2: Coronary artery structure.

2.1.1.1 Coronary artery disease

2.1.1.1.1 Coronary artery

Coronary arteries are vessels that cover the surface of the heart, as shown in Figure 2.1. They are responsible for supplying oxygen-rich blood to the heart muscle. Like all other tissues in the body, the heart muscle needs oxygen rich blood to keep the heart muscle working and healthy, and oxygen-depleted blood must be carried away. The coronary arteries run along the outside of the heart and have small branches that dive into the heart muscle to bring blood [37].

Coronary arteries are mainly divided into the left main and right coronary arteries. The left main coronary artery, which divides into the anterior interventricular artery and the circumflex artery, supplies blood to the left ventricle and left atrium. The right coronary artery, which divides into the posterior interventricular artery and marginal arteries, supplies blood to the right ventricle, right atrium, and the sinoatrial and atrioventricular nodes, which regulate the heart rhythm.

Since coronary arteries deliver blood to the heart muscle, any coronary artery disorder or disease can pose serious implications by reducing the flow of oxygen and nutrients to the heart muscle, which may lead to a heart attack and possibly death.

The basic organization of the coronary arterial wall is similar to all arteries in that three concentric layers, as shown in Figure 2.2. The image shows an inner (luminal) layer, the intima (tunica intima, intimal layer); a middle layer, the media (tunica media, media layer); and an outer (external) layer, the adventitia (tunica adventitia, adventitial layer). The luminal diameter of the majors coronary artery in adults range as follows: left main, 2.0-5.5 mm (mean 4 mm); left anterior descending, 2.0-5.0 mm (mean 3.6 mm); left circumflex, 1.5-5.5 mm (mean 3.0 mm); and right, 1.5-5.5 mm (mean 3.2 mm) [38].

2.1.1.1.2 Acute coronary syndrome

Coronary artery disease is characterized by the accumulation of fatty deposits along

the innermost layer of the coronary arteries. The fatty deposits may develop in childhood and continue to thicken and enlarge throughout the life span. This thickening, called atherosclerosis, narrows the arteries and can decrease or block the flow of blood to the heart.

Atherosclerosis, which is a build up of plaque in the inner lining of an artery causing it to narrow or become blocked, is the most common cause of heart disease as shown in Figure 2.3. It is characterized by the thickening, hardening, and loss of elasticity of the inner arterial walls [39]. The plaque restricts the flow of blood and the delivery of oxygen to the heart.

The components of plaques are lipid components and other material, which is built up and accumulated inside the coronary artery. The vulnerable plaque that ruptures is usually described as having a lipid core with a fibrous cap as shown in Figure 2.4, with the thinning of the cap and inflammation in the shoulder region of the plaque. The progressive accumulation of plaque within the artery wall over decades is the setup for vulnerable plaque which, in turn, leads to heart attack and stenosis of the artery. If plaque from the wall of a coronary artery ruptures, a blood clot can form at the site of the rupture. If the clot is large enough to block the vessel and critically reduces blood flow, the heart muscle can be damaged. This process is known as thrombosis.

All large and medium-sized arteries, including the coronary, carotid, and cerebral arteries, the aorta, its branches, and major arteries of the extremities can be affected by atherosclerosis [36]. Atherosclerosis can lead to ACS. ACS occurs when a blood clot blocks a coronary artery, reducing blood supply to the heart.

ACS can be caused by a variety of risk factors, including a family history of heart attack or unstable angina. High cholesterol, high blood pressure, diabetes and tobacco use also can contribute to the buildup of plaque in the arteries which may lead to atherosclerosis. ACS describes any condition characterized by signs and symptoms of sudden myocardial ischemia-a sudden reduction in blood flow to the heart [40].

2.1.1.2 Intravascular ultrasound method

The ultrasound technology has many applications in medical diagnosis. One of the applications of the ultrasound technology is to see inside a coronary artery, which is known as intravascular ultrasound (IVUS) method. The IVUS method is a catheter based medical imaging technique that produces cross-sectional images of blood vessel and is particularly useful for the diagnosis of atherosclerosis. IVUS method is further used in the coronary arteries to observe within the blood vessel all the way through to the surrounding blood columns, visualizing the coronary plaque. It determines the amount of plaque built up at any particular point in the coronary artery in living individual.

Several characteristics inherent to ultrasound imaging offer potential advantages in the evaluation of coronary disease compared to angiography. Angiography is only

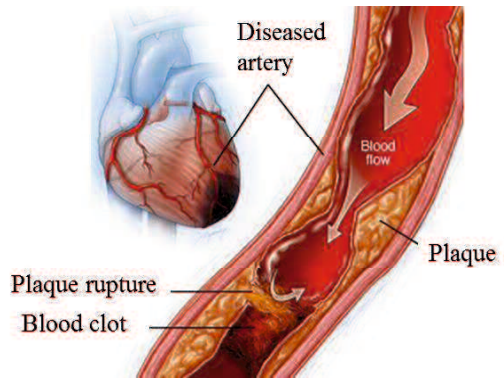

Figure 2.3: Coronary artery diseases caused by atherosclerosis (http://www.examiner.com/).

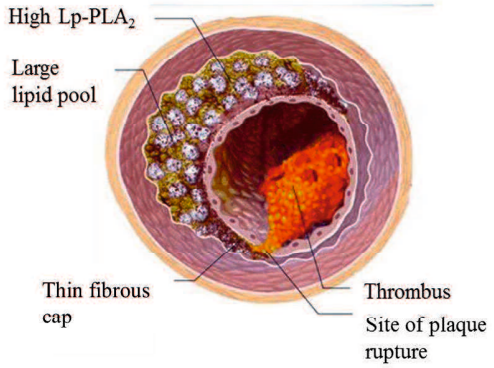

Figure 2.4: Ruptured plaque in cross-sectional coronary artery (http://www.sec.gov/).

able to visualize the vessel in two surfaces and is also not able to visualize inside coronary vessels. Where as ultrasound not only allows a precise assessment of vessel but also enables visualization and measurement of the tomographic of lumen area and plaque size [41].

2.1.1.2.1 Ultrasound technology

Ultrasounds (US) are pressure waves with frequency f beyond the limit of human hearing ($f > 20$ KHz) propagating in a medium. In medicine, US are used in both diagnostic (ultrasonography) and therapeutic (focused ultrasound surgery) applications.

In the first case, US are used to penetrate a medium and measure the reflection signature. It reveals details about the inner structure of the medium. In the second case, US are used to supply focused energy to tissues. In nature, each medium can be considered as having been formed by a large number of particles, normally quiet, and when perturbed by an US wave start to oscillate around their resting position. US in fact, transfer mechanical energy through the medium they are travelling in, alternatively compressing and decompressing it [42].

US are generated by US transducer able to both produce and receive pressure waves. When US propagates through a medium, it finds an interface of two different tissues. It is in part reflected and returns towards the source with a reduced magnitude and a temporal delay. This phenomenon is called echo and it is common to each acoustic wave. An ultrasound image is then created by processing the echoes returning to the US transducer which comes from various depths of the body upon emission of an ultrasound pulse of a specific frequency. In most of the ultrasonography application, the ultrasonic transducer is applied to the surface of the body. Whilst in an invasive application, like IVUS, it is directly put into the artery [43].

2.1.1.2.2 Intravascular ultrasound image reconstruction from radio frequency data

An IVUS image displays tomography from a cross-sectional perspective. This facilitates direct measurements of lumen dimensions, including minimum and maximum diameter, and a cross-sectional area, as well as the characterization of atheroma size, plaque distribution and lesion composition. The IVUS image generally consists of three layers around the lumen: the intima, the media and the adventitia. Estimation of the vessel area is based on the measurements of the media-adventitia border, and plaque area is derived by subtracting lumen area from vessel area. Although invasive, the inside-out imaging of the arterial wall is extremely important in coronary interventions where there is limited access to the site of plaque deposition [43]. The IVUS image is created by using IVUS imaging.

IVUS imaging is a catheter-based approach that provides an accurate luminal and transmural image of vascular structures. A catheter is usually inserted in the body as shown in Figure 2.5. From Figure 2.5, it can be seen that the catheter can be inserted in groin (femoral artery) or in wrist (radial artery). The IVUS method uses a specially designed thin catheter with the ultimately-miniaturized ultrasound probe attached to its distal end. The equipment required to perform IVUS consists of 2 major components; a catheter incorporating a miniaturized transducer, and a console containing the electronics necessary to reconstruct the image. High ultrasound frequencies are used; typically centered at 20 to 50 MHz, providing excellent theoretical resolution.

The probes are inserted into the vessel as shown in Figure 2.6 by a catheter with a diameter of 0.96 to 1.17 mm. Two technical approaches to transducer design have emerged in years; mechanically rotated and multi-element electronic array imaging devices. Mechanical transducers, the most frequently used type of IVUS catheters, consists of a single piezoelectric transducer. The 360 degree view of the vessel is obtained by rotating the probe. IVUS images are acquired by means of high frequency, single-use probes based on various mechanical and electronic phased-array systems. From Figure 2.6, it can be seen that the probe rotates in the arterial lumen in order to receive an ultrasound radio frequency (RF) signal reflected from the plaque and the vascular wall.

From RF signals received is possible to reconstruct the 360 degree cross-sectional representation of the inner vessel morphology. To form a transverse cross-sectional image of the vessel in real time, the ultrasound beam is rotated at 30 revolutions per second leading to 30 images per second. Each beam can be seen as a radius of the final circular IVUS image that shows the cross-section of the explored vessel. An example of US signal generating the IVUS image is also shown in Figure 2.7. The number of position $M(M = 256)$ assumed by the rotational catheter, during IVUS data acquisition. A-lines are collected by the probe. Each A-line can be sampled, and N samples, quantized by using K -bit, are obtained. In this way, each IVUS frame can be stored and processed as an $M \times N$ matrix. The information contained in this matrix is related to the polar domain (r, θ) of the vessel morphology [42].

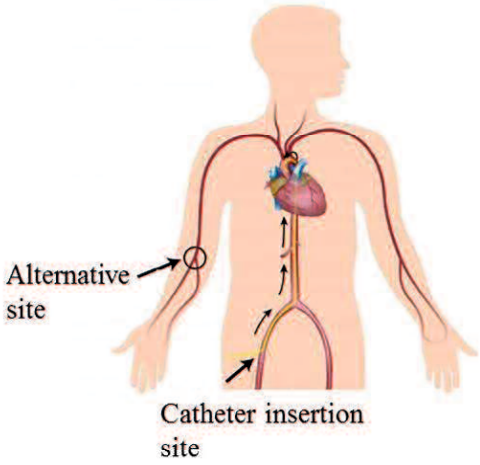

Figure 2.5: Catheter insertion site (http://www.wisegeek.com/).

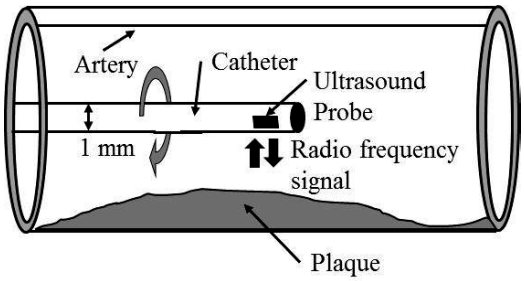

Figure 2.6: Catheter.

In papers, the transmitting frequency of the probe used is 40 MHz. The RF signal is sampled at 200 Mhz (i.e. 200×10^6 sample/sec). The assumed tissue speed is 1.55 mm/ μ s. In the data sampling process, 256 beams (A-lines) by 1250 samples for each image are acquired. They are stored as a matrix of 1250×256 elements. The samples only took into account 1024 samples over the 1250 available, discarding the farther radial region. The IVUS image is generated by using the amplitude information from the received ultrasound RF signals.

The steps of IVUS image construction are summarized as follows:

1. Transformation of a RF signal into 8-bit luminal intensity signal.

   The IVUS image is constructed by using the amplitude information from the received ultrasound RF signals. In order to visualize the inside of a coronary artery, the sampled RF signal is firstly transformed into an 8-bit luminal intensity signal by taking the absolute value of the signal.

2. Calculation of time gain compensation (TGC).

   The quality of ultrasound images is often affected by incorrect TGC [44]. The US propagating in the tissue is influenced by an attenuation due to depth. TGC is a setting applied in diagnostic ultrasound imaging to account for tissue attenuation [45]. By increasing the received signal intensity by depth, the artifacts in the uniformity of a B-mode image's intensity are reduced. A-line RF signals before and after applying the TGC function are shown in Figure 2.8. The blue line and green line show A-line RF signal before and after applying the TGC function, respectively. The TGC function which used is defined as

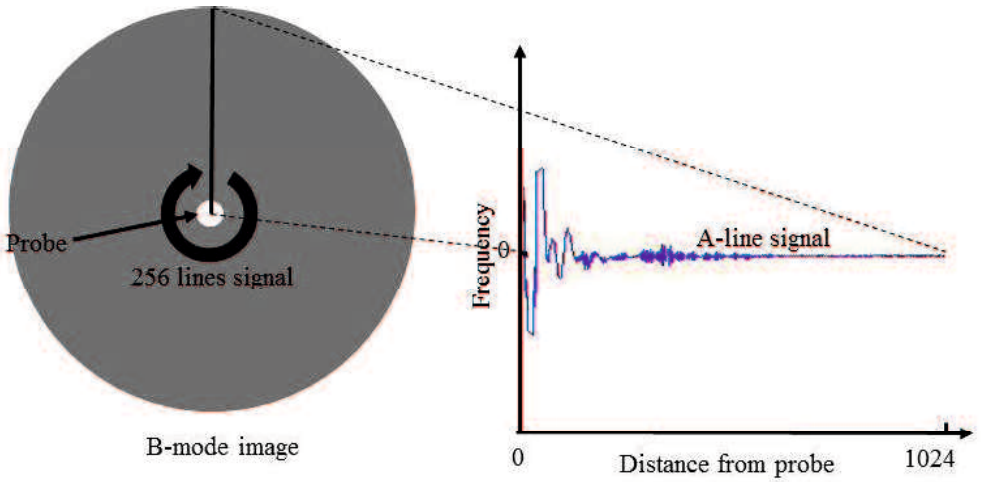

Figure 2.7: An example of US signal generating the IVUS image.

follows:

$$T(r) = 1 - e^{-\beta r}, \tag{2.1}$$

where $\beta = \ln 10^{\alpha f/20}, \alpha$ is the attenuation factor of the tissue measured in dB/MHz $\cdot$ cm. f is the frequency of the transducer in MHz and r is the radial distance from the catheter in cm. The values used in this paper are $\alpha^2 = 0.1$ dB/MHz $\cdot$ cm, $f = 40$ MHz, and r varies between 0.7810 mm and 8.7706 mm.

Different attenuation factors can be used for each tissue in order to be more precise in the vessel modelling. However, in practice this is not feasible since there is no prior information about the presence of specific tissues. Therefore, a weighted average of all possible factors can be assumed.

3. Filter the RF signal by using band-pass filter.

   In order to reduce the noise effect and spurious harmonic components outside the band of interest, the RF signal is filtered by a band-pass filter. For this purpose, the Butterworth filter [46] is suitable, given that its frequency response is as flat as mathematically possible in the passband. Given the central frequency of the catheter $f_0 = 40$. It is expected that the main spectral information in a certain band centered is found in f_0. Data are then filtered with the Butterworth filter ($n = 10, f_L = 20$ MHz, $f_H = 60$ MHz). After applying the Butterworth filter, A-line RF signal (blue line) is smoother as shown in Figure 2.9.

4. Take the envelope of the RF signal.

   After filtering, the envelope of the signal needs to be recovered ; to change from a bipolar to a unipolar signal, in order to achieve final conversion between 0

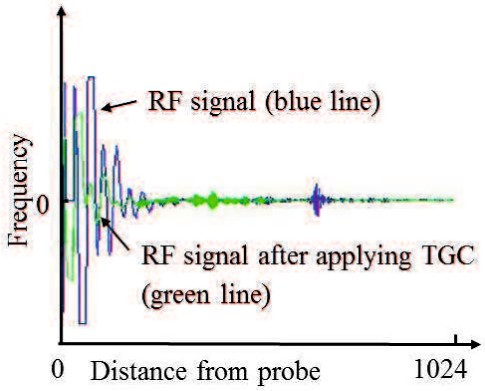

Figure 2.8: A-line RF signal after applying the TGC function.

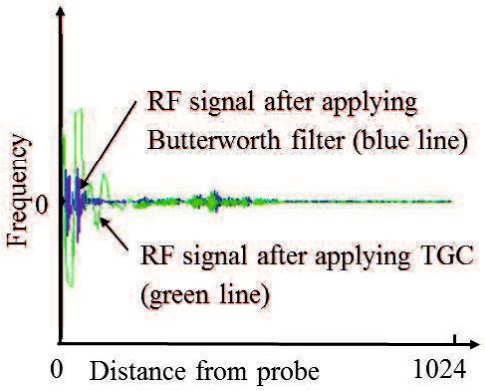

Figure 2.9: A-line RF signal after applying the Butterworth filter.

and 255. This is done by taking the absolute value of Hilbert transform of the signal. Figure 2.10 shows an envelope (red line) of A-line RF signal(blue line).

5. Normalization.

   Normalization means transforming data to specific range. In this paper, the data range has been changed to have a value between 0 and 1. This allows the application of homogeneous data ranges for all cases. The normalization of RF data matrix is defined by:

$$R_{norm} = (R - R_{min})/(R_{max} - R_{min}), \tag{2.2}$$

   where R is RF data matrix. R_{min} and R_{max} are the minimum and maximum value of RF data matrix, respectively.

6. Gamma Correction.

   Many devices used for capturing, printing, or displaying an image generally apply a transformation called power-law or gamma correction [47]. Since the IVUS image also needs the contrast adjustment, gamma correction is used. It is defined by:

$$R_y = 255 \times R_{norm}^{\gamma}, \tag{2.3}$$

   where R_{norm} is a normalization of RF data and γ is a positive constant introducing the gamma value. A larger gamma results in a higher contrast image. By this assumption, the value of γ typically can be determined experimentally, by passing a calibration target with a full range of known luminance values through the imaging device. In this paper, γ is equal to 1.

The final result is a tomographic cross-sectional image of a coronary artery after transforming into a polar coordinates as shown in Figure 2.11. This image is called a “B-mode image”.

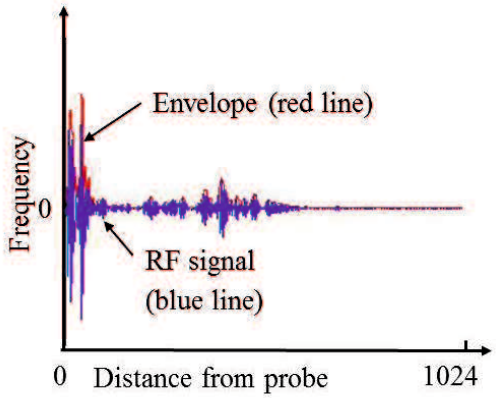

Figure 2.10: Envelope of A-line RF signal.

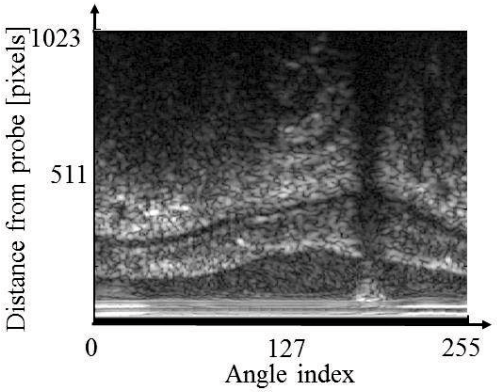

Figure 2.11: IVUS B-mode image.

2.1.1.3 Coronary plaque boundary detection

Plaque composition in ultrasound is usually characterized by the intensity of the signals as soft (gray) echoes. These are very high intensity (bright) reflectors that create distal shadowing, and echoes of intermediate intensity, features that correspond to tissue, calcification, and fibrosis, respectively. In addition, echolucent or signal free zones have been found to represent lipid accumulations. For these reasons, the IVUS technologies are a suitable technique for the assessment of atherosclerotic plaque in coronary artery analysis. In particular, it is appropriate in the study of the vulnerable plaque.

In quantitative assessment of coronary plaque, the following two boundaries need to be detected in the IVUS B-mode image. One is the luminal boundary (LB) between the lumen and the plaque, and the other is the adventitial boundary (AB) between the plaque and the vascular wall as shown in Figure 2.12.

The conventional boundary detection uses the spline function. However, the conventional method needs several seed points. The seed points are marked directly on the IVUS image by a medical doctor. Those points are then interpolated smoothly by a parametric spline function. Interpolation is carried out according to the marking order of the seed points. However, its precision is considerably affected by the number of seed points and/or a distance between those points [48].

Koga et al. [12] presented a fully automatic boundary extraction of coronary plaque in the IVUS image by the PMD filter and the T-S type fuzzy inference. In this method, the seed points are automatically decided by heuristic rule. The plaque boundaries are approximated by the T-S fuzzy inference. The number and location of MSFs of the T-S fuzzy inference are decided by using method in the reference [11]. They are decided by considering a complexity of plaque. However, the location of seed points affects the accuracy of this method.

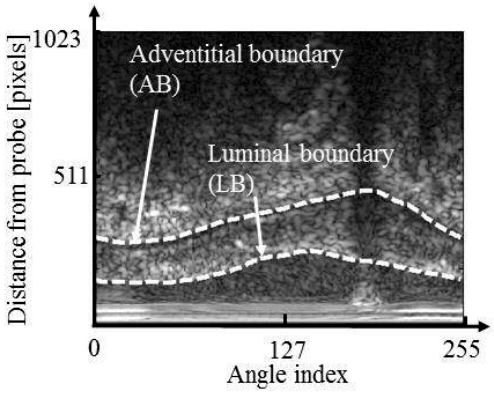

Figure 2.12: Plaque boundary in IVUS B-mode image.

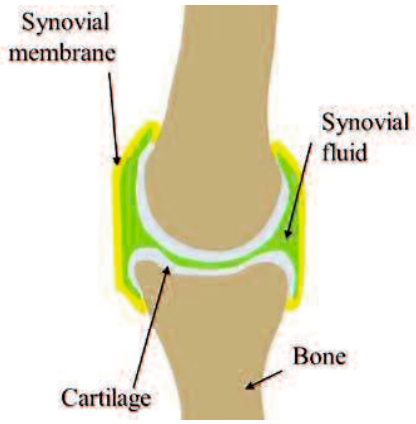

Figure 2.13: Joint.

2.1.2 Arthritis and radiography

Arthritis is a chronic inflammatory disorder that typically affects the small joints. It causes premature mortality, disability, and a compromised quality of life [49]. Early treatment of arthritis significantly delays joint destruction, disease activity, and functional disability. X ray (radiography) is one of methods to diagnose arthritis.

2.1.2.1 Skeleton system and arthritis

2.1.2.1.1 Skeleton system

The human body performs the basic life process of interaction. It detects information about the environment and also reacts to that information. This involves various parts of the body; such as the sense organs, the nervous system and the musculoskeletal system. The musculoskeletal system is composed of many muscles and bones. Its primary functions include supporting the body, allowing motion, and protecting vital organs. The musculoskeletal system can be divided into two subsystems, i.e., skeletal system and muscle system.

Skeletal system is the system of bones, associated with the cartilages and joints of human body. A skeleton is defined as the hard framework of human body around which the entire body is built. Almost all the hard parts of human body are components of human skeletal system. Joints are very important because they help the skeletal system to move in different locations. The skeleton in the body consists of bones connected with joints that allow movement [50]. When humans are born, they have 270 bones in their skeletal system, and even more bones that form during childhood. By adulthood, several separate bones fuse together so that the number of bones decrease to around 206, which make up the adult skeletal system.

The skeletal system serves 6 major functions in human body as follows [51]:

1. Support

The skeleton provides the framework which supports the body and maintains its shape.

2. Movement

   The joints between bones permit movement. Some allow a wider range of movement than others, e.g. the ball and socket joint allows a greater range of movement than the pivot joint at the neck.

3. Protection

   It protects the body's soft, internal organs, like the brain, heart and lungs.

4. Blood cell production

   The skeleton is the site of haematopoiesis, which takes place in red bone marrow.

5. Storage

   Bone matrix can store calcium and is involved in calcium metabolism, and bone marrow can store iron in ferritin and is involved in iron metabolism.

6. Endocrine regulation

   Bone cells release a hormone called osteocalcin, which contributes to the regulation of blood sugar (glucose) and fat deposition.

2.1.2.1.2 Bone

The bones, which form the skeleton, contain a hard material and has very good mechanical properties. Bone is a dense type of connective tissue impregnated with inorganic salts; mainly the salts of calcium such as calcium phosphate, calcium carbonate etc. The organic portion of the bone constitutes one third of the bone, whilst the inorganic salt component constitutes two thirds. The inorganic salts are mainly responsible for rigidity and hardness, which make the bone resist compression caused by the forces of weight and impact. The organic connective tissue portion of the bone makes it resilient and thus the bone can afford resistance to tensile forces. In strength, bone is comparable to iron and steel.

A joint is where two or more bones come together, such as the hip or knee as shown in Figure 2.13. The bones of a joint are covered with a smooth, spongy material called cartilage; which cushions the bones and allows the joint to move without pain. The joint is lined by a thin film of tissue called the synovium. The synovium's lining produces a slippery fluid called synovial fluid that nourishes the joint and helps reduce friction. Synovial fluid is covered by synovial membrane which is the soft tissue found between the joint capsule and the joint cavity of synovial joints.

The hand bone is one of the important bones, and is often used for radiological examination to diagnose any diseases. Each hand consists of 27 bones, 8 form the wrist,

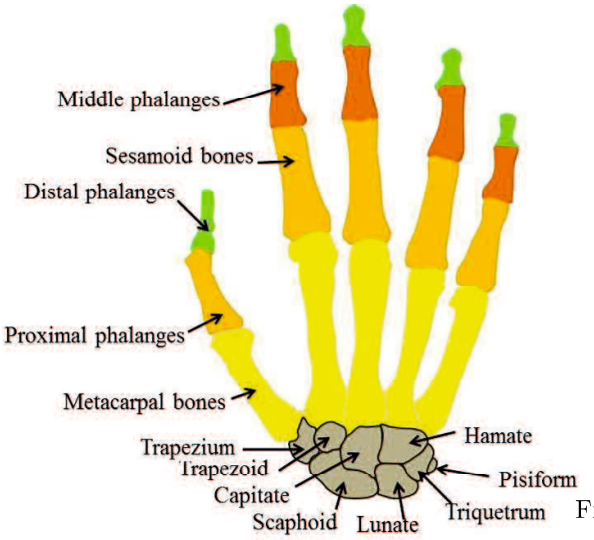

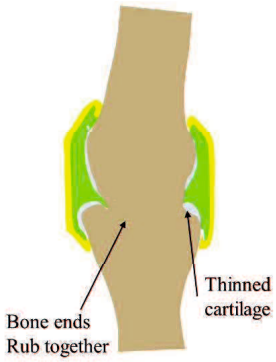

Figure 2.15: Joint affected by osteoarthritis.

Figure 2.14: Hand bones structure.

and nineteen form the palm. The hand bones consist of the carpal bones (wrist), metacarpals and phalanges (palm). At birth, only the shafts of the metacarpals and phalanges are present. The structure of the hand bone is shown in Figure 2.14.

2.1.2.1.3 Arthritis

Arthritis means "joint inflammation". Inflammation is one of the body's natural reactions to disease or injury, and includes swelling, pain, and stiffness. Inflammation that lasts for a very long time or recurs, as in arthritis, can lead to tissue damage [52]. With arthritis, an area in or around a joint becomes inflamed, causing pain, stiffness and, sometimes has difficulty moving. Some types of arthritis also affect other parts of the body, such as the skin and internal organs.

Although the exact cause of arthritis may not be known, there are several risk factors for arthritis. A risk factor is a trait or behavior that increases a person's chance of developing a disease or predisposes a person to a certain condition. The first risk factors of arthritis are as follows:

1. Age.

   The risk of developing arthritis, especially osteoarthritis, increases with age.

2. Gender.

   In general, arthritis occurs more frequently in women than in men.

3. Obesity.

   Being overweight puts extra stress on weight-bearing joints, increasing wear and tear, and increasing the risk of arthritis, especially osteoarthritis.

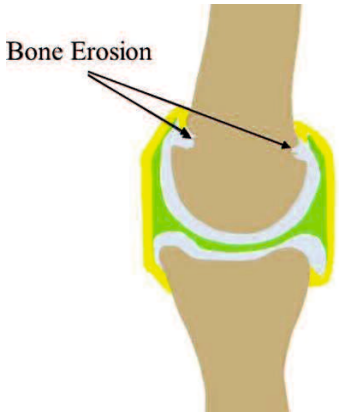

Figure 2.16: Joint affected by rheumatoid arthritis.

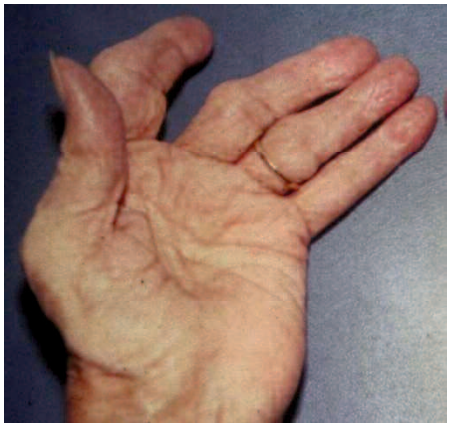

Figure 2.17: Hand affected by rheumatoid arthritis (http://www.doctor-harris.com/).

4. Work factors.

   Some jobs that require repetitive movements or heavy lifting can stress the joints and/or cause an injury, which can lead to arthritis, particularly osteoarthritis.

5. Previous injury.

   Any previous injury such as a fracture or a muscle, ligament or tendon injury can develop into arthritis.

6. Systemic diseases.

   Systemic conditions such as gout and lupus are types of arthritis.

7. Infections.

   Bacterial and viral conditions such as chlamydia, mumps and human parvovirus can cause arthritis.

There are more than 100 different types of arthritis. Two of the more common types include:

1. Osteoarthritis.

   Osteoarthritis is the most common type of arthritis. Figure 2.15 shows the joint affected by osteoarthritis. It occurs when the cartilage covering the end of the bones gradually become thin. Without the protection of the cartilage, the bones begin to rub against each other and the resulting friction leads to pain and swelling. In severe osteoarthritis, the cartilage can become so thin that it doesn't cover the ends of the bones. The bones rub against each other and start to wear away. At the loss of the cartilage, the wearing of bone and the bony spurs can change the shape of joints, forcing the bones out of their normal position.

Osteoarthritis can occur in any joint, but most often affects the hands and weight-bearing joints such as the knee, hip and facet joints (in the spine). Osteoarthritis often occurs as the cartilage breaks down, or degenerates, with age or overuse. The surfaces within the joints become damaged and the joint doesn't move as smoothly as it should. This condition is sometimes called osteoarthrosis. Older terms are degenerative joint disease or wear and tear.

It is very important for osteoarthritis to be diagnosed, because there are many different types of arthritis and some need very different treatments.

2. Rheumatoid arthritis.

   Rheumatoid arthritis is an inflammatory disease that exerts its greatest impact on joints of the body that are lined with synovium, a specialised tissue responsible for maintaining the nutrition and lubrication of the joint. It typically affects the small joints of the hands and the feet, and usually both sides equally in a symmetrical distribution, though any synovial joint can be affected. In patients with established and aggressive disease, most joints will be affected over time [53]. This disease often occurs in more than one joint and can affect any joint in the body [54]. The inflammation then spreads to the surrounding tissues, and can eventually damage cartilage and bone. In more severe cases, rheumatoid arthritis can affect other areas of the body, such as the skin, eyes, lungs, and nerves [55].

   Figure 2.16 shows a joint affected by rheumatoid arthritis. It can be seen that the bone suffers from erosion. The first stage, rheumatoid arthritis causes in inflammation of the synovial membrane, swelling and warming the whole joint, which produces pain and reduced mobility on the affected area. In the second stage, the synovium cells start to grow and divide, thickening the membrane and releasing enzymes. Such enzymes dissolve the bonecovering cartilage and might erode the bone itself. At the severe stages of rheumatoid arthritis, the cartilage collapses and bones might mount one over the other which makes the joint completely loose its function. Figure 2.17 shows an example of heavily affected hand.

   Since rheumatoid arthritis can provoke irreversible joint damage even in the first stages, there is a significant decrease in the quality of life of patients affected by rheumatoid arthritis. Treatments against rheumatoid arthritis require medical trials for demonstrating their effectiveness, and, thus accurate methodologies for assessing the degree of rheumatoid arthritis are needed too.

2.1.2.2 Radiography

X-Ray or radiography is used in a very wide range of applications including medicine, engineering, forensics, security, etc. There are two general types of x-ray procedures:

Figure 2.18: Bone erosion.

Figure 2.19: Bone boundary detection by doctors.

radiographic examinations and fluoroscopic examinations. Radiographic examinations, which will be used in this study, employ x-ray film and usually an x-ray tube mounted from the ceiling on a track that allows the tube to be moved in any direction. Such examinations provide the radiologist with fixed photographic images.

Radiographic examination of the hand is performed using posteroanterior, oblique, and lateral projections. The posteroanterior projection is the best conventional view for demonstrating malalignment, joint-space narrowing, and soft-tissue abnormalities in early rheumatoid arthritis. Whilst the anteroposterior oblique projection is commonly used to look for early evidence of rheumatoid arthritis at the second through fifth proximal phalanges and metatarsophalangeal joints. Both hands are generally exposed, with the contralateral image used for bone structure comparison.

To produce a satisfactory x-ray, one must supply the x-ray tube with a high voltage and a sufficient electric current. X-ray voltages are measured in kilovolts peak (kVp). One kilovolt (kV) is equal to 1000 V of electric potential. X-ray currents are measured in milliamperes (mA), where the ampere (A) is a measure of electric current. The normal household current is a few amperes. The prefix kilo stands for 1000; the prefix milli, for 1/1000, or 0.001. The voltage and the current create the power to drive the x-ray tube to produce x-rays which then penetrate that part of the body to be examined, and imprint the x-ray film [56] .

2.1.2.3 Arthritis diagnosis by using bone radiograph

Radiograph is the most useful test to confirm arthritis. Measurement of the degree of joint damage represents an important tool to assess disease progression and effectiveness of current treatments [57, 35]. Periarticular osteopenia, erosions and joint space narrowing are features of arthritis that can be seen on the radiography of the hands and feet. Magnification radiography contributes to detection in specific ways and characterization of bone, joint, and soft tissue abnormalities. Radiograph may show changes such as bone spurs or narrowing of the space between bones. It will also show whether any calcium has settled in a joint.

Once one hand has arthritis, the other usually follows. A medical doctor usually uses a hand bone radiograph to give arthritis diagnosis. The hand bones are analyzed to detect erosion caused by arthritis as shown in Figure 2.18. To detect the hand bone erosion, medical doctors need to detect the bone boundary. Figure 2.19 shows the bone boundary detection by medical doctors.

2.2 Image processing methods

Image processing is a method to convert an image into digital form and perform operations on it, in order to get an enhanced image or to extract useful information. This section will describe several image processing methods which related with the proposed method.

2.2.1 Perona-Malik diffusion filter

An image acquired by a camera or other imaging system is often unable to be used directly. The image may be corrupted by random variations in intensity, variations in illumination, or poor contrast that must be dealt with in the early stages of vision processing. Image filtering became an important field to handle this problem.

Linear scale space has contributed to image filtering, which is a formal theory for handling image structures at different scales, by representing an image as a one-parameter family of smoothed images. In this theory, Gaussian low-pass filters process the original fine-scale image, generating simplified coarse-scale images. Unfortunately, coarse-scale images generated by Gaussian filters present blurred edges that do not spatially match the original edges.

In order to keep important edges sharp and spatially fixed whilst filtering noise and small edges, Perona and Malik have introduced the non linear scale-space by using anisotropic diffusion filter [24]. It has two advantages, one is to preserve the edges of an image, and the other is to reduce speckle noise. The Perona-Malik diffusion (PMD) filter is defined by:

$$\begin{aligned} I_t &= \frac{\partial I}{\partial t} \\ &= div(c(i,j,t)\nabla I), \end{aligned} \tag{2.4}$$

where *div* represents divergence, ∇I represents a gradient of an image, and $c(i, j, t)$ denotes a diffusion coefficient. The diffusion coefficient will be 1 in the inferior of each region and 0 at the boundaries. The blurring will then take place separately in each region with no interaction between regions. The region boundaries would remain sharp.

A current best estimate of the location of the boundaries appropriate to each scale. Let $\mathbf{E}(i, j, t)$ be an estimate of the location of the boundaries. It is a vector defined on the image which ideally should have the following properties:

1. $\mathbf{E}(i, j, t) = 0$ in the inferior each region,

2. $\mathbf{E}(i, j, t) = \mathbf{T}\mathbf{e}(i, j, t)$ at each edge point, where $\mathbf{e}(i, j, t)$ is a unit vector normal to edge at the point, and $\mathbf{T}$ is the local contrast of the edge.

If an estimate $\mathbf{E}(i, j, t)$ is available, the diffusion coefficient $c(i, j, t)$ can be chosen to be a function $c = g(\|\mathbf{E}(i, j, t)\|)$. The simplest estimate of the edge positions is achieved through the gradient of brightness function, i.e., $\mathbf{E}(i, j, t) = \nabla I(i, j, t)$ which gives excellent result. From this estimate, the diffusion coefficient $c(i, j, t)$ can be obtained:

$$c(i, j, t) = g(\|\nabla I(i, j, t)\|). \tag{2.5}$$

$g(\cdot)$ refers to an edge stopping function, which is defined by:

$$g(z) = \frac{1}{1 + \left(\frac{z}{K}\right)^2}, \tag{2.6}$$

where K is a parameter which controls the strength of diffusion. $g(\cdot)$ takes a large value at the regions where the intensity gradients are low. It takes a small value at the regions where the intensity gradients are high. The behavior of the PMD filter depends on two parameters: the artificial time parameter t and the gradient thresholding parameter K. However, if the discretized diffusion is iterated until the convergence $t \longrightarrow \infty$, the output image depends only on K. Thus, the appropriate choice of K is essential to obtain a conveniently filtered image. However, it seems that no clear relationship between the parameter K and the output image has ever been established, and hence the choice of K is a guesswork.

The PMD filter is discretized by using a numerical scheme. Equation (2.4) can be discretized, with brightness value associated with the vertices, and conduction coefficients to the arcs. The structure of the discrete computational scheme for simulating the diffusion equation is shown in Figure 2.20. This scheme has 4 directions (North (N), East (E), South (S), West (W)). The discretization process of the PMD filter is as follows:

$$
\begin{aligned}
\tfrac{\partial I}{\partial t} &= div(c(i,j,t)\nabla I(i,j,t)) \\
&= \nabla^T(c(i,j,t)\nabla I(i,j,t)) \\
&= \tfrac{\partial}{\partial i}[c(i,j,t)\tfrac{\partial}{\partial i}I(i,j,t)] + \tfrac{\partial}{\partial j}[c(i,j,t)\tfrac{\partial}{\partial j}I(i,j,t)] \\
&\approx \tfrac{\partial}{\partial i}[c(i,j,t)\tfrac{1}{\Delta i}(I(i+\tfrac{\Delta i}{2},j,t) - I(i-\tfrac{\Delta i}{2},j,t))] \\
&\quad +\tfrac{\partial}{\partial j}[c(i,j,t)\tfrac{1}{\Delta j}(I(i,j+\tfrac{\Delta j}{2},t) - I(i,j-\tfrac{\Delta j}{2},t))] \\
&\approx \tfrac{1}{\Delta i^2}[c(i+\tfrac{\Delta i}{2},j,t)(I(i+\Delta i,j,t) - I(i,j,t)) \\
&\quad -c(i-\tfrac{\Delta i}{2},j,t)(I(i,j,t) - I(i-\Delta i,j,t))] \\
&\quad +\tfrac{1}{\Delta j^2}[c(i,j+\tfrac{\Delta j}{2},t)(I(i,j+\Delta j,t) - I(i,j,t)) \\
&\quad -c(i,j-\tfrac{\Delta j}{2},t)(I(i,j,t) - I(i,j-\Delta j,t))] \| \Delta i = \Delta j = 1 \\
&= [c(i+\tfrac{1}{2},j,t)(I(i+1,j,t) - I(i,j,t)) \\
&\quad -c(i-\tfrac{1}{2},j,t)(I(i,j,t) - I(i-1,j,t))] \\
&\quad +[c(i,j+\tfrac{1}{2},t)(I(i,j+1,t) - I(i,j,t)) \\
&\quad -c(i,j-\tfrac{1}{2},t)(I(i,j,t) - I(i,j-1,t))] \\
&= c(i+\tfrac{1}{2},j,t)(I(i+1,j,t) - I(i,j,t)) \\
&\quad +c(i-\tfrac{1}{2},j,t)(I(i-1,j,t) - I(i,j,t)) \\
&\quad +c(i,j+\tfrac{1}{2},t)(I(i,j+1,t) - I(i,j,t)) \\
&\quad +c(i,j-\tfrac{1}{2},t)(I(i,j-1,t) - I(i,j,t)).
\end{aligned}
$$

Therefore, Equation (2.7) is solved by using finite difference on a discrete spatial grid in the domain $\mathbf{s} = (i,j)$. Let $I(\mathbf{s}, n\Delta t) = I_{\mathbf{s}^{(t)}}$ where Δt is the time step. Then for spatial grid $\mathbf{s}$, I can be calculated by:

$$
\begin{aligned}
\tfrac{\partial I}{\partial t} &\approx c(i+\tfrac{1}{2},j,t)(I(i+1,j,t) - I(i,j,t)) \\
&\quad +c(i-\tfrac{1}{2},j,t)(I(i-1,j,t) - I(i,j,t)) \\
&\quad +c(i,j+\tfrac{1}{2},t)(I(i,j+1,t) - I(i,j,t)) \\
&\quad +c(i,j-\tfrac{1}{2},t)(I(i,j-1,t) - I(i,j,t)) \\
\tfrac{I_{\mathbf{s}}^{(t+1)} - I_{\mathbf{s}}^{(t)}}{\Delta t} &\approx c(i+\tfrac{1}{2},j,t)(I(i+1,j,t) - I(i,j,t)) \\
&\quad +c(i-\tfrac{1}{2},j,t)(I(i-1,j,t) - I(i,j,t)) \\
&\quad +c(i,j+\tfrac{1}{2},t)(I(i,j+1,t) - I(i,j,t)) \\
&\quad +c(i,j-\tfrac{1}{2},t)(I(i,j-1,t) - I(i,j,t)) \\
I_{\mathbf{s}}^{(t+1)} &\approx I_{\mathbf{s}}^{(t)} + \Delta t(c(i+\tfrac{1}{2},j,t)(I(i+1,j,t) - I(i,j,t)) \\
&\quad +c(i-\tfrac{1}{2},j,t)(I(i-1,j,t) - I(i,j,t)) \\
&\quad +c(i,j+\tfrac{1}{2},t)(I(i,j+1,t) - I(i,j,t)) \\
&\quad +c(i,j-\tfrac{1}{2},t)(I(i,j-1,t) - I(i,j,t))) \\
&= I_{\mathbf{s}}^{(t)} + \Delta t(c^t_{i+\frac{1}{2},j}(I^t_{i+1,j} - I^t_{i,j}) + c^t_{i-\frac{1}{2},j}(I^t_{i-1,j} - I^t_{i,j}) \\
&\quad +c^t_{i,j+\frac{1}{2}}(I^t_{i,j+1} - I^t_{i,j}) + c^t_{i,j-\frac{1}{2}}(I^t_{i,j-1} - I^t_{i,j})) \\
&= I_{\mathbf{s}}^{(t)} + \Delta t(c^t_{N_{i,j}}(I^t_{i+1,j} - I^t_{i,j}) + c^t_{S_{i,j}}(I^t_{i-1,j} - I^t_{i,j}) \\
&\quad +c^t_{E_{i,j}}(I^t_{i,j+1} - I^t_{i,j}) + c^t_{W_{i,j}}(I^t_{i,j-1} - I^t_{i,j})),
\end{aligned}
\tag{2.7}
$$

where $0 \leq \Delta t \leq 1/4$ for the numerical scheme to be stable, N, S, E, W are the mnemonic superscript, and subscripts on the square bracket are applied to all the

terms it encloses, and the symbol $\bigtriangledown$ (not to be confused with ∇, which is for the gradient operator) indicates nearest-neighbour differences:

$$\begin{array}{l} \bigtriangledown_N I^t_{i,j} \equiv I^t_{i+1,j} - I^t_{i,j} \\ \bigtriangledown_S I^t_{i,j} \equiv I^t_{i-1,j} - I^t_{i,j} \\ \bigtriangledown_E I^t_{i,j} \equiv I^t_{i,j+1} - I^t_{i,j} \\ \bigtriangledown_W I^t_{i,j} \equiv I^t_{i,j-1} - I^t_{i,j}. \end{array} \tag{2.8}$$

The conduction coefficients are updated at every iteration as a function gradient in Equation (2.5). They are shown as follows:

$$\begin{array}{l} c^t_{N_{i,j}} = g(\|(\nabla I)^t_{i+(1/2),j}\|) \\ c^t_{S_{i,j}} = g(\|(\nabla I)^t_{i-(1/2),j}\|) \\ c^t_{E_{i,j}} = g(\|(\nabla I)^t_{i,j+(1/2)}\|) \\ c^t_{W_{i,j}} = g(\|(\nabla I)^t_{i,j-(1/2)}\|). \end{array} \tag{2.9}$$

The value of the gradient can be computed on different neighborhood structures, achieving diffferent compromises between accuracy and locality. The simplest choice consists of approximating the norm of the gradient at each arc location with the absolute value of its projection along the direction of the arc:

$$\begin{array}{l} c^t_{N_{i,j}} = g(\|\bigtriangledown_N I^t_{i,j}\|) \\ c^t_{S_{i,j}} = g(\|\bigtriangledown_S I^t_{i,j}\|) \\ c^t_{E_{i,j}} = g(\|\bigtriangledown_E I^t_{i,j}\|) \\ c^t_{W_{i,j}} = g(\|\bigtriangledown_W I^t_{i,j}\|). \end{array} \tag{2.10}$$

By using Equations (2.7), (2.8) and (2.10), the PMD in discrete version is obtained as follows:

$$\begin{array}{rcl} I^{(t+1)}_{\mathbf{s}} & = & I^{(t)}_{\mathbf{s}} + \Delta t[c^t_{N_{i,j}} \bigtriangledown_N I^t_{i,j} + c^t_{S_{i,j}} \bigtriangledown_S I^t_{i,j} + c^t_{E_{i,j}} \bigtriangledown_E I^t_{i,j} + c^t_{W_{i,j}} \bigtriangledown_W I^t_{i,j}] \| \Delta t = \frac{\lambda}{|\phi_{\mathbf{s}}|} \\ & = & I^{(t)}_{\mathbf{s}} + \frac{\lambda}{|\phi_{\mathbf{s}}|}[g(\|\bigtriangledown_N I^t_{i,j}\|) \bigtriangledown_N I^t_{i,j} + g(\|\bigtriangledown_S I^t_{i,j}\|) \bigtriangledown_S I^t_{i,j} \\ & & + g(\|\bigtriangledown_E I^t_{i,j}\|) \bigtriangledown_E I^t_{i,j} + g(\|\bigtriangledown_W I^t_{i,j}\|) \bigtriangledown_W I^t_{i,j}] \\ & = & I^{(t)}_{\mathbf{s}} + \frac{\lambda}{|\phi_{\mathbf{s}}|} \sum g(\bigtriangledown I^{(t)}_{\mathbf{s},p}) I^{(t)}_{\mathbf{s},p}, \end{array} \tag{2.11}$$

where p and $I^{(t)}_{\mathbf{s}}$ represent the neighboring pixels of $\mathbf{s}$ and an intensity at $\mathbf{s}$ with an iteration count t, respectively. $\phi_{\mathbf{s}}$ and $|\phi_{\mathbf{s}}|$ represent a set of the diffusion directions and the number of pixels in the neighboring area, respectively. λ is a parameter. Therefore, the Equation (2.11) is called the normal PMD filter.

The initial condition is given by:

$$I^{(0)}_{\mathbf{s}} = I_0(i,j), \tag{2.12}$$

where $I_0(i,j)$ is the original image.

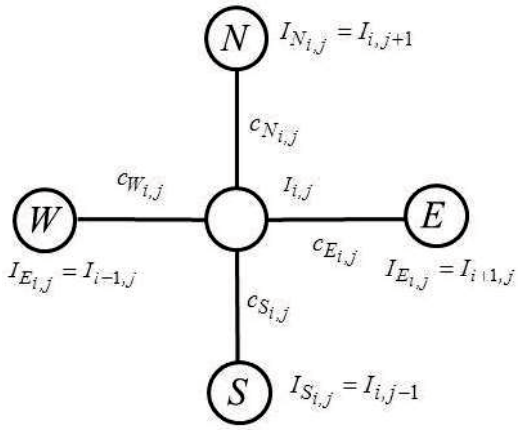

Figure 2.20: The structure of the discrete computational scheme for simulating the PMD filter.

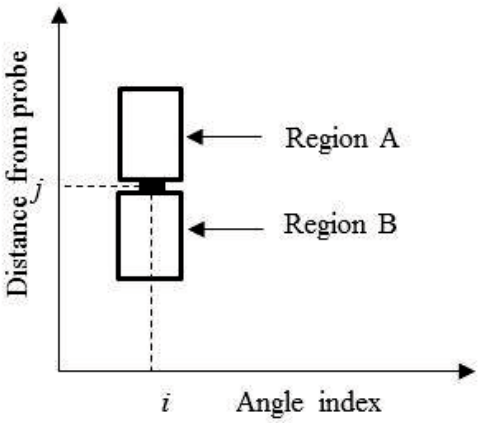

Figure 2.21: Image separability.

2.2.2 Image separability

Edges are primitive features for high level image processing. Many edge extraction methods have been proposed, most of which are mainly based on the gradient of image intensity. These gradient-based methods use a smoothing filter such as the Gaussian filter for suppression of noise [58, 59]. Since they blur edges, the precision for edge localization degrades. In addition, their performance is sensitive to the selection of parameters such as the threshold value for edge extraction.

Other edge extraction methods without smoothing, which are based on the statistical analysis of the distribution of image features; such as image intensity and the image gradient within a local region. These region-based methods are robust to noise compared to gradient-based methods, since they use integrals in extraction edges. However, they require a complex process to improve performance.

An edge detection method using a statistical discriminant measure of image separability, called image separability, has been proposed by Fukui [60]. In this method, an edge is not defined as point where the intensity changes rapidly, but as a region boundary where the features (such as image) of local region are separated in Figure 2.21. The image method has advantages over the above methods, because the image separability has the following features:

1. Insensitivity to noisy and blurred edges,

2. Ability to differentite the edges between texture regions.

Figure 2.21 shows a local region which consists two small regions A and B. The separability for pixel $\mathbf{s}$ can be calculated by a linear discriminant analysis with

information from regions A and B using as follows:

$$\eta_{\mathbf{s}} = \frac{n_A(\bar{I}_A - \bar{I})^2 + \bar{I}_B - \bar{I})^2}{\sum_{k=1}^{C} I_k - \bar{I}}, \tag{2.13}$$

where n_A and n_B represent the numbers of the pixels in the regions of A and B, respectively. $\bar{I}_A$ and $\bar{I}_B$ represent the averages of intensities in the regions of A and B. $\bar{I}$ stands for the average of the intensities in the combined region A and B. C and $\bar{I}_k$ represents the number of the pixels and the intensity of the k-th pixel in the combined region A and B.

The weighted separability for pixel $\mathbf{s}$, which is a modification of the original separability [60] by considering conditions peculiar to IVUS image [5], is defined by:

$$\eta_{\mathbf{s}}^w = \eta_{\mathbf{s}}(\frac{I_{max} - \bar{I}_A}{I_{max}} \times \frac{\bar{I}_B}{I_{max}})^2, \tag{2.14}$$

where I_{max} is the maximum intensity in the whole of image and $\eta_{\mathbf{s}}^w$ satisfies $0 \leq \eta_{\mathbf{s}}^w \leq 1$. The image separability takes the larger value when two regions are separated from each other.

In order to extract the intensity and direction of the candidates of plaque boundary, the mask on Figure 2.21 is used. The main steps for weighted image separability calculation are outlined bellow:

1. Set the mask at a pixel $\mathbf{s}$.
2. Calculate the weighted image separability $\eta_{\mathbf{s}}^w$ by using Equations (2.13) and (2.14).
3. Move the mask to the next pixel. Do steps (1) and (2) until all pixels were calculated.

The weighted image separability detects the candidates of the inner and outer boundaries of plaque by considering the following two conditions peculiar to IVUS images which are:

1. Intensity in the outside area of a luminal boundary (LB) tends to be stronger than that in the inside area of LB,
2. Intensity in the outside area of an adventitial boundary (AB) tends to be stronger than that in the inside area of AB.

2.2.3 Texture analysis

An image texture is a property that represents the surface and structure of an image. Generally speaking, the image texture can be defined as a regular repetition of an element or a pattern on a surface. The image texture is a complex visual

pattern composed of entities or regions with sub-patterns with the characteristics of brightness, color, shape, size, etc. An image region has a constant texture if a set of its characteristics are constant, slowly changing or approximately periodic. The image texture can be regarded as a similarity grouping in an image.

Texture analysis is a major step in texture classification, image segmentation and image shape identification. Image segmentation and shape identification are typically the preprocessing steps for object recognition in an image [61]. Texture analysis refers to a class of the mathematical procedures and models that characterize the spatial variations within imagery by means of extracting information.

Approaches to the texture analysis are usually categorized into structural, statistical, model-based and transform methods. Feature extraction is the first stage of the image texture analysis. The results obtained from this stage are used for texture discrimination, texture classification or object shape determination. One of the feature extraction methods is a histogram based the entropy method.

The image is assumed as a function $f(x, y)$ of two space variables and where $x = 0, 1, ..., N - 1$ and $y = 0, 1, ..., M - 1$. The function can take discrete values of $0, 1, ..., G - 1$, which are the values of the intensity in the image.

The intensity-level histogram is a function showing the number of pixels in the whole image, which is defined by:

$$h(i) = \sum_{x=0}^{N-1} \sum_{y=0}^{M-1} \delta(f(x, y), i), \tag{2.15}$$

where $\delta(j, i)$ is a following Kroneckerfs delta function:

$$\delta(j, i) = \begin{cases} 1, j = i \\ 0, j \neq i. \end{cases} \tag{2.16}$$

Dividing the values $h(i)$ by the total number of pixels in the image, one obtains the appropriate probability density of occurrence of the intensity levels as follows:

$$p(i) = \frac{h(i)}{NM}, i = 0, 1, ..., G - 1. \tag{2.17}$$

The entropy is defined by:

$$E = -\sum_{i=0}^{G-1} p(i) \log (p(i)). \tag{2.18}$$

The entropy method is also often used for characterizing the image texture.

2.2.4 Level set method

Boundaries in an image contain cues that very important to high level visual tasks such as object recognition and scene understanding. Detecting boundaries has been a fundamental problem since the beginning of computer vision.

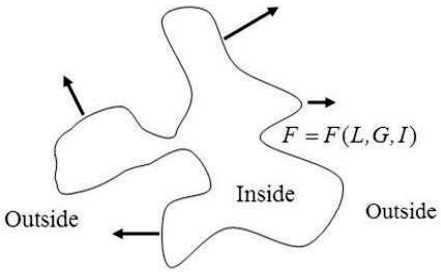

Figure 2.22: Curve propagating with speed F in normal direction.

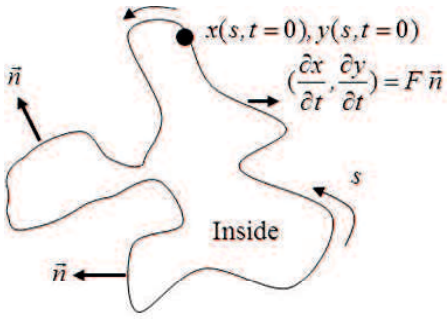

Figure 2.23: Parameterized view of propagating curve.

The level set method has been proposed by Osher and Setian [18]. The level set methods have been widely and successfully used for detecting the image boundaries. A boundary, either a curve in two dimensions or surface in three dimensions, separates one region from another.

The basic idea of the level set method is that the contour is represented by the zero level set of a higher dimensional function, called a level set function. The motion of the contour is formulated based on the evolution of the level set function.

A level set associated to ϕ is geometrically defined as points (in $\Re$), a curve (in $\Re^2$) or a surface (in $\Re^3$). It is given by:

$$\Gamma = \{\mathbf{x} \in \Re^N | \phi(\mathbf{x}) = c\}, \tag{2.19}$$

where $\phi : \Re^N \longrightarrow \Re$ denotes a real-valued function implicitly or explicitly which is defined on a $\Re^N$ for $N = 1,2$ or 3. c represents a constant. The function ϕ is called the level set function associated to Γ. In the case $c = 0$, Γ is a zero level set.

Associated to an interface $\Gamma = \{\mathbf{x} \in \Re^N | \phi(\mathbf{x}) = 0\}$, the interior (inside) region and the exterior (outside) region are defined, respectively as follows:

$$\Omega^- = \{\mathbf{x} \in \Re^N | \phi(\mathbf{x}) < 0\} \tag{2.20}$$

and

$$\Omega^+ = \{\mathbf{x} \in \Re^N | \phi(\mathbf{x}) > 0\}. \tag{2.21}$$

Let us consider a dynamic parametric contour $\mathbf{x}(x(s,t), y(s,t))$, where t is the time and s is the curve parameter. This curve moves in its normal direction with a known speed function F which determines the speed evolution as shown in Figure 2.22. The tangential motions of the interface are ignored. The goal is to track the motion of this interface as it evolves.

The position vector $\mathbf{x}(s,t) = (x(s,t), y(s,t))$ parameterizes γ at time t and $0 \leq s \leq S$. It is assumed that the periodic boundary condition is $\mathbf{x}(0,t) = \mathbf{x}(S,t)$. The

curve is parameterized so that the interior is on the left, in the direction of increasing s (see Figure 2.23).

The curve evolution can be characterized by the following partial differential equation:

$$\frac{\partial \mathbf{x}}{\partial t} = F\mathbf{N}, \tag{2.22}$$

where $\mathbf{N}$ is an inward normal vector to the curve γ. F is a speed function that controls the motion of the contour.

The speed function F can be thought of as depending on three types of arguments, namely:

$$F = F(L, G, I), \tag{2.23}$$

where L is the local properties of the front which are those determined by local information, such as curvature and normal direction. G is the global properties of the front, such as integrals along the front and associated differential equation. The global properties of the front depend on the shape and position of the front for the solution. I is independent properties which are independent of the shape of the front, such as an underlying fluid velocity which passively transports to the front.

Further on, a mathematical description of the level set method will be explained. A closed $N-1$ dimensional hypersurface $\Gamma(t)$ is given. It is an Eulerian for the motion of the hypersurface propagating along its normal direction with speed F. F can be a function of various arguments, including the curvature, normal direction, etc. The main idea of the level set methodology is to embed this propagating interface as the zero level set of a higher dimensional function ϕ. Let $\phi(\mathbf{x}, t = 0)$ be defined as:

$$\phi(\mathbf{x}, t = 0) = \pm d, \tag{2.24}$$

where $\mathbf{x}$ is a point in space in $\Re^N$ and d is the shortest distance from $\mathbf{x}$ to the initial hypersurface $\Gamma(t = 0)$. The plus (minus) sign of ϕ is chosen if the point $\mathbf{x}$ is outside (inside) the initial hypersurface $\Gamma(t = 0)$. And thus, an initial level set function $\phi(\mathbf{x}, t = 0) : \Re^N \longrightarrow \Re$ is given, with the property that gives an initial interface as:

$$\Gamma(t = 0) = \{\mathbf{x} \in \Re^N | \phi(\mathbf{x}, t = 0) = 0\}. \tag{2.25}$$

The goal is to produce an equation for evolving function $\phi(\mathbf{x}, t)$ which contains the embedded motion of $\Gamma(t)$ as the level set $\phi = 0$. Let $\mathbf{x}(t)$ be the path of a point on the propagating front. That is, $\mathbf{x}(t = 0)$ is a point on the initial front $\Gamma(t = 0)$, and $\mathbf{x}_t \cdot \mathbf{N} = F(\mathbf{x}(t))$ where $\mathbf{N}$ is the normal to the front at $\mathbf{x}(t)$. This means that the speed of motion is in the normal direction.

Since the zero level of the evolving function ϕ must always match the propagating hypersurface, it must be:

$$\phi(\mathbf{x}, t) = 0. \tag{2.26}$$

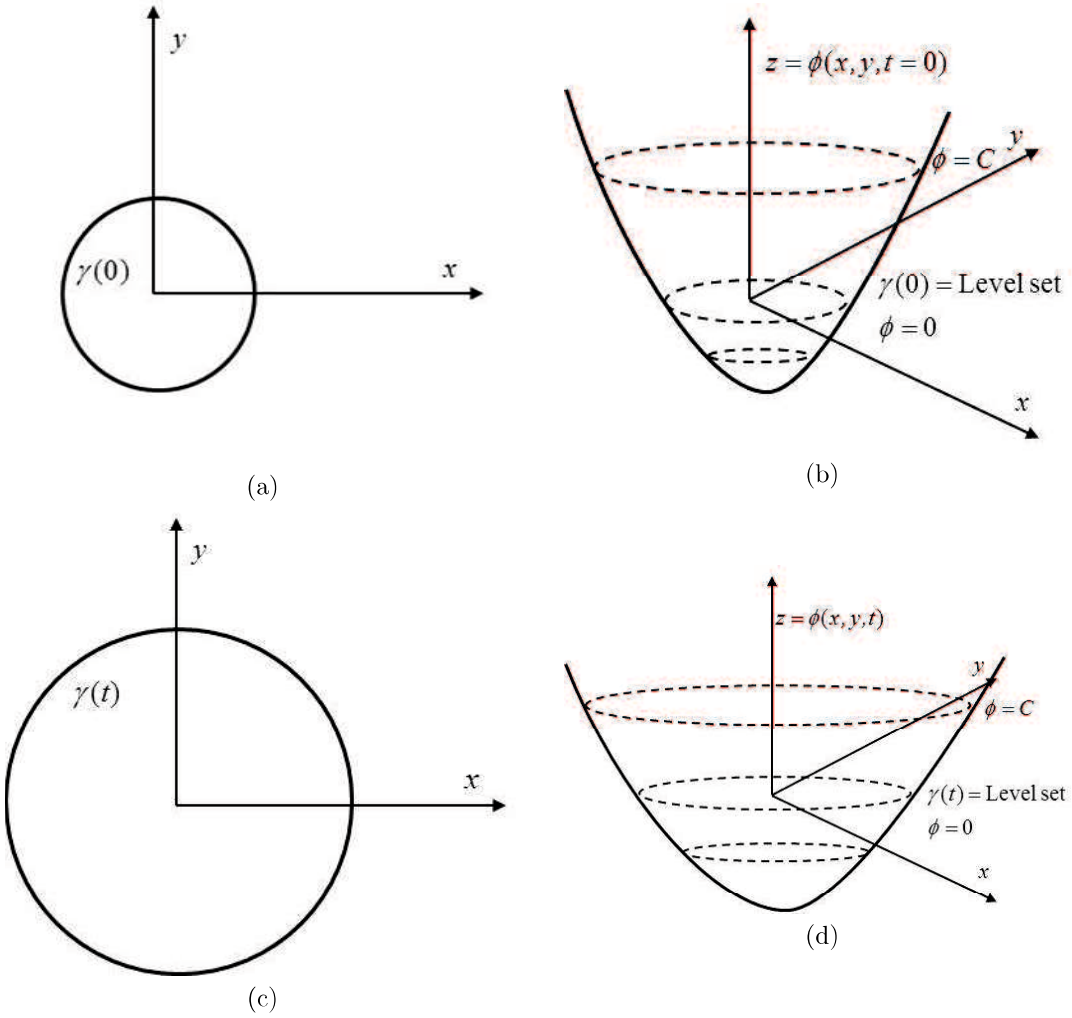

Figure 2.24: Propagating circle.

Equation (2.26) can be differentiated by using the chain rule, so it is obtained by:

$$\frac{\partial \phi}{\partial t} + \nabla \phi(\mathbf{x}, t) \cdot \frac{\partial \mathbf{x}}{\partial t} = 0. \tag{2.27}$$

Since $\mathbf{N} = \frac{\nabla \phi}{|\phi|}$, by using Equation (2.22) the evolution for ϕ of Equation (2.27) can be written as:

$$\begin{aligned} &\phi_t + \nabla \phi(\mathbf{x}, t) F \mathbf{N} = 0 \\ &\phi_t + \nabla \phi(\mathbf{x}, t) F \tfrac{\nabla \phi(\mathbf{x}, t)}{|\nabla \phi(\mathbf{x}, t)|} = 0 \\ &\phi_t + F |\nabla \phi(\mathbf{x}, t)| = 0 \end{aligned} \tag{2.28}$$

$$\phi(\mathbf{x}, t = 0) \text{ given.} \tag{2.29}$$

Equation (2.28) is the time-dependent level set equation. For certain forms of speed function F, a standard Hamilton-Jacobi equation is obtained [62].

Figure 2.24 shows the outward propagation of an initial curve and the accompanying motion of the level set function ϕ. Figure 2.24 (a) shows the initial circle and Figure 2.24 (c) shows the circle at a later time. Figures 2.24 (b) and (d) show the initial position of the level function ϕ and the function at a later time, respectively.

Equation (2.28) can be solved by using finite difference on a discrete spatial grid in the domain of $\mathbf{x}$. Let $\phi(\mathbf{x}, \mathbf{n}\delta\mathbf{t}) = \phi_{\mathbf{x}}^{\mathbf{n}}$ where δt is the time step. Then for the spatial grid node $\mathbf{x} = (i, j), \phi$, can be calculated by:

$$\begin{array}{l} \phi_t^n + F|\nabla\phi_{\mathbf{x}}^n| = 0 \\ \frac{\phi_{\mathbf{x}}^{n+1} - \phi_{\mathbf{x}}^n}{\Delta t} + F|\nabla\phi_{i,j}^n| = 0 \\ \phi_{\mathbf{x}}^{n+1} = \phi_{\mathbf{x}}^n - \Delta t F|\nabla\phi_{i,j}^n|. \end{array} \tag{2.30}$$

F is a speed function which is given by:

$$F = \frac{1}{1 + |\nabla G_\sigma * I|^2}, \tag{2.31}$$

where G_σ is a Gaussian filter and I is an image.

The distance regularized level set evolution (DRLSE) was proposed in the reference [15]. Further, the DRLSE is explained. Let $\phi : \Omega \to \Re$ be a level set function (LSF) defined on a domain Ω. An energy function $\varepsilon(\phi)$ is defined by:

$$\varepsilon(\phi) = \mu\mathcal{R}_p(\phi) + \varepsilon_{ext}(\phi) \tag{2.32}$$

where $\mathcal{R}_p(\phi)$ is the level set regulation term defined in following, $\mu > 0$ is a constant, and $\varepsilon_{ext}(\phi)$ is the external energy that depends on the data of interest (e.g., an image for image segmentation application). The level set regulation term $\mathcal{R}_p(\phi)$ is defined by:

$$\mathcal{R}_p(\phi) \approx \int_\Omega p(|\nabla(\phi)|)d\mathbf{x} \tag{2.33}$$

where p is a potential (or energy density) $p : [0, \infty] \to \Re$.

A standard way to minimize an energy functional $\mathcal{F}(\phi)$ is to find the steady state solution of the gradient flow equation:

$$\frac{\partial\phi}{\partial t} = -\frac{\partial\mathcal{F}}{\partial\phi} \tag{2.34}$$

where $\partial\mathcal{F}/\partial\phi$ is the Gateaux derivative of functional $\mathcal{F}(\phi)$. The Gateaux derivative of the functional $\mathcal{R}_p(\phi)$ in Equation (2.33) is:

$$\frac{\partial\mathcal{R}_p(\phi)}{\partial\phi} = -div(d_p(|\nabla\phi|)\nabla\phi) \tag{2.35}$$

where $div(.)$ is the divergence operator and d_p is a function defined by:

$$d_p(s) = \frac{p'(s)}{s} \tag{2.36}$$

From Equation (2.32) and the linearity of Gateaux derivative, $\frac{\partial \varepsilon}{\partial t}$ can be obtained:

$$\frac{\partial \varepsilon}{\partial t} = \mu \frac{\partial \mathcal{R}_p}{\partial \phi} + \frac{\partial \varepsilon_{ext}}{\partial \phi} \tag{2.37}$$

where $\partial \varepsilon_{ext}/\partial \phi$ is the Gateaux derivative of the external energy functional ε_{ext} with respect to ϕ. Then, the gradient flow of the energy $\varepsilon(\phi)$ is

$$\frac{\partial \phi}{\partial t} = -\mu \frac{\partial \mathcal{R}_p}{\partial \phi} - \frac{\partial \varepsilon_{ext}}{\partial \phi} \tag{2.38}$$

which, combined with Equation (2.35), can be further expressed as:

$$\frac{\partial \phi}{\partial t} = \mu div(d_p(|\nabla \phi|)\nabla \phi) - \frac{\partial \varepsilon_{ext}}{\partial \phi} \tag{2.39}$$

Let I be an image on a domain Ω. Thus, a speed function (edge indicator) is defined by:

$$g = \frac{1}{1 + |\nabla G_\sigma * I|^2} \tag{2.40}$$

where G_σ is an Gaussian kernel with a standard deviation σ. It is used to smooth the image to reduce the noise.

For $\phi : \Omega \to \Re$, energy functional $\varepsilon(\phi)$ is defined by:

$$\varepsilon(\phi) = \mu \mathcal{R}_p(\phi) + \lambda \mathcal{L}_g(\phi) + \alpha \mathcal{A}_g(\phi) \tag{2.41}$$

where $\lambda > 0$ and $\alpha \in \Re$ are the coefficients of energy functional $\mathcal{L}_g(\phi)$ and $\mathcal{A}_g(\phi)$, which are defined by:

$$\mathcal{L}_g(\phi) = \int_\Omega g\delta(\phi)|\nabla \phi| d\mathbf{x} \tag{2.42}$$

and

$$\mathcal{A}_g(\phi) = \int_\Omega gH(-\phi) d\mathbf{x} \tag{2.43}$$

where δ and H are the Dirac delta function and Heaviside function, respectively. With the Dirac delta function δ and Heaviside function H in Equations (2.42) and (2.43) are replaced by δ_ε and H_ε, the energy functional $\varepsilon(\phi)$ is then approximated by:

$$\varepsilon_\varepsilon(\phi) = \mu \int_\Omega p(|\nabla(\phi)|) d\mathbf{x} + \lambda \int_\Omega g\delta_\varepsilon(\phi)|\nabla \phi| d\mathbf{x} + \alpha \int_\Omega gH_\varepsilon(-\phi) d\mathbf{x}. \tag{2.44}$$

This energy functional can be minimized by solving the following gradient flow:

$$\frac{\partial \phi}{\partial t} = \mu div(d_p(|\nabla \phi|)\nabla \phi) + \lambda \delta_\varepsilon(\phi) div(g \nabla \phi / |\nabla \phi|) + \alpha g \delta_\varepsilon, \tag{2.45}$$

where δ_ε is a dirac delta function.

2.3 Takagi-Sugeno fuzzy inference

Fuzzy inference has been successfully applied in fields such as automatic control, data classification, decision analysis, expert systems, and computer vision. Fuzzy inference (reasoning) is the actual process of mapping from a given input to an output by using fuzzy logic.

The fuzzy inference introduced by Takagi and Sugeno is a powerful tool for modeling complex nonlinear systems [30]. The Takagi-Sugeno (T-S) fuzzy inference is a multimodel approach in which linear local models associated with the T-S rules are combined to describe the global behavior of the system. The T-S rules have high degrees of freedom to improve performance that make them possible to express complicated behaviors with a small number of rules which consequently, has made the 1st order T-S fuzzy popular in the applications of fuzzy logic.

To compute the output of this fuzzy inference given the inputs, the steps of fuzzy inference are given as follows:

1. Determining a set of fuzzy rules.
2. Fuzzifying the inputs using the input membership functions.
3. Combining the fuzzified inputs according to the fuzzy rules to establish a rule strength (fuzzy operations).
4. Finding the consequence of the rule by combining the rule strength and the output membership function (implication).
5. Combining the consequences to get an output distribution (aggregation).
6. Defuzzifying the output distribution (this step is only if a crisp output (class) is needed).

From here on, the T-S fuzzy model will be explained. It is suggested that the fuzzy implication R is of the format:

$$R : \text{If } f(x_1 \text{ is } A_1, ..., x_k \text{ is } A_k) \text{ then } y = g(x_1, ..., x_k), \tag{2.46}$$

where y represents variable of the consequence whose value which is inferred. $x_1 - x_k$ are variables of the premise that also appear in part of the consequence. $A_1 - A_k$ represent fuzzy sets with linear membership functions which then represent a fuzzy

subspace in which the implication R which can be applied for reasoning. f and g represent logical function that connects the propositions in the premise and function that implies the value of y when $x_1 - x_k$ satisfies the premise, respectively.

In the premise A_i is equal to X_i, for some values of i where X_i is the universe of discourse of x_i, this term is omitted and x_i is unconditioned. In the sequel "and" connectives are used in premise and adopt a linear function in the consequence, so an implication is written as:

$$R : \text{If } x_1 \text{ is } A_1 \text{ and } ... \text{ and } x_k \text{ is } A_k \text{ then } y = p_0 + p_1 x_1 + ... + p_k x_k. \tag{2.47}$$

The algorithm of the T-S fuzzy inference will be explained. Suppose that the implication $R^i (i = 1, ..., n)$ is in the above format. When given $(x_1 = x_1^0, ..., x_1 = x_k^0)$ where $x_1^0 - x_k^0$ are singletons, the value of y is inferred as follows:

1. For each implication R^i, y^i is calculated by the function g^i in the consequence

$$\begin{array}{rcl} y^i & = & g^i(x_1^0, ..., x_k^0) \\ & = & p_0^i + p_1^i x_1^0 + ... + p_k^i x_k^0. \end{array} \tag{2.48}$$

2. The truth value of the proposition $y = y^i$ is calculated by the equation

$$\begin{array}{rcl} |y = y^i| & = & |x_1^0 \text{ is } A_1^0 \text{ and } ... \text{ and } x_k^0 \text{ is } A_k^i| \wedge |R^i| \\ & = & (A_1^i(x_1^0) \wedge ... \wedge A_k^i(x_k^0)) \wedge |R^i|, \end{array} \tag{2.49}$$

   where $|*|$ means the truth value of proposition $*$ and $\wedge$ stands for min operation, and $|x^0 \text{ is } A| = A(x^0)$, i.e., the grade of the membership of x_0. For simplicity, it is assumed:

$$|R^i| = 1 \tag{2.50}$$

   so the truth value of the consequence obtained is

$$|y = y^i| = A_1^i(x_1^0) \wedge ... \wedge A_k^i(x_k^0). \tag{2.51}$$

3. The final output y inferred from n implications is given as the average of all y^i with $|y = y^i|$:

$$y = \frac{\Sigma |y = y^i| \times y^i}{\Sigma |y = y^i|}. \tag{2.52}$$

The T-S fuzzy inference has several parameters that need to be identified. A fuzzy inference of Equation (2.47) is considered. The algorithm of the identification of implication is divided into three steps, corresponding to the three items, by using the input-output data of an objective system. They are: choice of premise variables, premise parameter identification, and consequence parameters identification.

Optimum consequence parameters should minimize the performance index, provided that both the premise variables and parameters are given. The performance index has been defined above as "a root mean square of the output errors", which means the differences between the output data of an original system and those of a model. Let a system be represented by the following implications:

$$\begin{array}{l} R^1 : \text{If } x_1 \text{ is } A_1^1 \text{ and } ... \text{ and } x_k \text{ is } A_k^1 \text{ then } y = p_0^1 + p_1^1 x_1 + ... + p_k^1 x_k \\ \vdots\vdots \\ R^n : \text{If } x_1 \text{ is } A_1^n \text{ and } ... \text{ and } x_k \text{ is } A_k^n \text{ then } y = p_0^n + p_1^n x_1 + ... + p_k^n x_k \end{array} \tag{2.53}$$

then the output y for the input $(x_1, ..., x_k)$ is obtained as

$$y = \frac{\sum_{i=1}^{n}(A_1^i(x_1) \wedge ... \wedge A_n^i(x_n))(p_0^i + p_1^i x_1 + ... + p_k^i x_k)}{\sum_{i=1}^{n}(A_1^i(x_1) \wedge ... \wedge A_n^i(x_n))}. \tag{2.54}$$

Let β_i be

$$\beta_i = \frac{(A_1^i(x_1) \wedge ... \wedge A_n^i(x_n))}{\sum_{i=1}^{n}(A_1^i(x_1) \wedge ... \wedge A_n^i(x_n))} \tag{2.55}$$

then

$$\begin{array}{rcl} y & = & \sum_{i=1}^{n} \beta_i (p_0^i + p_1^i x_1 + ... + p_k^i x_k) \\ & = & \sum_{i=1}^{n} (p_0^i \beta_i + p_1^i x_1 \beta_i + ... + p_k^i x_k \beta_i). \end{array} \tag{2.56}$$

When a set of input-output data $x_{1j}, x_{2j}, ..., x_{kj} \rightarrow y_j (j = 1...m)$ is given, the consequence parameters $p_0^i, p_1^i, ..., p_k^i (i = 1...n)$ can be obtained by the least squares method using Equation (2.56).

Let $X(m \times n(k+1)$ matrix), $Y(m$ vector) and $P(n(k+1)$ vector) be

$$X = \begin{bmatrix} \beta_{11} & ... & \beta_{n1} & x_{11}\beta_{11} & ... & x_{11}\beta_{n1} & ... & x_{k1}\beta_{11} & .... & x_{k1}\beta_{n1} \\ \vdots & \vdots & \vdots & \vdots & \vdots & \vdots & \vdots & \vdots & \vdots & \vdots \\ \beta_{1m} & ... & \beta_{nm} & x_{1m}\beta_{1m} & ... & x_{1m}\beta_{nm} & ... & x_{km}\beta_{1m} & .... & x_{km}\beta_{nm} \end{bmatrix} \tag{2.57}$$

where

$$\beta_{ij} = \frac{(A_{i1}(x_{1j}) \wedge ... \wedge A_{ik}(x_{kj}))}{\sum_j (A_{i1}(x_{ij}) \wedge ... \wedge A_{ik}(x_{kj}))} \tag{2.58}$$

$$Y = [y_1, ..., y_m]^T \tag{2.59}$$

$$P = [p_0^1, ..., p_0^n, p_1^1, ..., p_1^n, ..., p_k^1, ..., p_k^n]^T. \tag{2.60}$$

Then the parameter vector P is calculated by:

$$P = (X^T X)^{-1} X^T Y. \tag{2.61}$$

2.4 Particle swarm optimization

Particle swarm optimization (PSO) was first introduced by Kennedy and Eberhart in 1995 [32]. It is inspired by swarm intelligence and general theories such as bird flocking, fish schooling and human behavior. PSO can be applied to various function optimization problems, or problems that can be transformed to the function optimization. PSO has exhibited good performance across a wide range of application.

PSO has several advantages, i.e., it comprises a very simple concept and paradigms can be implemented in a few lines of computer code. It also requires only primitive mathematical operators, and is computationally inexpensive in terms of both memory requirements and speed. PSO can be applied to optimization problems of large dimensions, often producing quality solutions more rapidly than alternative methods.

The PSO model consists of a swarm of particles, which are initialized with a population of random candidate solutions. Each particle has a position represented by a position-vector $\mathbf{z}_\ell(t)$ and a velocity represented by a velocity-vector $\mathbf{v}_\ell(t)$.

During each generation, each particle is accelerated towards the particle's previous best position and the global best position. They move iteratively through the d-dimension problem space to search for new solutions, where the fitness, f, can be calculated as a certain qualities measure. A particle decides where its own experience, which is memory of its best past position, and the experience of its most successful particle in the swarm. The particle searches the solutions in the problem space with a range $[-u, u]$.

Generally, the algorithm of PSO consists of two operators. The first operator in PSO is an update of these particle velocities. At each iteration a new velocity value for each particle is calculated based on its current velocity, the distance from its previous best position, and the distance from the global best position. An update of the general particle velocity is defined by:

$$\begin{aligned}&\mathbf{v}_\ell(t+1) = w\mathbf{v}_\ell(t) + c_1 R_1(t)[\mathbf{Z}_\ell(t) - \mathbf{z}_\ell(t)] + c_2 R_2(t)[\hat{\mathbf{Z}}_\ell(t) - \mathbf{z}_\ell(t)] \\ &(\ell = 1, 2, ..., G),\end{aligned} \tag{2.62}$$

where G is the number of particles, t is an iteration number, w is an inertia weight, c_1 and c_2 are acceleration coefficients, and $R_1(t)$ and $R_2(t)$ are uniformly distributed random variables.

The inertia weight w is multiplied by the previous velocity in the standard velocity equation, and is linearly decreased throughout the running program. A non zero inertia weight introduces a preference for the particle to continue moving in the same direction it was going on the previous iteration. Empirical results have shown a constant inertia of $w = 0.7298$ and acceleration coefficients $c_1 = c_2 = 1.49618$ [63].

The standard version of the PSO has a tendency to explode as oscillations gradually become wider, unless a method is applied for damping the velocity. The usual method for preventing explosion is simply to define a parameter V_{max} and to prevent

the velocity from exceeding it on each dimension d for individual ℓ. Typically V_{max} is set to Z_{max}, the maximum initialization range of $z_{\ell d}$

$$\begin{array}{l} \text{If } v_{\ell d} > V_{max} \text{ then } v_{\ell d} = V_{max} \\ \text{If } v_{\ell d} < -V_{max} \text{ then } v_{\ell d} = -V_{max}. \end{array} \tag{2.63}$$

Each particle remembers its own best position which is called "personal best position" $\mathbf{Z}_\ell(t)$ defined by:

$$\mathbf{Z}_\ell(t+1) = \begin{cases} \mathbf{z}_\ell(t+1), \text{if} f(\mathbf{z}_\ell(t+1)) < f(\mathbf{Z}_\ell(t)) \\ \mathbf{Z}_\ell(t). \end{cases} \tag{2.64}$$

The best position among the particles which is called "global best" is calculated by:

$$\hat{\mathbf{Z}}(t) = \arg\min_{z \in GB} f(\mathbf{Z}), GB = \{\mathbf{Z}_1(t), ..., \mathbf{Z}_G(t)\}, \tag{2.65}$$

where $f(\cdot)$ is an objective function.

The second operator in PSO is an update of particle position. The new velocity is used to update a particle position which is given by:

$$\mathbf{z}_\ell(t+1) = \mathbf{z}_\ell(t) + \mathbf{v}_\ell(t+1). \tag{2.66}$$

The process is then iterated a set number of times, or until a minimum error is achieved.

The framework of the PSO algorithm is summarized as follows:

1. The position of particles $\mathbf{z}_\ell(t)$ for $t = 0$ are randomly initialized within the hypercube of feasible space.

2. Evaluate the fitness of each particle $\mathbf{z}_\ell(t)$.

3. Compare the performance of each individual to update its (personal) best performance by using Equation (2.64).

4. Compare the performance of each particle to update the global best particle by using Equation (2.65).

5. Update the velocity of the particle according to Equation (2.62).

6. Update each particle to a new position according to Equation (2.66).

7. Stop if the stop criterion is satisfied (convergence); otherwise, increase t by using $t = t + 1$ and go to step 2.

Chapter 3

Combining PSO and Fuzzy Inference for Detecting Coronary Plaque Boundary in IVUS Image

3.1 Background

Acute coronary syndromes (ACS) is one of the leading causes of hospitalization in the world. ACS occurs when the blood supplied to the heart muscle is suddenly blocked. Restricted blood flow, which is caused by atherosclerosis, can damage organs and stop them from functioning properly.

Atherosclerosis occurs when arteries become clogged up by fatty substances called plaque. The plaque builds up inside the coronary arteries. ACS is treatable if diagnosed quickly. The intravascular ultrasound (IVUS) method [34] provides a real time cross-sectional image of a coronary artery in vivo. Medical doctors use IVUS images for tissue characterization and plaque volume calculation. For this purpose, the detection of the inner and outer plaque boundaries are required.

Currently, these boundaries of plaque are manually detected and the area of that plaque is also evaluated manually by a medical doctor. After that, the volume of the plaque is estimated by integrating the detected areas. However, the detection of plaque boundaries is difficult and time consuming. This is not only because a large number of the IVUS images must be processed, but also because recognizing the boundaries of plaque is very hard due to a heavy speckle noise. To reduce the workload of a medical doctor, an automatic plaque boundary detection method with high accuracy is strongly required.

Ruiz et al. have proposed in the reference [8], a probabilistic segmentation for identification of luminal boundary (LB), and Gil et al. have also proposed in the reference [9], a statistical strategy for anisotropic adventitial modelling. However, those methods do not automatically work because the method [8] needs an initial area created by a user, and the method [9] needs a set of training data manually

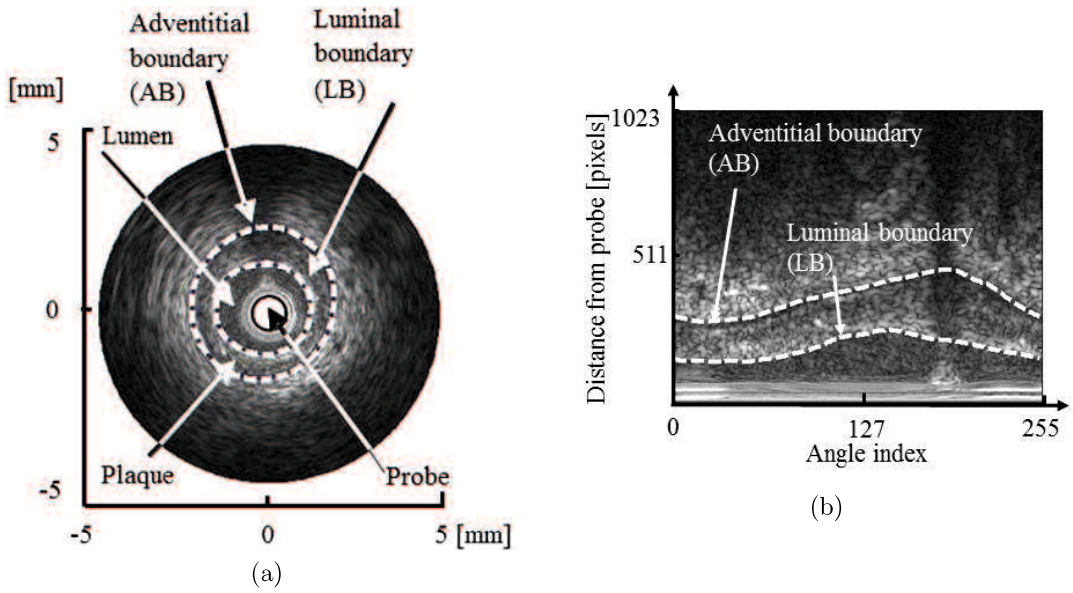

Figure 3.1: IVUS B-mode image. (a) B-mode image in the Cartesian coordinates. (b) B-mode image in the polar coordinates.

segmented by an expert. The shape driven segmentation method proposed by Unal et al. [10] also needs a set of training data which is manually segmented by an expert.

Adame et al. [64] have proposed an automatic segmentation and plaque characterization method, but it is not fully automatic. It still requires a center point in lumen, a seed point inside the lipid core and a circle that surrounds the vessel, which have to be decided by a user.

Several automatic plaque boundary detection methods have been proposed. They do not need a set of training data nor any initial area. In the automatic plaque boundary methods [11, 12], the coronary plaque boundaries were detected by piecewise polynomials approximated via a fuzzy inference-based method, in which the Takagi-Sugeno (T-S) fuzzy inference [30] was used.

Fuzzy inference has several advantages over the conventional methods in the boundary detection of image, e.g., Sobels method, Prewitts method, and Roberts method [31]. The fuzzy inference can handle problems that happen because of imprecise, noisy, in-consistent and incomplete data sets [29]. Additionally, the T-S fuzzy inference has been successfully applied in many areas. Since IVUS images often have noise and the plaque boundaries are often missing in several areas, the T-S fuzzy inference has been employed to restore the missing boundaries by inference.

The coefficients of the polynomials were determined by the weighted least square method using the separability of image, which is a kind of statistical measure for the detection of the edge of the image. The candidates for the boundaries are detected by using a statistical discriminant measure (called separability [60]), which

is insensitive to noisy and blurred edges, and can detect an edge between different texture regions.

In the reference [11], membership functions (MSFs) in the antecedent parts of the fuzzy rules were adaptively allocated by using the information of the seed points given by a medical doctor. In the reference [12], the seed points were automatically determined by the weighted image separability and heuristic rules.

Since the IVUS image has heavy speckle noise, the normal Perona Malik diffusion (PMD) filter [24] was used in this chapter. The normal PMD not only reduces speckle noise but also effectively enhances the edges of image.

In those methods, the accuracy of the plaque boundary detection is influenced by the parameters of the MSFs. The parameter tuning of the MSFs can be regarded as an optimization problem. However, this optimization was not done in the reference [11].

Particle swarm optimization (PSO) is one of the methods of global optimization [32], which is used for function optimization with multiple local solutions. PSO is especially useful when other techniques such as gradient descent or direct analytical discovery are not applicable. In those cases genetic algorithm (GA) is another alternative to be applied, but PSO yields faster convergence than GA because of the balance between exploration and exploitation in the search space [33].

For these reasons, a method for coronary plaque boundary detection in an IVUS image is proposed by combining PSO and the T-S fuzzy inference.

3.2 Proposed method

This chapter will explain how to tune the parameters of MSFs of the T-S fuzzy inference by using PSO. After that, the T-S fuzzy inference is applied to approximate coronary plaque boundaries. This chapter is divided into three sections, which are the placement of seed points by heuristic rules, the boundary detection procedure and MSFs parameter tuning by using PSO.

3.2.1 Placement of seed points by using heuristic rules

The following is the concrete process of placement seed points by heuristic rules [12]:

1. Input B-mode image in Cartesian coordinate as shown on Figure 3.1 (a), and then it will be transformed into polar coordinates as shown on Figure 3.1 (b). The horizontal axis in Figure 3.1 (b) corresponds to the angle index in clockwise starting from three o'clock direction of the IVUS image of Figure 3.1 (a). The vertical one corresponds to the distance from the probe located at the center of the IVUS image of Figure 3.1 (a). Figure 3.1 (b) consists of 256 lines in radial direction(x-axis) and one line consists of 1,024 pixels (y-axis). The angle between lines is 1.41 deg and the distance between pixels on a line is 3.91μ m.

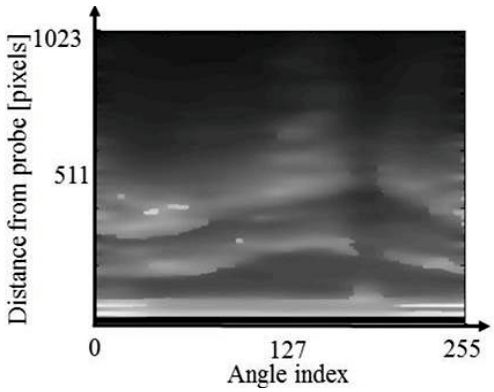

Figure 3.2: Speckle noise filtering by the normal PMD filter.

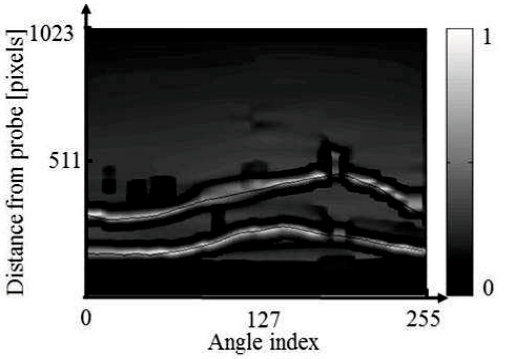

Figure 3.3: Weighted separability of IVUS image in Figure 3.2.

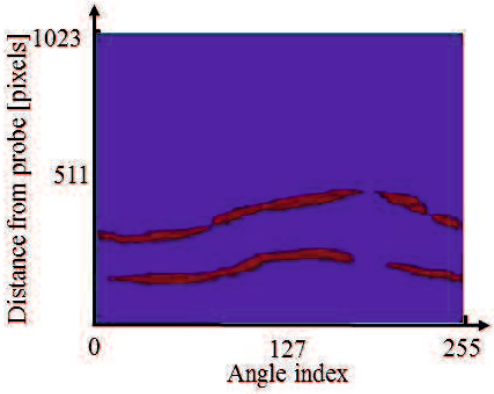

Figure 3.4: Binary image obtained by threshold processing for Figure 3.3.

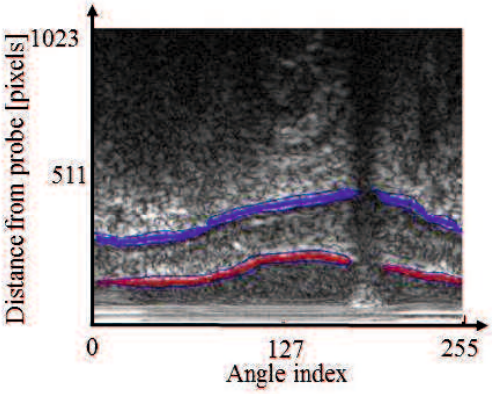

Figure 3.5: Candidates of seed points.

2. The normal PMD filter is used to reduce speckle noise.
   Figure 3.2 shows the result of an IVUS image in Figure 3.1 (b) after applying the normal PMD filter. It can been seen that the image around the boundary area keeps sharp and smooth in the other area. However, the boundaries cannot be preserved in several areas. It means that the normal PMD filter can only reduce speckle noise and preserve the plaque boundary in several areas.

3. The weighted image separability is used for detecting candidates of plaque boundaries.
   Figure 3.3 shows an image separability of Figure 3.2. Each pixel of its image corresponds to the ratio η_{ij}^{w}. The brightness of each pixel in the image is a value of separability η_{ij}^{w} for that pixel. The separability η_{ij}^{w} of pixel $\mathbf{s} = (i, j)$ takes a large value around the regional edge of the image. That is, a line of

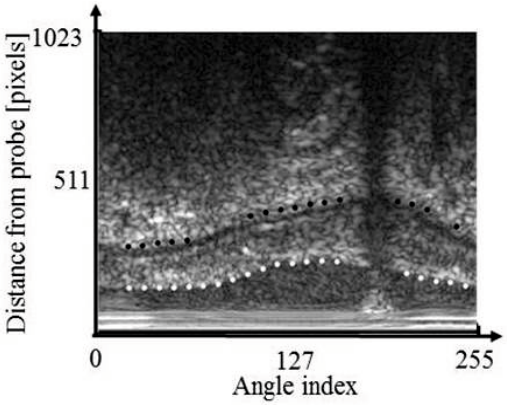

Figure 3.6: Final seed points.

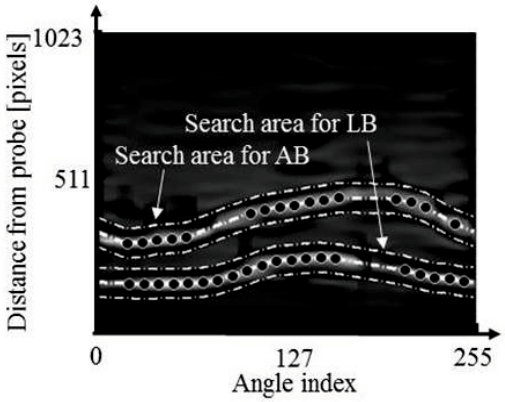

Figure 3.7: Primitive boundaries and specified search areas.

white pixels can then be a candidate of a plaque boundary.

4. Binary operation is run.
   Figure 3.4 shows a binary image by the threshold processing for image of Figure 3.3. Here, let the threshold value of the weighted separability be ξ. By changing the value of ξ from ξ_{low} to ξ_{high} at regular intervals, a binary image with each threshold value of ξ, such as Figure 3.4 is obtained. The points on the central line of the dark red colored region of Figure 3.5 are regarded as candidates of the seed points. The candidates are detected by the line scanning in parallel to x-axis. When two regions are detected by the line scanning, the centers of the regions are regarded as the candidates. The candidates of the seed points for all the binary images are superimposed on Figure 3.5.

The optimum threshold value of this has to be set to obtain the best binary image of Figure 3.4 for detecting the final seed points. In this process, the binary images are evaluated by using the following score S:

$$G_1 = \begin{cases} \frac{1}{N_{r1}} n_r, 0 \leq n_r < N_{r1} \\ -\frac{1}{N_{r2}-N_{r1}} n_r + \frac{N_{r2}}{N_{r2}-N_{r1}}, N_{r1} \leq n_r < N_{r2} \\ 0, N_{r2} \leq n_r. \end{cases} \tag{3.1}$$

$$G_2 = \begin{cases} 0, 0 \leq n_p < N_{p1} \\ \frac{1}{N_{p2}-N_{p1}} n_p - \frac{N_{p1}}{N_{p2}-N_{p1}}, N_{p1} \leq n_p < N_{p2} \\ -\frac{1}{N_{p3}-N_{p2}} n_p + \frac{N_{p3}}{N_{p3}-N_{p2}}, N_{p2} \leq n_p < N_{p3} \\ 0, N_{p3} \leq n_p. \end{cases} \tag{3.2}$$

$$G_3 = \begin{cases} 0, 0 \leq l_r < l_{r1} \\ \frac{1}{L_{r2}-L_{r1}} l_r - \frac{L_{r1}}{L_{r2}-L_{r1}}, L_{r1} \leq l_r < l_{r2} \\ -\frac{1}{L_{r3}-L_{r2}} l_r + \frac{L_{r3}}{L_{r3}-L_{r2}}, L_{r2} \leq l_r < L_{r3} \\ 0, L_{r3} \leq l_r. \end{cases} \tag{3.3}$$

$$S = G_1 G_2 G_3, \tag{3.4}$$

where G_1, G_2 and G_3 are concerned with the membership functions for the number of region n, the number of pixels and the total length of region, respectively.

The sets of parameter $\{N_{r1}, N_{r2}\}, \{N_{p1}, N_{p2}, N_{p3}\}$ and $\{L_{r1}, L_{r2}, L_{r3}\}$ define the figure of each membership functions and are empirically determined by analyzing hundreds of real IVUS images. The image with the maximum score of S is selected to obtain Figure 3.4. The color-coded regions in Figure 3.5 are classified either to region LB or AB through majority decision by using the class information of the candidates of the seed points.

Finally, the points on the central line of each region of Figure 3.5 are regarded as the final seed points to get Figure 3.6. The selected seed points are linearly interpolated, and the boundary extraction areas are allocated around this linearly interpolated curve with weights of the following Gaussian kernel function:

$$f(y) = exp(-\frac{(y - y(i))^2}{2\delta^2} \tag{3.5}$$

$$\delta = \frac{y_{out}(i) - y_{in}(i)}{3}, \tag{3.6}$$

where $y_{in}(i)$ and $y_{out}(i)$ are lines obtained by the interpolation for LB and AB, respectively. The allocated areas for the boundary detection are shown in Figure 3.7.

3.2.2 Boundary detection procedure

This section will describe a procedure of plaque boundary detection. The boundary detection procedure is briefly summarized as follows:

1. Seed points are roughly placed automatically on the B-mode image as shown in Figure 3.6, to get search areas described in Section 3.2.1.

2. The plaque boundary is inferred by using the T-S fuzzy inference. The boundary is piecewise approximated by the following series of fuzzy rules:

$$\text{If } x_i \text{ is } A_u \text{ Then } f_i(x_i) = a_u x_i + b_u, \tag{3.7}$$

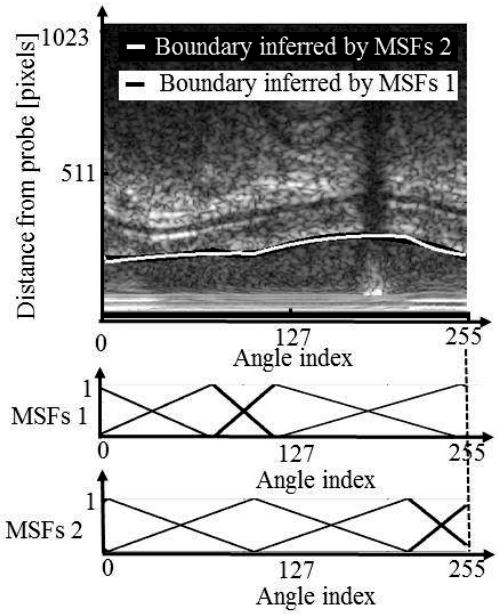

Figure 3.8: Two solutions of the locations of the MSFs for LB and the boundaries detected by PSO.

where A_u is a fuzzy set with the MSF $\mu_u(x_i), x_i$ corresponding to the angle index, and $f_u(x_i)$ is a linear function. In the antecedent part of the fuzzy rule, the complementary triangular MSFs are used. The u-th rule thus stands for a piecewise approximation of the plaque boundary in the interval $[z_{u-1}, z_{u+1}]$ where z_{u-1} and z_{u+1} are MSFs locations. The inferred boundary is given by:

$$y(x) = \mu_u(x_i) f_u(x_i) + \mu_{u+1}(x_i) f_{u+1}(x_i), \tag{3.8}$$

3. The optimum coefficients in the consequent part of the fuzzy rule are determined by using the weighted least square method (WLSM), to minimize the following weighted error criterion:

$$E = \sum_{J=0}^{J-1} \sum_{I=0}^{I-1} \eta_{\mathbf{s}}^{w} (y_j - \hat{y}_j(x_i))^2, \tag{3.9}$$

where $\eta_{\mathbf{s}}^{w}$ is a weighted image separability of pixel $\mathbf{s} = (i, j)$. In this method, $\eta_{\mathbf{s}}^{w}$ inside the search areas (see Figure 3.7.) are used as the weights for WLSM.

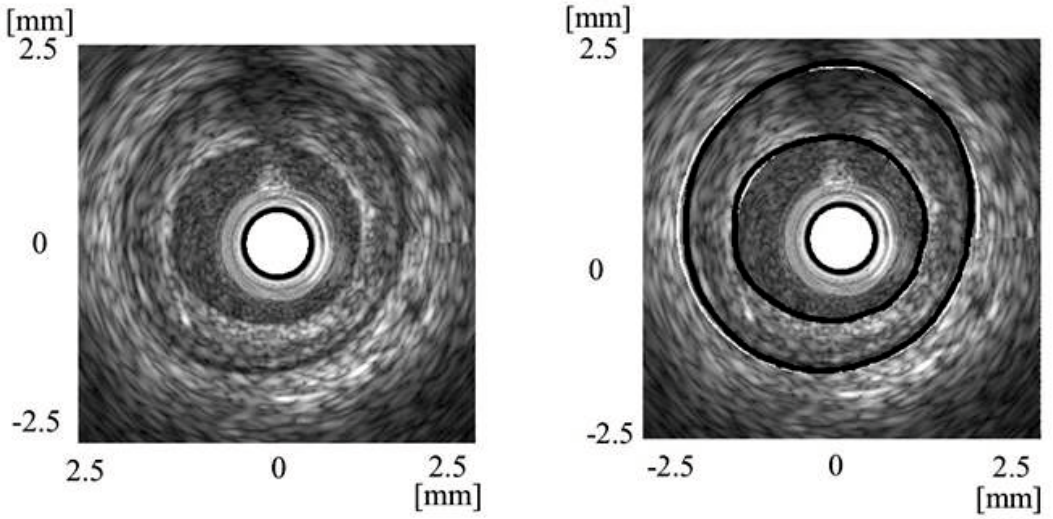

(a) (b)

Figure 3.9: Boundary detection results by the proposed method for image 1. The white and black lines indicate the detected boundaries and the desired boundaries, respectively. (a) IVUS image to be processed. (b) Boundary detection results.

3.2.3 Membership function parameter tuning by using particle swarm optimization

PSO is used for tuning the parameters of MSFs. The positions of MSFs are decided by PSO based on the evaluation of the objective function of Equation (3.10). The tuning procedure of the MSFs using PSO is briefly summarized as follows:

1. Generate the initial positions of the particles $\mathbf{z}_\ell(0) = (\mathbf{z}_{\ell 1}(0), \mathbf{z}_{\ell 2}(0), ..., \mathbf{z}_{\ell p}(0))$ where p is the number of MSFs.

2. Determine the consequence parameters a_u and b_u of the T-S fuzzy inference of Equation (3.8) by using the weighted least square method (WLSM) which minimize Equation (3.9).

3. Evaluate the values of the following objective function:

$$E(\mathbf{z}_\ell(t)) = \sqrt{\frac{\sum_{j=0}^{J-1}\sum_{i=0}^{I-1} \eta_{\mathbf{s}}^{w}(y_j - \hat{y}_j(x_i; \mathbf{z}_\ell(t))^2}{\sum_{j=0}^{J-1}\sum_{i=0}^{I-1} \eta_{\mathbf{s}}^{w}}}, \tag{3.10}$$

and then calculate the personal best position for each particle, and the overall

global best position of all the particles.

4. Update the velocity and position of the particle using Equations (2.62) and (2.66), respectively.

5. If the global best position does not change during the fixed number of iterations, then the worst 10% particles are replaced with the new particles randomly selected.

6. Check the terminal conditions. If one of the terminal conditions is satisfied, then go to step 2.

7. Finish the search.

3.3 Experimental results and discussion

In the experiments, three IVUS images were used. The proposed method uses PSO to tune the parameters of MSFs. To evaluate the performance of the proposed method, it was compared with the conventional method [11], [48] and the gradient descent tuning method.

The seed points are automatically placed by the method [12]. The parameters of PSO of Equation (2.62) are assigned as $s = 10$, $w = 0.7298$, and $c_1 = c_2 = 1.49618$ accordingly to the reference [63]. In this experiment, the maximum iteration is set to 100. If the improvement of the global best position is less than 0.0001 during 20 iterations, then the search is terminated.

PSO is based on a stochastic method, and so the processing for each image was repeated 5 times (5 runs). The desired boundaries were decided by an experienced medical doctor based on the difference of image brightness.

Tables 3.1 and 3.2 show the values of the objective function of Equation (3.10) for LB and AB, respectively. Good performance of the proposed method can be seen. In the proposed method, the different solutions (the locations of the MSF locations) were obtained in different runs. This indicates that the objective function has local minima. Figure 3.8 shows the two solutions of the locations of MSFs for LB.

The proposed method cannot move further than the local minimum, but the values of the objective function of the proposed method are better than those of the conventional method [11, 48] and the gradient descent method.

Figures 3.9, 3.10 and 3.11 show the detection results by the proposed method for each image. It can be observed from Figures 3.9, 3.10 and 3.11 that the detected

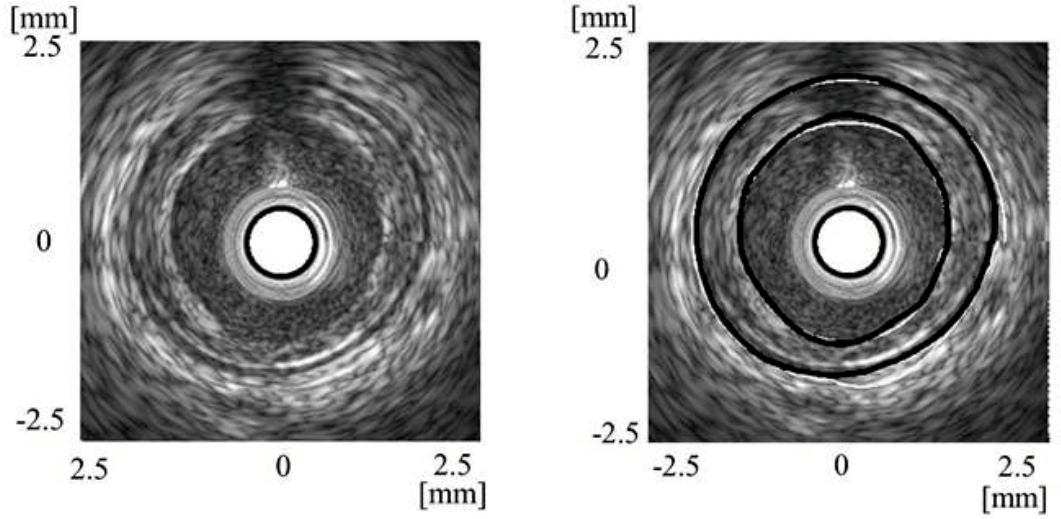

(a) (b)

Figure 3.10: Boundary detection results by the proposed method for image 2. The white and black lines indicate the detected boundaries and the desired boundaries, respectively. (a) IVUS image to be processed. (b) Boundary detection results.

boundaries (white) by the proposed method are close to the desired boundaries (black). These results show that the proposed method works well.

Tables 3.3 and 3.4 show the root mean square errors (RMSEs) between the desired and the extracted boundaries. The average of RMSEs of the proposed method is better than our previous method for the most part for LB, but is not always better than the previous method for AB.

The average of RMSEs of the proposed method for all data is 1.86×10^{-2} mm for LB and 3.36×10^{-2} mm for AB. Taking into account that the diameter of the coronary artery is around 5 mm, the above RMSEs can be considered as very small, and so it can be concluded that the accuracy of the proposed method is adequate. Additionally, the proposed method works automatically and does not need any set of training data, seed points, nor initial areas which were given manually in the conventional methods.

However, this method has problems. From Tables 3.2 and 3.4, it can be seen that there is a contradiction between the RMSEs and the values of the objective function, that is, minimizing the objective function does not always lead to minimizing the RMSE. This is caused by the plaque boundaries which cannot be preserved after applying the normal PMD filter. As a result, the desired boundaries (black lines) are not always in around the center of the area with high weighted image separability as shown in Figure 3.3. This contraction needs to be solved in future works.

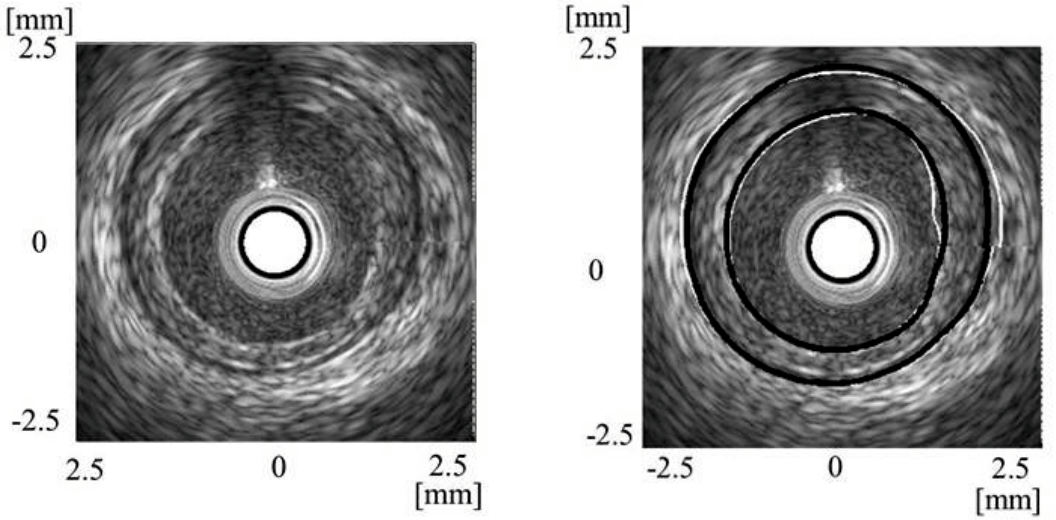

(a) (b)

Figure 3.11: Boundary detection results by the proposed method for image 3. The white and black lines indicate the detected boundaries and the desired boundaries, respectively. (a) IVUS image to be processed. (b) Boundary detection results.

Table 3.1: Values of objective function of luminal boundary (LB) detection results.

Method	Conventional Method		Gradient Descent Method	Proposed Method Averaged
	[48]	[11]		
Image 1	45.63	36.82	36.80	**36.72**
Image 2	44.91	41.69	47.07	**40.66**
Image 3	47.78	44.48	44.30	**40.85**

Table 3.2: Values of objective function of adventitial boundary (AB) detection results.

Method	Conventional Method		Gradient Descent Method	Proposed Method Averaged
	[48]	[11]		
Image 1	49.06	47.40	47.35	**46.81**
Image 2	46.76	47.09	47.07	**46.19**
Image 3	**41.73**	51.40	51.30	47.88

Table 3.3: RMSEs of luminal boundary (LB) detection results (μm).

Method	Conventional Method		Gradient Descent Method	Proposed Method Averaged
	[48]	[11]		
Image 1	26.45	13.72	13.70	**12.21**
Image 2	25.74	20.01	19.88	**19.86**
Image 3	26.74	28.04	27.58	**23.81**

Table 3.4: RMSEs of adventitial boundary (AB) detection results (μm).

Method	Conventional Method		Gradient Descent Method	Proposed Method Averaged
	[48]	[11]		
Image 1	33.20	28.40	**28.31**	28.46
Image 2	**26.83**	30.18	30.26	40.10
Image 3	34.36	35.39	35.32	**33.20**

3.4 Chapter conclusion

This chapter has explained a method for coronary plaque boundary detection in an IVUS image by combining PSO and the T-S fuzzy inference.

The proposed method gives better performance than previous works [11, 48] and the gradient descent method in terms of the detection accuracy.

The proposed method has more advantages over the methods in the references [8, 9, 10]; it works automatically which does not need any set of training data, seed points, nor initial areas which were given manually in the conventional methods.

However, the proposed method in this chapter has several weaknesses. The first weakness is that the proposed method needs to generate seed points to detect coronary plaque boundaries. If the seed points are placed in wrong position, the accuracy decreases. The second weakness is that the coronary plaque boundaries cannot be preserved in several region after applying the normal PMD filter.

Chapter 4

Modified PMD Filter and Hybrid Method for Detecting Coronary Plaque Boundary

4.1 Background

Acute coronary syndrome (ACS) happens when the heart is not getting enough oxygen-rich blood. This is caused when the coronary arteries are narrowed or blocked by a rupture of vulnerable plaque as shown in Figure 4.1, which is built up inside the coronary arteries. If the heart does not get enough oxygen, it can cause a heart attack. The plaque may also block blood supply to the brain, which could trigger a stroke.

ACS can be treated if it is diagnosed quickly. Intravascular ultrasound (IVUS) method is one of technologies which is used to diagnose ACS. IVUS method is a medical imaging technique which allows to see the inside of the blood vessel, visualizing the coronary plaque in the living individual [34]. IVUS image is not only used for ACS diagnosis but also it is used for planing the ACS treatment. A medical doctor uses IVUS images for the quantitative assessment of the compositions of coronary plaque, and plaque volume calculation for a diagnosis of ACS. For this purpose, the plaque boundaries (the luminal boundary (LB) and the adventitial boundary (AB) of the coronary plaque) are required to be detected and evaluated precisely. After that, the volume of the plaque is estimated by integrating the calculated areas.

Plaque boundary detection is however a very hard and time consuming work for medical doctors. This is not only because the plaque boundary of the IVUS image is difficult to be identified, but also because the number of IVUS images to be processed by a medical doctor is very large. For those reasons, an automatic plaque boundary detection method with high accuracy is strongly required.

The other problem of the plaque boundary detection in IVUS image is that a

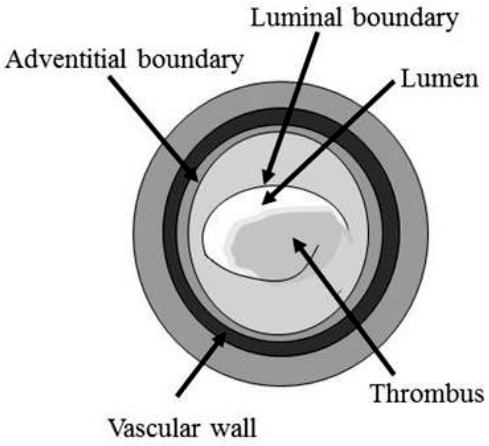

Figure 4.1: Illustration of ruptured plaque.

region of the IVUS image behind the guide wire often becomes shadowed, and then it contains no texture information there as shown in Figure 4.2. Thus the existing methods fail to detect the plaque boundaries on the guide wire shadow area.

Several algorithms for the coronary plaque boundary have been proposed in the references [9, 10, 12, 5, 11]. Gil et al. [9] presented a statistical strategy for anisotropic adventitial modelling. This method however does not work automatically because the method [9] needs a set of training data manually segmented by an expert. Unal et al. [10] has proposed a shape driven segmentation method. This method also needs a set of training data which is manually segmented by an expert.

Several automatic plaque boundary methods also have been proposed in the references [12, 5, 11]. Those methods could significantly reduce the workload of medical doctors. However, those methods [11, 12, 5] needed the seed points to detect the plaque boundary. If the seed points were placed in the wrong position the accuracy of the methods would be reduced drastically.

Since the IVUS image is very grainy which is caused by heavy speckle noise, the speckle noise in the IVUS image has to be reduced and coronary plaque boundary boundaries have to be enhanced. The PMD filter has several advantages over the other methods as explained in Chapter 1. However, when the normal PMD filter is applied to the IVUS image, the coronary plaque boundary cannot be preserved in several areas as shown in Chapter 3. The diffusion direction and its strength are very important factors to enhance the image edges and to reduce the speckle noise. This is because the diffusion direction and its strength in the normal PMD filter used in the references [11, 12] have not been set properly and the plaque boundary direction in medical image was not considered.

Therefore, this paper proposes a modified PMD filter to reduce the speckle noise and enhance a coronary plaque boundary by considering the plaque direction in

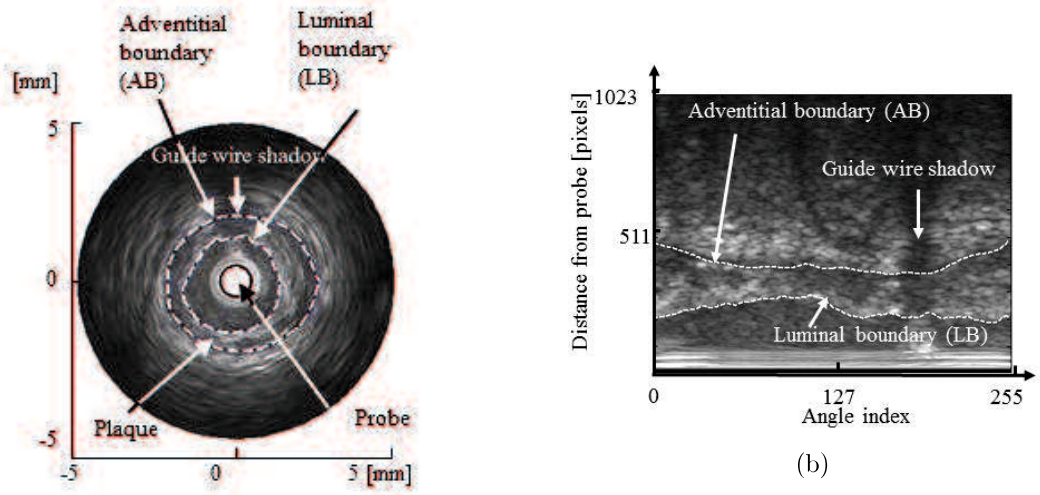

Figure 4.2: The guide wire shadow problem of the IVUS image. (a) The guide wire shadow of the IVUS image in the cartesian coordinate. (b) The guide wire shadow of the IVUS image in the polar coordinate.

IVUS image.

Furthermore, this paper proposes a modified level set method. At the same time a hybrid method based on its modified level set method and the T-S fuzzy inference is proposed for the plaque boundaries detection. Due to the advantages of the level set method as explained in Chapter 1, this paper exploits the level set method. The level set method is modified on several points to obtain better performance.

At the first point, the Gaussian filtering method on the level set methods is substituted with the modified PMD filter for reducing noise. Since there is a high possibility that the image boundary becomes dull after applying the Gaussian filter.

At the second points, the speed function is modified to make the level set method more successful in boundary detection regardless of noise. The weighted image separability is employed to substitute the image gradient in the speed function. The image gradient is commonly used for calculating the speed function in the level set method to detect the image boundary, but it cannot work well in the IVUS image. Since medical images tend to have noise, the noise is filtered by the smoothing filter which causes a blurred edge. The weighted image separability is used to substitute the image gradient because it is robust to noise and dulled edge when detecting an edge. The modified speed function controls the motion of level set contour, and thus the zero level curve of the level set stops around the boundary areas and moves quickly in other areas.

The plaque boundaries on the guide wire shadow region are detected by fuzzy inference. Fuzzy inference is applied in this paper because it has several advantages over the conventional methods in the boundary detection of image, e.g., So-

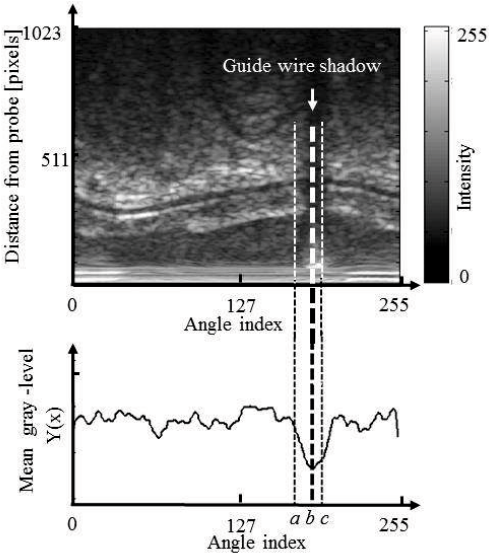

Figure 4.3: Guide wire shadow detection.

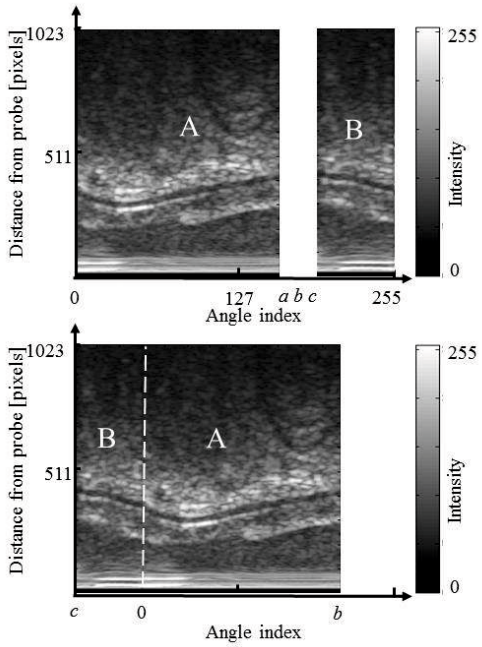

Figure 4.4: IVUS image after ignoring the guide wire shadow.

bels method, Prewitts method, and Roberts method [31]. The fuzzy inference can handle problems of imprecise, noisy, in-consistent and incomplete data sets [29]. Additionally, the T-S fuzzy inference has been successfully applied in many areas. IVUS images have often noise and the plaque boundaries are often missing in several areas. The T-S fuzzy inference is employed to restore the missing boundaries by inference.

The plaque boundary in the guide wire shadow region could be successfully detected by using the newly proposed hybrid boundary detection method. The effectiveness of the present method was also evaluated by the experiments using the real IVUS images.

4.2 Proposed method

This paper presents a hybrid boundary detection method based on the new modified level set and the T-S fuzzy inference for detecting a plaque boundary in the coronary artery. This paper also presents a modified PMD filter to reduce the speckle noise and enhance a coronary plaque boundary by considering the plaque direction in IVUS image.

This chapter is divided into four sections. They are: guide wire shadow detection, modified PMD filter, plaque boundary detection by using the modified level set

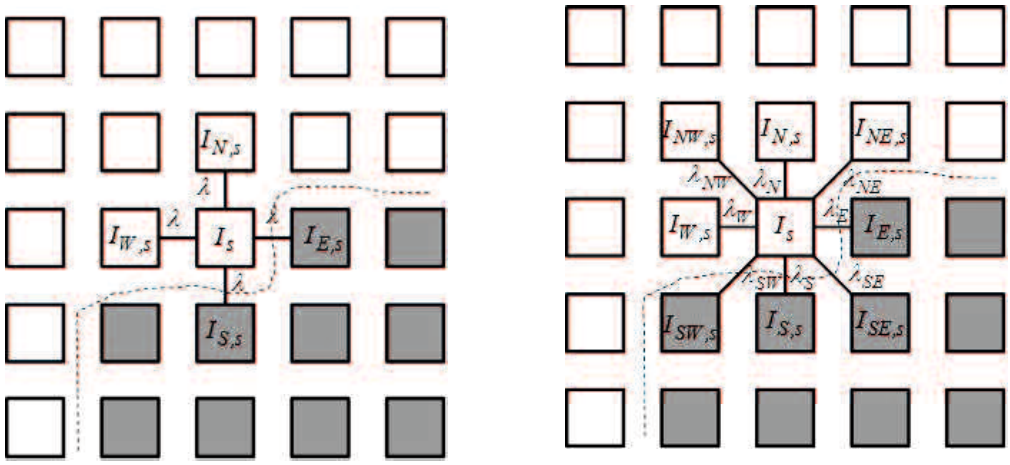

(a) (b)

Figure 4.5: Structure of diffusion directions. (a) The normal PMD filter. (b) The modified PMD filter.

method, and inference of plaque boundary in the guide wire shadow region by using the T-S fuzzy inference.

4.2.1 Guide wire shadow detection

IVUS image has a guide wire shadow and it does not contain any texture information there. Thus the level set method fails to detect the plaque boundary in that region. To overcome this problem, the plaque boundary in the guide wire shadow region is inferred using the plaque boundary information on the left and on the right hand side of the guide wire shadow region.

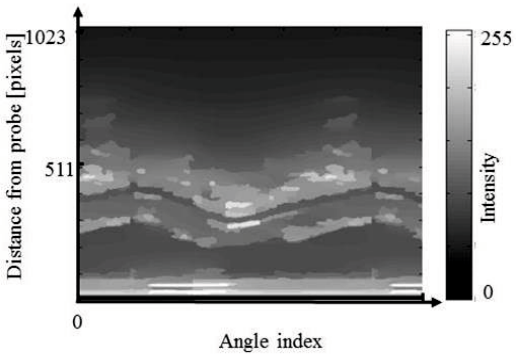

Figure 4.6: IVUS image after applying the PMD filter to Figure 4.4.

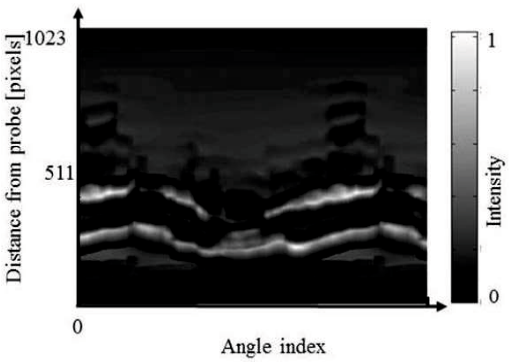

Figure 4.7: Weighted image separability of Figure 4.6.

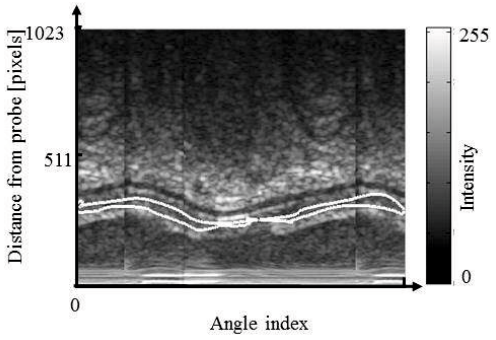

Figure 4.8: Initial contour of the new modified level set.

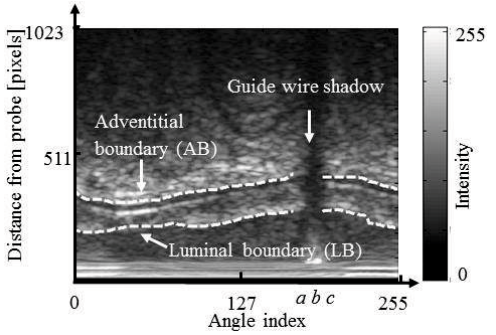

Figure 4.9: Plaque boundary detection results by using the present modified level set method.

In the first step of the present hybrid boundary detection method, the guide wire shadow region is detected. Its procedure is as follows:

1. Convert the B-mode image of Figure 4.2 (a) in the cartesian coordinate system to the polar coordinate system of Figure 4.2 (b).

2. Detect the position of the guide wire shadow. From Figure 4.2 it can be seen that the guide wire shadow is located in the small gray-level area. The mean gray-level of every column of the polar coordinate system is calculated to determine the guide wire shadow. The mean gray-level of every column is given by:

$$Y(x) = \frac{\sum_{k=1}^{N} I(x,y)}{N}, x = 0, 1, 2, ..., 255, \tag{4.1}$$

where N is the number of pixels in one column. The mean gray-level of Equation (4.1) for Figure 4.2 (b) is shown in Figure 4.3. It is observed that the shadow area around the guide wire has a small value of the mean gray-level as shown in Figure 4.3. The location of the guide wire shadow region can be roughly predicted by this mean gray-level of Equation (4.1).

4.2.2 Modified Perona-Malik diffusion filter

Perona and Malik have proposed an anisotropic diffusion filter, which is known as the Perona-Malik diffusion (PMD) filter, to filter noise and preserve the edges of an image. The basic idea of the PMD process is to get an increasingly smoothed image from an original image indexed by a diffusion parameter

The normal PMD filter process as defined in Equation (2.11) represents the four neighboring pixels in North, West, South and East diffusion directions. The structure of diffusion direction for the normal PMD filters is shown in Figure 4.5 (a).

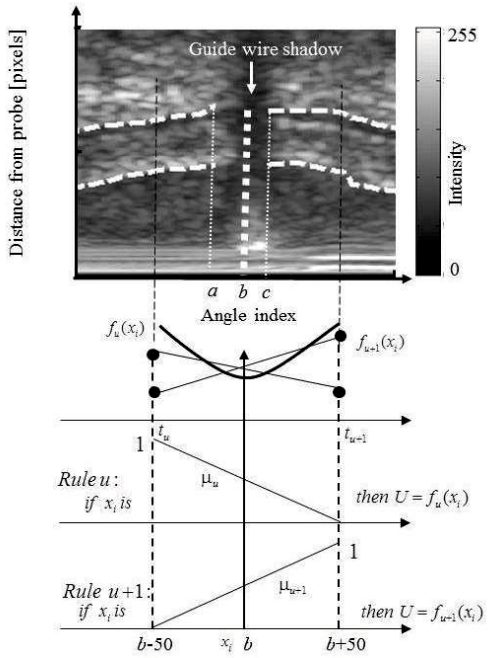

Figure 4.10: Membership functions of the T-S fuzzy inference in the guide wire shadow region.

However, when the normal PMD filter is applied to IVUS image, the coronary plaque boundary cannot be preserved in several areas. By analyzing many experiments, it can be concluded that the diffusion direction and its strength are very important factors in the PMD filter to enhance the edge of image and to reduce noise. If the strength of diffusion is too large, the edge of the image tends to be lost. On the contrary, if the strength of diffusion is too low, the noise of the image cannot be reduced. When the diffusion direction and its strength are set properly, the PMD filter can enhance the plaque boundary and reduce noise. Therefore, the direction and strength of diffusion must be set properly for a good filtering performance.

The modified direction and strength of diffusion of the PMD filter are proposed here by considering the plaque boundary direction in the IVUS image. From Figure 4.2 it can be observed that the boundaries of plaque are horizontal in direction. It means that in order to preserve the plaque boundaries, the diffusion strength in vertical direction should be smaller than that in other directions. In order to consider the direction of plaque boundary, this chapter proposes a new structure for diffusion directions as shown in Figure 4.5 (b).

The modified PMD filter moves in eight directions with different strengths in each direction. By modifying the diffusion process of the normal PMD filter of Equation (2.11) based on the diffusion direction in Figure 4.5 (b), the proposed

iteration formula for diffusion process of the modified PMD filter is given as follows:

$$I_s^{(n+1)} = I_{\mathbf{s}}^{(n)} + \frac{1}{|\phi_s|} \sum_k \lambda_k g(\nabla I_{k,\mathbf{s}}^{(n)}) I_{k,\mathbf{s}}^{(n)}, \tag{4.2}$$

where NW, N through W represent the direction of North West, North, North East, East, South East, South, South West and West, respectively.

4.2.3 Plaque boundary detection by using modified level set method

This paper will modify the distance regularized level set evolution (DRLSE) which is proposed in the reference [15].

In this paper, a new speed function is proposed, and is defined by:

$$g = \left(\frac{1}{1 + \eta_h^w} \right)^q, \tag{4.3}$$

where q is a parameter and η_h^w is a weighted image separability. The weighted image separability is used to detect the candidate of boundary which substitutes the gradient of the image. The following steps explains the procedure of the proposed plaque boundary detection:

1. Detect the guide wire shadow region (angle index between a and c) shown in Figure 4.3.. The positions of a and c are determined by analyzing the real IVUS images which are used for the experiments. Examining the many IVUS images, a and c are set to be $b - 14$ and $b + 8$, respectively. b is a point where the mean-gray level becomes minimum.
2. Merge areas c to 255 (region B) and 0 to a (region A) by placing the latter on the right side as shown in Figure 4.4.
3. Reduce the speckle noise by applying the modified PMD filter to Figure 4.4. The filtering result is shown in Figure 4.6.
4. Calculate the weighted image separability to get Figure 4.7.
5. Calculate the new modified speed function of Equation (4.3).
6. Give the initial contour of the level set, e.g., as shown in Figure 4.8.
7. Calculate the contour evolution by using Equation (2.45) .
8. Calculate the new contour.
9. Repeat steps 8) and 9) until it converges or the maximum number of iterations is reached.

The plaque boundary detected by using the present modified level set is shown in Figure 4.9.

4.2.4 Plaque boundary detection in the guide wire shadow region by using Takagi-Sugeno fuzzy inference

The plaque boundary in the guide wire shadow region is inferred by the T-S fuzzy inference [30]. The plaque boundary is interpolated by the information which is taken from the plaque boundary on the left and on the right of hand side the guide wire shadow region as shown in Figure 4.10. The plaque boundary is inferred by the following fuzzy rules:

$$\text{If } x_i \text{ is } x_i \text{ then } f_u(x_i) = a_u x_i + b_u, \tag{4.4}$$

where A_u is a fuzzy set with the membership function (MSF) $\mu_u(x_i)$, x_i corresponds to the angle index, and is a linear function. Figure 4.10 shows the complementary linear MSFs which are allocated to infer the plaque boundary. The u-th rule is used for approximating the plaque boundary by a linear function in the interval . The plaque boundary is inferred by:

$$\hat{y}_i(x_i) = \mu_u f_u(x_i) + \mu_{u+1} f_{u+1}(x_i), \tag{4.5}$$

The optimum coefficients in the consequent part of the fuzzy rule are determined by using the least square method. It minimizes the following error criterion:

$$E = \sum_i (y_i - \hat{y}_i(x_i))^2, \tag{4.6}$$

where y_i is a plaque boundary that is detected by the newly modified level set method on angle index i. The black dotted lines on the angle interval $[a, c]$ in Figure 4.18 show the plaque boundary inferred by the T-S fuzzy inference.

4.3 Experimental results and discussion

In the experiments, three different IVUS images is used as shown in Figure 4.11, and the proposed method is compared with the method using the normal PMD filter in the reference [12].

By analyzing many IVUS images, the parameters of the modified PMD filter of Equation (4.2) were set as $\lambda_N = \lambda_S = 1$ and $\lambda_W = \lambda_E = \lambda_{NW} = \lambda_{SW} = \lambda_{SE} = \lambda_{NE} = 1.2$. Figures 4.12 (a), 4.13 (a) and 4.14 (a) show the filtering results by the normal PMD filter [24]. Figures 4.12 (b), 4.13 (b) and 4.14 (b) show the filtering results by the modified PMD filter. The plaque boundaries by the modified PMD filter are more clearly enhanced than by the normal PMD filter [24]. It indicates that the modified PMD filter is better than the normal PMD filter in the plaque boundary enhancement.

Figures 4.15 (a), 4.16 (a) and 4.17 (a) show the image separability of image 1, image 2 and image 3 after applying the normal PMD filter. Figures 4.15 (a), 4.16 (a) and 4.17 (a) show the image separability of image 1, image 2 and image 3 after

Table 4.1: RMSEs of boundary detection results for image 1 (μm).

Method	LB	AB
Hybrid boundary detection method (1^{st} experiment)	9.1	20.4
Hybrid boundary detection method (2^{nd} experiment)	9.3	20.0
Hybrid boundary detection method (3^{th} experiment)	9.2	20.1
Hybrid boundary detection method (4^{th} experiment)	9.3	19.9
Hybrid boundary detection method (5^{th} experiment)	9.3	20.1
Hybrid boundary detection method (average)	**9.2**	**20.1**
T-S fuzzy inference [12]	13.7	28.4
T-S fuzzy inference optimized by particle swarm optimization (method in Chapter 3)	12.2	28.5

Table 4.2: RMSEs of boundary detection results for image 2 (μm).

Method	LB	AB
Hybrid boundary detection method (1^{st} experiment)	11.8	24.9
Hybrid boundary detection method (2^{nd} experiment)	12.8	17.3
Hybrid boundary detection method (3^{th} experiment)	12.7	17.6
Hybrid boundary detection method (4^{th} experiment)	12.6	17.2
Hybrid boundary detection method (5^{th} experiment)	12.7	17.5
Hybrid boundary detection method (average)	**12.5**	**18.9**
T-S fuzzy inference [12]	28.0	35.4
T-S fuzzy inference optimized by particle swarm optimization (method in Chapter 3)	23.8	33.2

applying the modified PMD filter. It is seen that the boundaries detected by an experienced medical doctor are located nearer to the center of the area, with high weighted image separability by the proposed method than by the method in the reference [24]. It means that the weighted image separability is able to detect the plaque boundary better on the image after the modified PMD filter. However, the plaque boundaries cannot be detected in several areas as shown in Figures 4.16 (b) and 4.17 (b). It is caused by noise(bright pixels) as shown in Figures 4.13 (a) and 4.14 (a). This problem will be considered in the future.

The proposed hybrid boundary detection method was compared with the methods by using only the T-S fuzzy inference [12], and the T-S fuzzy inference optimized by particle swarm optimization (PSO) (method in Chapter 3).

If the initial contour of the level set is different, the proposed method will produce a different plaque boundary. Therefore the experiment for each image was repeated 5 times with different initial contours. The desired boundaries were decided by an experienced medical doctor by using the difference between image brightness.

The root mean square errors (RMSEs) between the boundaries detected by an experienced medical doctor and the boundaries detected by the proposed hybrid boundary detection method are shown in Tables 4.1, 4.2 and 4.3. The RMSEs of the proposed method are significantly better than those of the previous methods (methods in the reference [12] and Chapter 3) for all images.

Figure 4.19 (a) shows the IVUS image to be processed, and Figure 4.19 (b) shows one of the plaque boundary detection results by the proposed method. The yellow lines show the boundaries detected by an experienced medical doctor and the green

Table 4.3: RMSEs of boundary detection results for image 3 (μm).

Method	LB	AB
Hybrid boundary detection method (1^{st} experiment)	15.3	12.0
Hybrid boundary detection method (2^{nd} experiment)	15.6	13.1
Hybrid boundary detection method (3^{th} experiment)	15.5	21.8
Hybrid boundary detection method (4^{th} experiment)	15.9	12.5
Hybrid boundary detection method (5^{th} experiment)	15.7	12.3
Hybrid boundary detection method (average)	**15.6**	**14.3**
T-S fuzzy inference [12]	20.0	30.2
T-S fuzzy inference optimized by particle swarm optimization (method in Chapter 3)	19.9	40.1

lines show the boundaries detected by the proposed method. The red lines and the blue lines show the boundaries detected by the T-S fuzzy inference [12] and the T-S fuzzy inference optimized by particle swarm optimization (PSO) (method in Chapter 3), respectively.

It can be observed from Figure 4.19 (b) that the boundaries detected by the proposed method are closer to the boundaries detected by an experienced medical doctor than those by the previous methods (methods in the reference [12] and Chapter 3).

4.4 Chapter conclusion

This chapter has proposed a hybrid boundary detection method for detecting a coronary plaque in an IVUS image. It incorporates a newly modified level set method with the Takagi-Sugeno fuzzy inference. The present method was compared with the previous methods (methods in the reference [12] and Chapter 3) and and the boundary detection accuracy of the present method was significantly better.

However, the plaque boundaries cannot be detected in several areas which are caused by noise. This problem will be considered in the future.

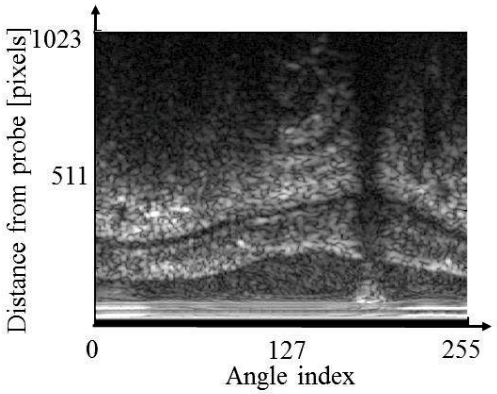

(a)

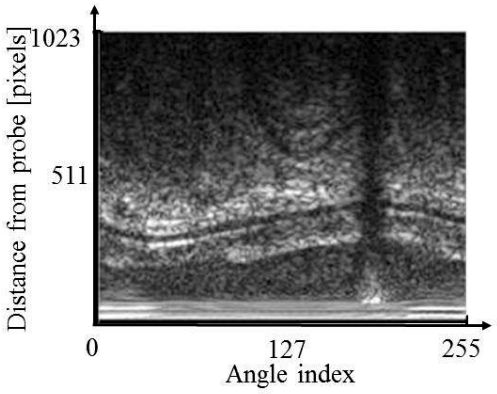

(b)

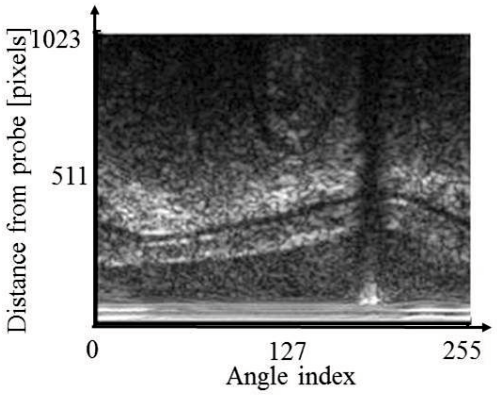

(c)

Figure 4.11: IVUS image in polar coordinate to be processed. (a) Image 1. (b) Image 2. (c) Image 3.

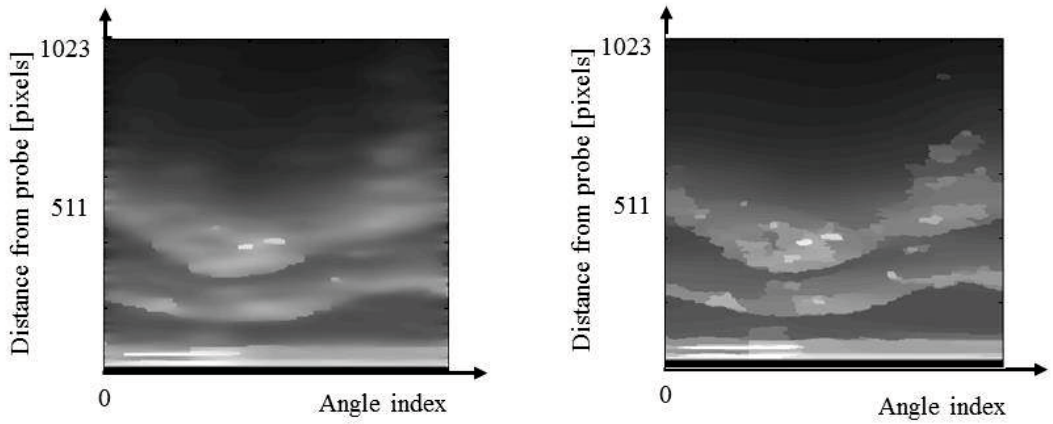

(a) (b)

Figure 4.12: PMD filter results for image 1. (a) The normal PMD filter [24]. (b) The modified PMD filter.

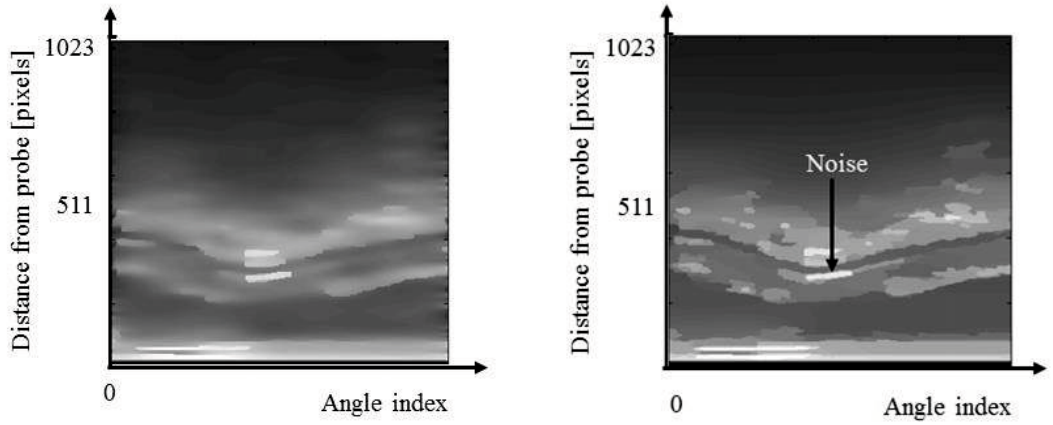

(a) (b)

Figure 4.13: PMD filter results for image 2. (a) The normal PMD filter [24]. (b) The modified PMD filter.

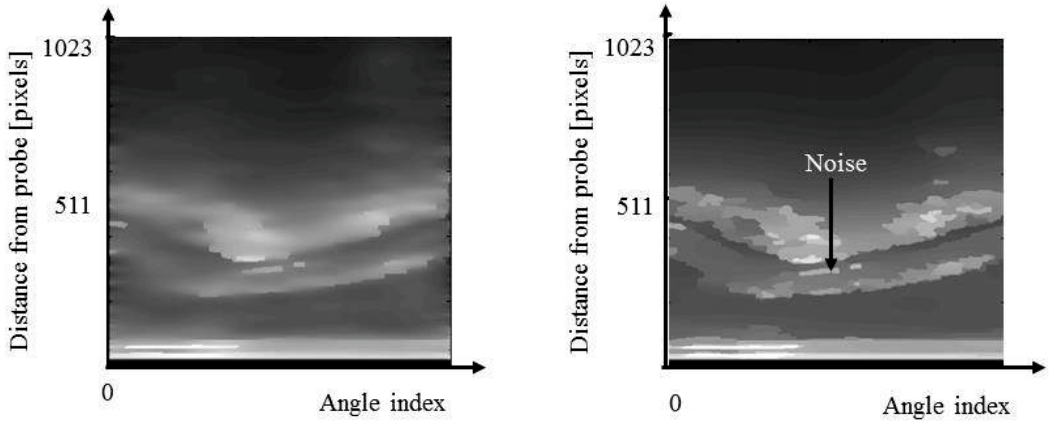

Figure 4.14: PMD filter results for image 3. (a) The normal PMD filter [24]. (b) The modified PMD filter.

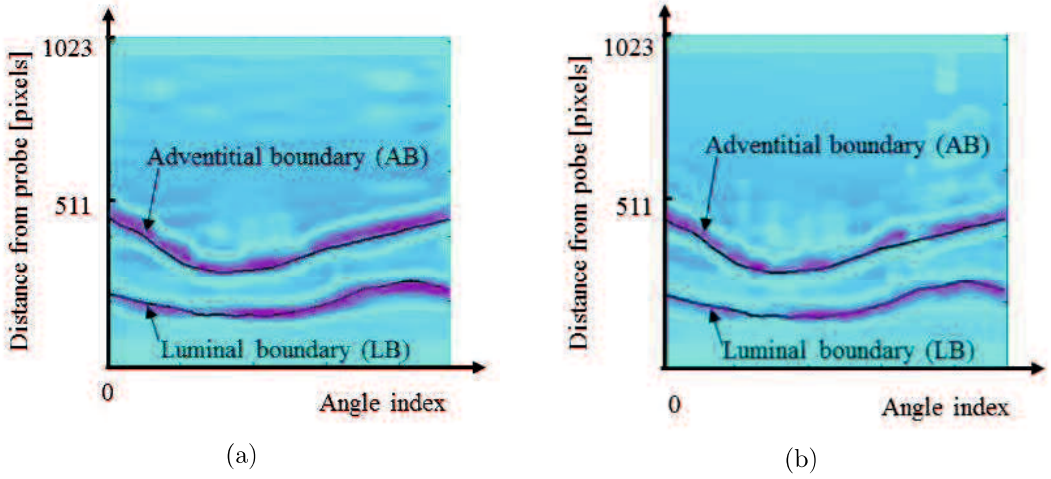

Figure 4.15: Weighted image separability for image 1. (a) The method with the normal PMD filter [12]. (b) The proposed method.

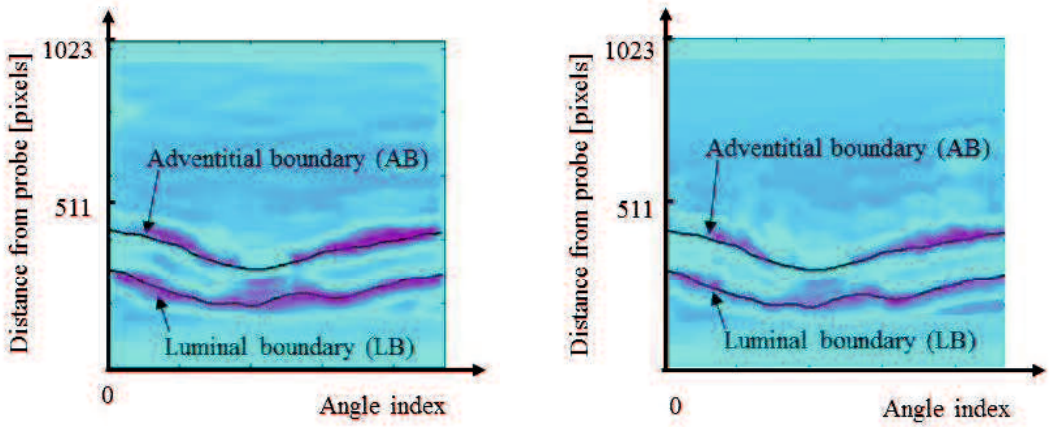

(a) (b)

Figure 4.16: Weighted image separability for image 2. (a) The method with the normal PMD filter [12]. (b) The proposed method.

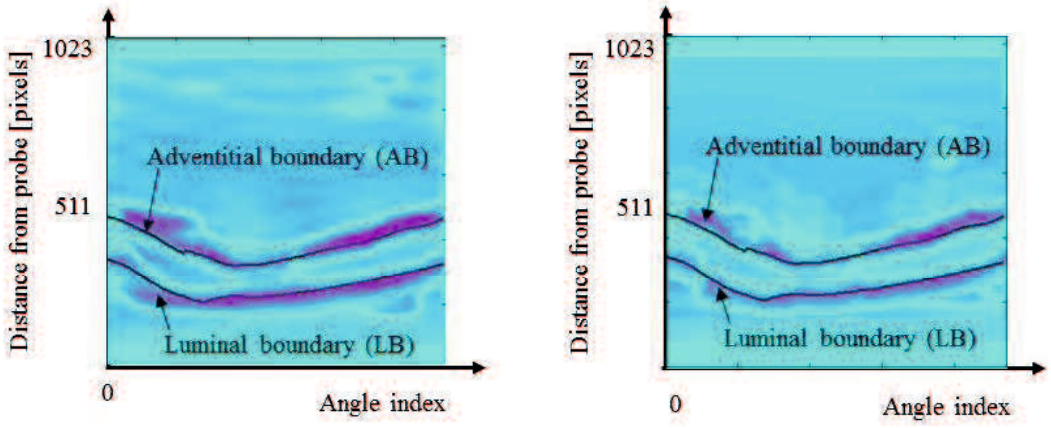

(a) (b)

Figure 4.17: Weighted image separability for image 3. (a) The method with the normal PMD filter [12]. (b) The proposed method.

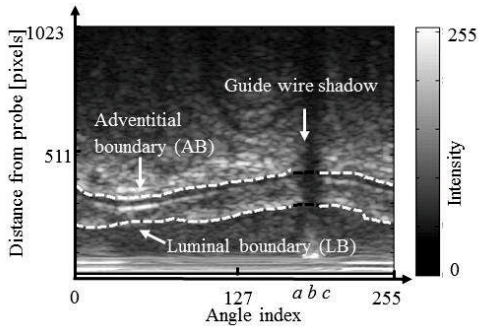

Figure 4.18: Plaque boundary detection results by a hybrid of the newly modified level set method and the T-S fuzzy inference.

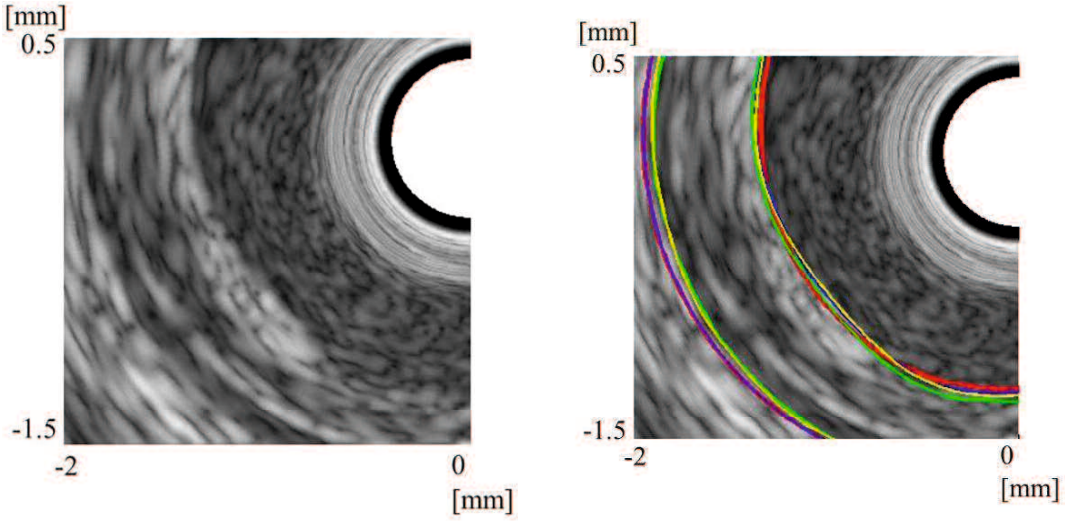

(a) (b)

Figure 4.19: Comparisons of the plaque boundary detection methods. (a) The IVUS image to be processed. (b) The plaque boundary detection results. The yellow lines show the boundaries detected by an experienced medical doctor and the green lines show the boundaries detected by the proposed method. The red lines and the blue lines show the boundaries detected by the T-S fuzzy inference [12] and the T-S fuzzy inference optimized by particle swarm optimization (method in Chapter 3), respectively.

Chapter 5

Texture Analysis and Modified Level Set Method for Automatic Detection of Bone Boundaries in Hand Radiographs

5.1 Background

Rheumatoid arthritis is a chronic and systemic inflammatory disorder that may affect many tissues and organs, but principally attacks synovial joints. Rheumatoid arthritis affects about 1% of the population worldwide and causes premature mortality, disability, and compromised quality of life [49]. It has been demonstrated that early treatment significantly delays joint destruction, disease activity, and functional disability.

Pathological changes in the early stages of a disease are thus extremely important. To give a rheumatoid arthritis diagnosis, a radiograph of the patient's hand is taken as shown in Figure 5.1, and hand bones are analyzed to detect erosion caused by rheumatoid arthritis as shown in Figure 5.2.

Hand bone radiograph analysis, however, is an extremely exhausting and time consuming task for radiologists because the precision required for correct diagnosis is very high. The boundaries of the hand bones firstly need to be detected for the hand bone radiograph analysis. Therefore, an automatic bone boundary detection in the hand radiographs are to be established first.

Boundary detection is a fundamental task in computer vision with wide applications in areas such as feature extraction, object recognition and image segmentation [66]. The boundary detection problem is the problem of finding lines separating homogeneous regions. Active contour model is one of the outstanding methods, and has been extensively exploited for an image boundary detection [13, 14, 15, 16, 65]. It has several desirable advantages over the classical image segmentation methods

Figure 5.1: Rheumatoid arthritis photographed in the hand bone radiograph.

Figure 5.2: The hand bone erosion is caused by rheumatoid arthritis.

as explained in Chapter 1.

Garcia et al. [19] have proposed a fully automatic algorithm for detecting the boundaries of bones in hand radiographs by using an adaptive snake method. However, it does not work well on hand radiographs affected by rheumatoid arthritis, because in this method several initial contours must be decided first and a linear interpolation method is used as shown in Figure 5.3. The snake method with a certain initial contour fails to detect the bone boundary as shown in Figure 5.4.

The level set method, introduced by Osher and Sethian [18], is a highly robust and accurate method for tracking interfaces moving under complex motions. Since the level set method has more advantages over the other methods, it has been widely used for image segmentation.

The level set method however doesn't work well on images with noise. It often leads to either a complete breakdown or a premature termination in the curve evolution process, resulting in unsatisfactory results as shown in Figure 5.5. This is because the speed function cannot properly detect the boundary and its detected boundary is dull even after filtering.

To avoid a premature termination or a complete breakdown in the level set method, this chapter proposes a new modified level set method. Two points in the level set method are modified. The first point is on the filtering and the second point is on the speed function.

In the standard level set method, the Gaussian filter is used for reducing noise.

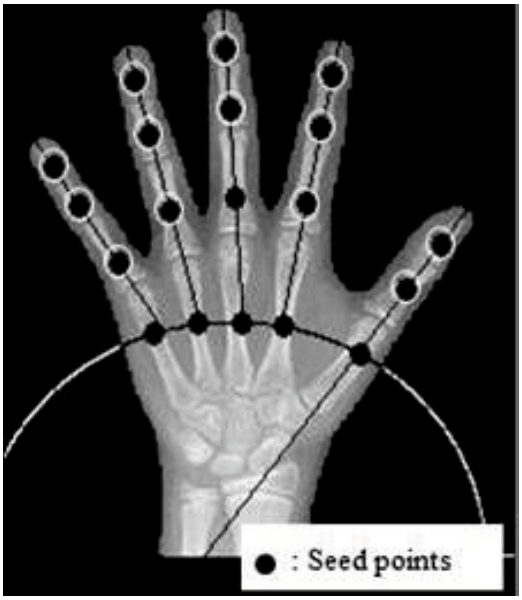

Figure 5.3: Seed points of the adaptive snake method [19]. The initial contours are defined by creating a small contour around each seed point.

Figure 5.4: An example of the failed detection boundary result by a snake method with a certain initial contour.

However, there is a high possibility that the image boundary becomes dull after applying the Gaussian filter. Therefore, the first modification part is that the normal Perona Malik diffusion (PMD) filter [24] is employed to substitute the Gaussian filter. The normal PMD filter not only reduces noise but also effectively enhances the image boundaries. The normal PMD filter is used because the boundaries direction is in all directions.

The second point is that the speed function of the level set method is modified to improve the motion of the level set contour. The modified speed function controls the motion of level set contour, and thus the zero level curve of the level set stops around the boundary areas and moves quickly in other areas.

In hand bone radiographs, the bone boundary detection is very difficult because the pixel intensities of bones and other areas are similar in certain parts, and the hand bone has non-uniform illumination. To solve this problem, an entropy method is employed for a preprocessing, which is one of the texture analysis methods, to distinguish the hand bones and other areas.

The effectiveness of the proposed method is verified through the experiments by applying it to the hand bone radiographs.

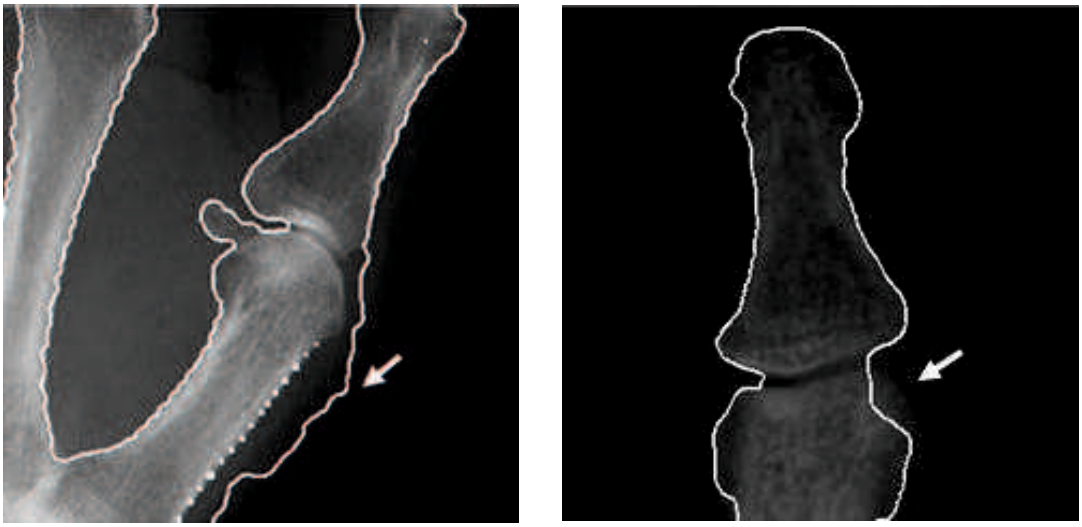

(a) (b)

Figure 5.5: The level set method problems. (a) A premature termination problem. (b) A complete breakdown problem.

5.2 Proposed method

In this chapter, the level set method is modified and it is applied for bone boundary detection in hand radiographs. This chapter further proposes to employ an entropy method-based texture analysis as a preprocessing.

This chapter is divided into two sections. They are: bone texture extraction and modified level set method.

5.2.1 Bone texture extraction

In the first step, the hand bone radiograph is cropped to get a region of concern as of Figure 5.6. In the second step, the cropped radiograph is scanned as in Figure 5.7 and the entropy is calculated for each window as follows:

$$E(i,j) = -\sum_{k=0}^{255} \log_2(p(k)) \tag{5.1}$$

where $E(i,j)$ is an entropy evaluated at the center of the window. The window moves from the top left to the right, then in the next row, until the bottom right of an image. This is called a craster scanning.

The entropy of an image of Figure 5.6 is shown in Figure 5.8. From Figure 5.8 it can be observed that the entropy can distinguish the bone areas and the other areas. The entropy has however a disadvantage that it makes the bones appear to be connected to each other even if they are separated in reality. To overcome this

Figure 5.6: The hand bone radiograph to be processed.

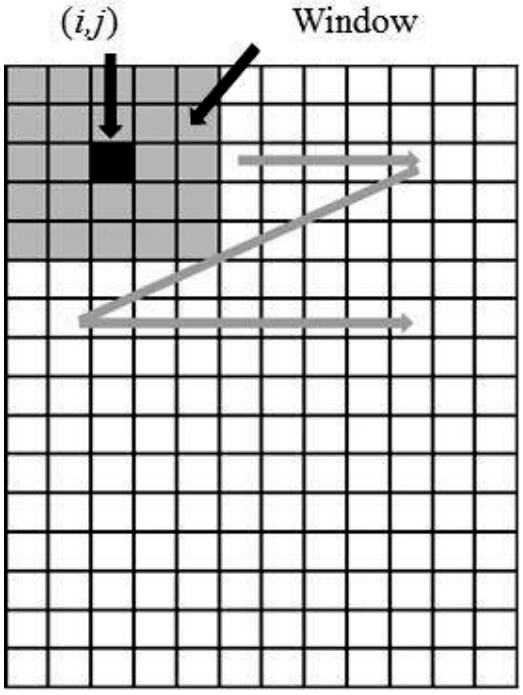

Figure 5.7: Scan of the cropped radiograph by using a moving window.

problem, it is recommended to employ the erosion morphology operation before the entropy of an image is evaluated.

An erosion operation is one of the most basic morphological operations. It adds and/or removes pixels to the image boundaries. The number of pixels added and/or removed from the objects in an image depends on the size and the shape of the structuring element of the erosion morphology operation.

A structuring element of it is a matrix consisting of only 0's and 1's that can have any arbitrary shape and size. The pixels with values of 1 define the neighborhood.

In this paper, the 90 degrees line structure element is used. The length of the line is set to be 11. The result of the erosion morphology applied to Figure 5.6 is shown in Figure 5.9, and the entropy of an image of Figure 5.9 is shown in Figure 5.10. Figure 5.10 is used thereafter.

5.2.2 Modified level set method

In this section, the modified level set method is described, which is applied to the entropy of an image in Section 2.2.3.

The procedure of the modified level set method is summarized as follows:

1. Apply the normal PMD filter to the entropy of an image to smooth it. This

Figure 5.8: The entropy of an image of Figure 5.6.

Figure 5.9: The hand bone radiograph after applying the erosion morphological operation to Figure 5.6.

normal PMD filter substitutes the Gaussian filter in the standard level set method.

2. Calculate the image gradient magnitude $|\nabla I(x,y)|$.

3. Normalize $|\nabla I(x,y)|$ in range [0,1] as follows:

$$G_{norm} = \frac{|\nabla I(x,y)| - \min(|\nabla I(x,y)|)}{max(|\nabla I(x,y)|) - \min(|\nabla I(x,y)|)}. \tag{5.2}$$

4. Calculate the modified speed function which is defined by:

$$g = \exp(-qG^2_{norm}), \tag{5.3}$$

where q is a constant which controls the motion of the contour.

5. Give the initial contour of the level set.

6. Calculate the contour evolution by using:

$$\Delta\phi = \mu div(d_p(|\nabla\phi|)\nabla\phi) + \lambda\delta_\varepsilon(\phi)div(g\nabla\phi/|\nabla\phi|) + \alpha g\delta_\varepsilon \tag{5.4}$$

where δ_ε is a dirac delta function, div is a divergence operator, and g is a speed function.

Figure 5.10: The entropy of an image of Figure 5.9.

Figure 5.11: The result after applying the normal PMD filter to Figure 5.10.

7. Calculate the new contour by using:

$$\phi_{t+1} = \phi_t + \Delta t \Delta \phi_t \tag{5.5}$$

8. Repeat steps (6) and (7) until it converges or the maximum number of iterations is reached.

5.3 Experimental results and discussion

The proposed method is applied to a set of hand bone radiographs. In the experiments, four hand bone radiographs are used. The bone boundary results by the proposed method were compared with the boundaries manually detected by an experienced medical doctor.

As described in Chapter 2, Figure 5.6 is the input image to be processed. After applying the erosion morphological operation to Figure 5.6, Figure 5.9 is obtained. Finally, the entropy of Figure 5.9 is obtained as shown in Figure 5.10. It is seen that Figure 5.10 has a uniform illumination and thus the bone areas and the other areas are softly distinguished.

Figures 5.11 and 5.12 show the entropy of an image after applying the normal PMD filter and the Gaussian filter to Figure 5.10, respectively. It is observed that the normal PMD filter works better than the Gaussian filter.

The values of the standard speed function and the values of the modified speed function for Figure 5.11 are shown in Figures 5.13 and 5.14, respectively. It can be

Figure 5.12: The result after applying the Gaussian filter to Figure 5.10.

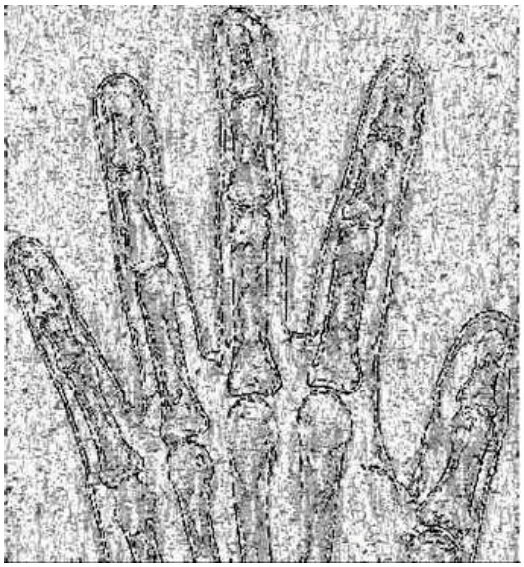

Figure 5.13: The values of the standard speed function for Figure 5.11.

Table 5.1: Numerical evaluation of the bone boundary detection results (pixels).

Data	Hand	Image size	Hausdorff Distance
Data 1	Left Hand	1539 x 1543	35.9
	Right Hand	1500 x 1481	38.7
Data 2	Left Hand	1347 x 1390	43.3
	Right Hand	1341 x 1384	42.0
Data 3	Left Hand	1437 x 1354	39.2
	Right Hand	1398 x 1330	40.6
Data 4	Left Hand	1449 x 1212	61.3
	Right Hand	1425 x 1386	58.5
Average			44.8

seen that the modified speed function clearly shows the bone boundaries better than the standard speed function. The modified speed function can thus avoid a complete breakdown or a premature termination, whilst the standard speed function cannot.

The parameters of the level set of Equation (5.4) were empirically assigned as $\Delta t = 10, \alpha = 1, \mu = 0.2/\Delta t, \lambda = 5$ and $\varepsilon = 1.5$.

Figure 5.15 shows the randomly given initial contour of the level set. The contour of the level set moves gradually with a speed function The level set contour with zero level moves from outside to inside, because the level set function has negative values inside the zero level set contour and positive values outside.

The contour of the level set will stop and converge on the boundary areas because the values of the speed function g on the boundary areas are close to 0.

Figure 5.16 (a) and Figure 5.17 (a) show the radiographs for the left and right hands to be processed, respectively. Figure 5.16 (b) and Figure 5.17 (b) show the

Figure 5.14: The values of the modified speed function for Figure 5.11.

Figure 5.15: Randomly given intial contour of the level set.

detection boundary by an experienced medical doctor for each hand. Figure 5.16 (c) and Figure 5.17 (c) show the detection boundary by the proposed method for each hand. Figure 5.16 (d) and Figure 5.17 (d) show the combined boundary detection results as determined by an experienced medical doctor and the proposed method for each hand. It can be seen from those results that the red lined boundaries manually detected by the proposed method are close to the green lined boundaries detected by an experienced medical doctor. Thus it is safe to conclude that the proposed method is efficient.

The bone boundary detection results are numerically evaluated by Hausdorff distance [67]. The Hausdorff distance between the two curves is defined as the maximum of the distance to the closest point between two curves as follows:

$$e(A, B) = \max(\max_i\{d(a_i, B)\}, \max_j\{d(b_j, B)\}), \tag{5.6}$$

where $A = \{a_1, a_2, ..., a_m\}$ and $B = \{b_1, b_2, ..., b_m\}$ represent the two curves. a_i and b_j are the ordered pairs of x and y coordinates of a point on the curve. $d(a_i, B)$ is the distance to the closest point for a_i to curve B defined by:

$$d(a_i, B) = \min_j \|b_j - a_i\|\} \tag{5.7}$$

The numerical evaluations of the bone detection results by Hausdorff distance are given in Table 5.1. The average of the Hausdorff distance between two curves is 44.8 pixels. Based on the definition of the Hausdorff distance, this means that the maximum error is 44.8 pixels.

The proposed method could detect the bone boundaries quite well for almost all the images that were used. One failed result is shown in Figure 5.18. Figure 5.18 (a) shows the radiographs for the left and right hands to be processed. Figure 5.18 (b) shows the entropy of the input image after applying the normal PMD filtering. It can be seen that the pixel intensities of the hand bone and the pixel intensities of the other areas are mostly similar in some parts. Figure 5.18 (c) shows a hand bone boundary detected by an experienced medical doctor. Figure 5.18 (d) shows the bone boundary detected by the proposed method. Even for a case as difficult as this, the proposed method could detect the bone boundary.

5.4 Chapter conclusion

This chapter has proposed a modified level set method for an automatic detection of the bone boundaries in hand radiographs. This chapter further has proposed to employ an entropy method-based texture analysis as a preprocessing. The proposed method has shown a good detection performance.

The proposed method however could not work well for some cases when the pixel intensities of the bone and those of the other areas are similar.

In future works, the above problem needs to be further considered. A robust method to a variety of image intensities is aimed to develop.

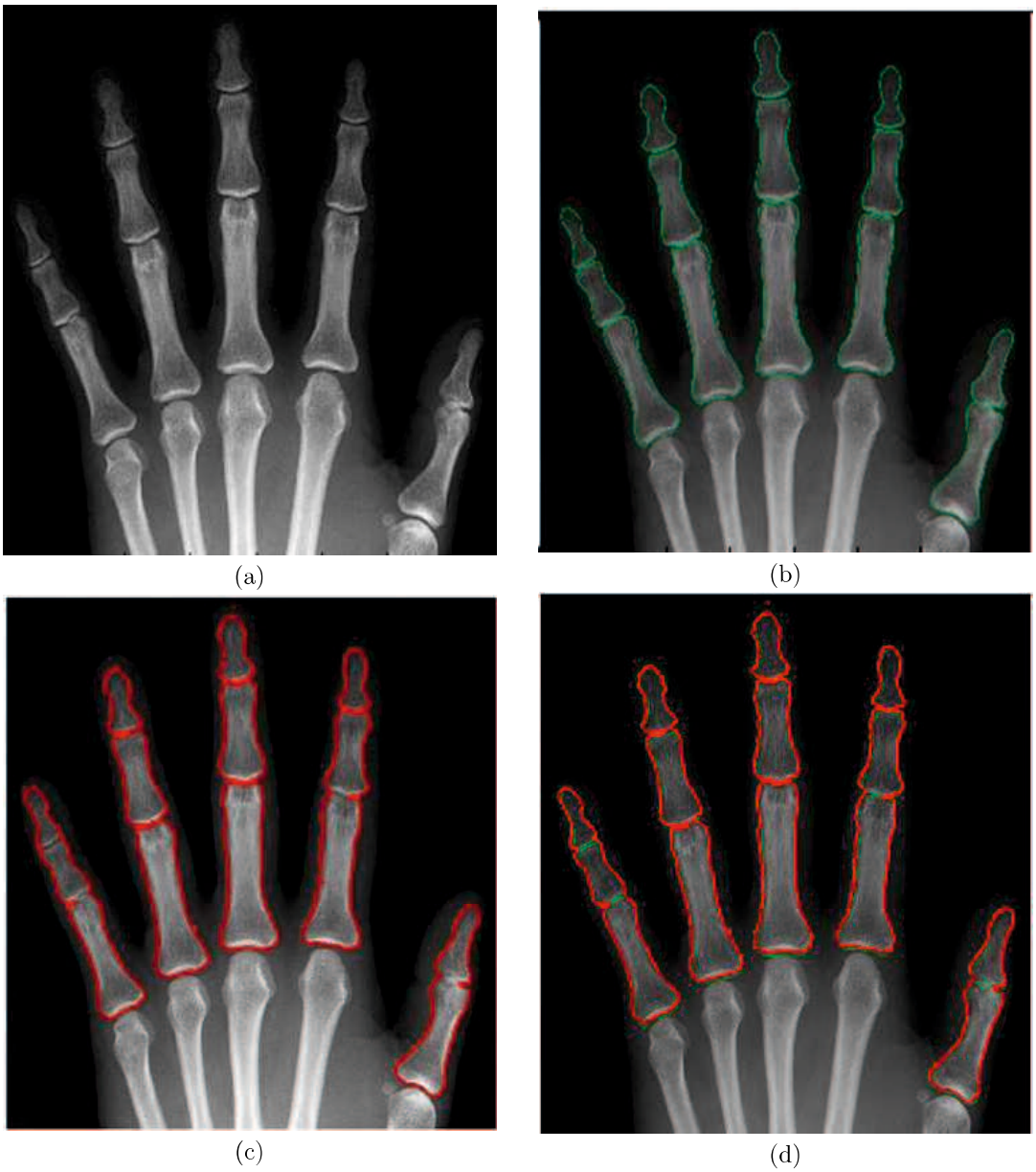

(a) (b) (c) (d)

Figure 5.16: The bone boundary detection results for the left hand radiograph. (a) The left hand bone radiograph to be proccessed. (b)-(d) The red lines and the green lines show the boundaries detected by the proposed method and those manually detected by an experienced medical doctor, respectively.

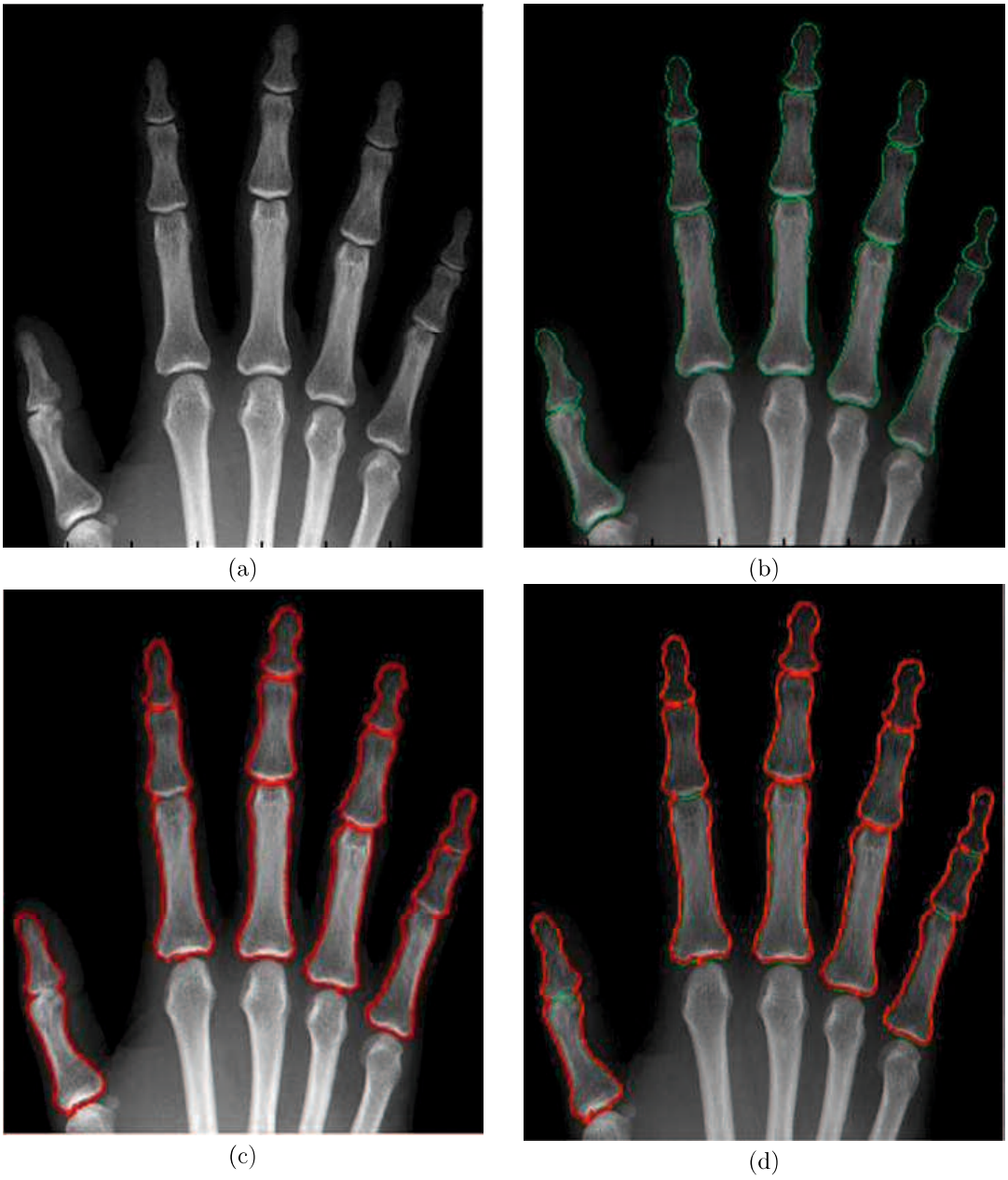

(a) (b) (c) (d)

Figure 5.17: The bone boundary detection results for the right hand radiograph. (a) The right hand bone radiograph to be proccessed. (b)-(d) The red lines and the green lines show the boundaries detected by the proposed method and those manually detected by an experienced medical doctor, respectively.

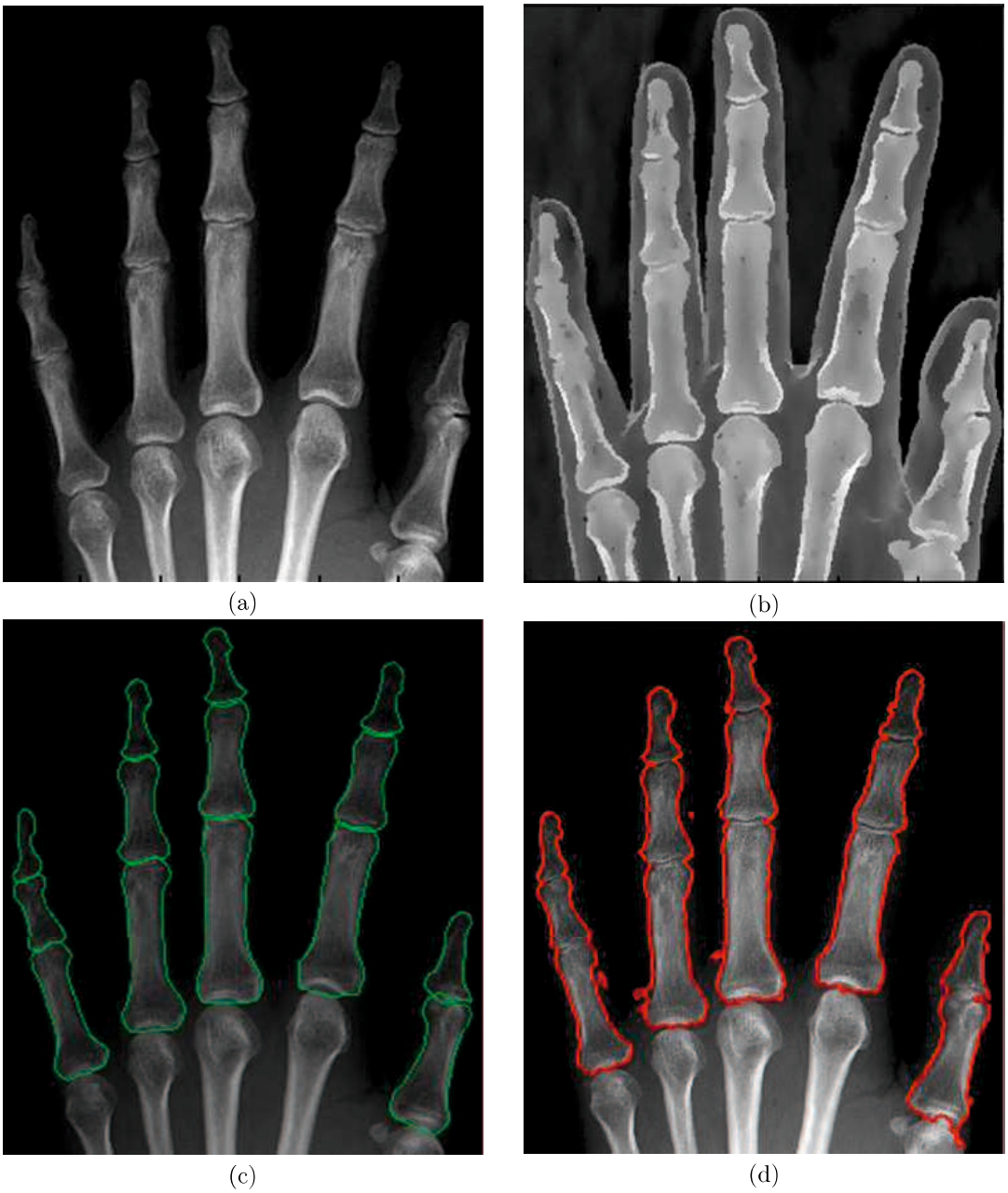

(a) (b)

(c) (d)

Figure 5.18: One comparison of the bone boundary detection for worst case result. (a) The hand bone radiograph to be proccessed. (b) The entropy of hand bone radiograph after applying the normal PMD filter. (c) The bone boundary detected by an experienced medical doctor. (d) The bone boundary detected by the proposed method.

Chapter 6

Conclusion

Medical imaging has developed into one of the most important fields for computerized medical image visualization and computer-aided diagnosis. It also builds a database of normal anatomy and physiology to make it possible to identify abnormalities. Medical images however need to be analyzed to provide information. One of the important subjects in an image analysis is boundary detection which is a type of image segmentation. Since the boundary of a medical image provides valuable information for further medical image analysis and interpretation tasks, accurate medical image boundary detection has become one of the most important and necessary tasks in medical image processing.

This paper has proposed intelligent boundary detection methods for medical images. The proposed methods were applied to IVUS images and hand bone radiograph.

Chapter 3 has presented a method for coronary plaque boundary detection in an IVUS image by combining PSO and the T-S fuzzy inference. It gives better performance than the previous works [11, 48] and the gradient descent method in terms of the detection accuracy. This method also has more advantages over the methods in the references [8, 9, 10]. It works automatically, and does not need any set of training data, seed points, nor initial areas which were given manually in the conventional methods. However, the method in this chapter has several weaknesses. The first weakness is that the proposed method needs to generate seed points to detect coronary plaque boundaries. If the seed points are placed in wrong position, the accuracy decreases. The second weakness is that the coronary plaque boundaries cannot be preserved in several regions after applying the normal PMD filter.

Chapter 4 has proposed a modified PMD filter to improve the performance of the normal PMD filter in Chapter 3. The PMD filter has been modified by considering the plaque direction in IVUS image. Chapter 4 also proposed a hybrid boundary detection method for detecting coronary plaque in an IVUS image. It incorporates a newly modified level set method with the Takagi-Sugeno fuzzy model. This method doesn't require seed points, while seed points is not considered in the method in Chapter 3. The guide wire shadow is considered while it is not considered in Chapter

3. The plaque boundaries outside the guide wire shadow region are detected using modified level set method. The plaque boundary inside the guide wire shadow region are interpolated by using T-S fuzzy inference. The modified PMD filter has significantly better performance than the normal PMD filter. The present method was compared to the previous methods [12] and the method in Chapter 3. The boundary detection accuracy of the present method was significantly better than the previous method and method in Chapter 3.

Chapter 5 has proposed a modified level set method for an automatic boundary detection. The level set method has been modified in the speed function. The speed function of the modified level set method is calculated by the normalization of gradient of image and exponent function, while the speed function of the modified level set method in Chapter 4 is calculated by separability of image. An entropy method-based texture analysis are used for preprocessing. The proposed method in Chapter 5 has detected successfully the bone boundaries in hand radiographs. The method has shown a good detection performance.

It has been shown that the proposed methods are applied successfully to IVUS images and hand bone radiographs. They have been selected to apply to the proposed methods in analysis and display, in the hope that the methodologies may be transferred to other applications. However, the coronary plaque boundaries could not be detected in several areas which are caused by noise. The incorrect bone detection happened in some cases because the pixel intensities of the bone are similar to those of the other areas. In future works, these problem needs to be considered further. Developing a robust method for a variety of image intensities and noisy images is goals for future works.

References

[1] G. Dougherty, "Image analysis in medical imaging: recent advances in selected examples," Biomedical Imaging and Intervention Journal, vol.6, no.3, pp.1-10, 2010.

[2] M. Landgren, "Segmentation of medical images application in Echocardiography and nuclear medicine," Licentiate Theses in Mathematical Sciences, 2014.

[3] Antonidoss and K. P. Kaliyamurthie, "Segmentation from images using adaptive threshold," Middle-East Journal of Scientific Research, vol.20, no.4, pp.489-484, 2014.

[4] J. Guerrero, S. E. Salcudean, J. A. McEwen, B. A. Masri, and S. Nicolaou, "Real-time vessel segmentation and tracking for ultrasound imaging applications," IEEE Transactions on Medical Imaging, vol.26, no.8, pp.1079-1090, 2007.

[5] T. Koga, E. Uchino, and N. Suetake, "Automated boundary extraction and visualization system for coronary plaque in IVUS image by using fuzzy inference-based method," Proceedings of the International Conference on Fuzzy Systems, pp.1966-1973, 2011.

[6] J. C. Buckland-Wright, "Microfocal radiographic examination of erosions in the wrist and hand of patients with rheumatoid arthritis," Annals of the Rheumatic Diseases, vol.43, pp.160-171, 1984.

[7] S. Jansi and P. Subashini, "Optimized adaptive thresholding based edge detection method for MRI brain images," International Journal of Computer Applications, vol.51, no.20, pp.1-8, 2012.

[8] G. M. Ruiz, M. Rivera, and I. A. Kakadiaris, "A probabilistic segmentation method for the identification of luminal borders in intravascular ultrasound images," Proceedings of the IEEE Conference on Computer Vision and Pattern Recognition, vol.45, pp.1-8, 2008.

[9] D. Gil, A. Hernandez, O. Rodriguez, J. Mauri, and P. Radeva, "Statistical strategy for anisotropic adventitia modelling in IVUS," IEEE Transactions on Medical Imaging, vol.25, pp.768-778, 2006.

[10] G. Unal, S. Bucher, S. Carlier, G. Slabaugh, T. Fang, and K. Tanaka, "Shape-driven segmentation of the arterial wall in intravascular ultrasound images," IEEE Transactions on Information Technology in Biomedicine, vol.12, pp.335-347, 2008.

[11] E. Uchino, N. Suetake, T. Koga, S. Ichiyama, G. Hashimoto, T. Hiro, and M. Matsuzaki, "Automatic plaque boundary extraction in intravascular ultrasound image by fuzzy inference with adaptively allocated membership functions," in "Advances in Neuro-Information Processing, Part II," Lecture Notes in Computer Science, vol.5507, pp.583-590, 2009.

[12] T. Koga, S. Ichiyama, E. Uchino, N. Suetake, T. Hiro, and M. Matsuzaki, "Fully automatic boundary extraction of coronary plaque in IVUS image by anisotropic diffusion and T-S type fuzzy inference," in Soft Computing in Industrial Applications, AISC, vol.75, pp.139147, 2010.

[13] L. He, S. Zheng, and L. Wang, "Integrating local distribution information with level set for boundary detection," Journal of Visual Communication Image Representation, vol.21, pp.343-354, 2010.

[14] K. Horbert, K. Rematas, and B. Leibe, "Level-set person segmentation and tracking with multi-region appearance models and top-down shape information," Proceedings of the IEEE International Conference on Computer Vision, pp.1871-1878, 2011.

[15] C. Li , C. Xu, C. Gui, and M. D. Fox, "Distance regularized level set evolution and its application to image segmentation," IEEE Transactions on Image Processing, vol.19, pp.3243-3254, 2010.

[16] C. Li, R. Huang, Z. Ding, J. C. Gatenby, D. N. Metaxas, and J. C. Gore, "A level set method for image segmentation in the presence of intensity inhomogeneities with application to MRI," IEEE Transactions on Image Processing, vol.20, pp.2007-2016, 2011.

[17] P. U. Panchal and K. C. Jondhale, "Image object detection using active contours via level set evolution for segmentation," Journal of Signal and Image Processing, vol.3, pp.97-101, 2012.

[18] S. Osher and J. Sethian, "Fronts propagating with curvature dependent speed: algorithms based on Hamilton-Jacobi formulation," Journal of Computational Physics, vol.79, pp.12-49, 1988.

[19] R. D. L. Garcia, M. M. Fernandez, J. I. Arribas, and C. A. Lopez, "A fully automatic algorithm for contour detection of bones in hand radiographs using active contours," Proceedings of the International Conference on Image Processing, pp.421-424, 2003.

[20] A. Huertas and G. Medioni, "Detection of intensity changes with sub pixel accuracy using Laplacian-Gaussian masks," IEEE Transactions on Pattern Analysis and Machine Intelligence, vol. 8, pp.651-664, 1986.

[21] J. C. Russ, "The image processing handbook," 5th ed. Academic Press, New York, 2006.

[22] P. Soille, "Morphology image analysis: principles and applications," Springer-Verlag, Telos, 1999.

[23] C. Tomasi and R. Manduchi, "Bilateral filter for gray and color images," Proceedings of the 6th International Conference on Computer Vision, pp.839-846,1998.

[24] P. Perona and J. Malik, "Scale-space and edge detection using anisotropic diffusion," IEEE Transactions on Pattern Analysis and Machine Intelligence, vol.12, pp.629-639, 1990.

[25] S. Kim, "Equalized net diffusion (END) in image denoising," Proceedings of the 10th WSEAS International Conference on Applied Mathematics, pp.349-354, 2006.

[26] S. K. Weeratunga and C. Kamath, "Comparison of PDE-based nonlinear anisotropic diffusion techniques for image denoising," Proceedings of the SPIE Electronic Imaging, Image Processing: Algorithms and Systems II, 2002.

[27] G. J. M. Parker and J. A. Schnabel, "Enhancement of anisotropic diffusive filtering of MR images using approximate entropy," Proceedings of the International Society for Magnetic Resonance in Medicine, p.175, 1999.

[28] A. Taki, Z. Najafi, A. Roodaki, S. Setarehdan, R. Zoroofi, A. Konig, and N. Navab, "Automatic segmentation of calcified plaques and vessel borders in IVUS images," Proceedings of the International Journal of Computer Assisted Radiology and Surgery, vol.3, pp.347-354, 2008.

[29] S. Cateni and V. Colla, "Fuzzy inference system for data processing in industrial applications," Fuzzy Inference System-Theory and Applications, pp.978-953, 2012.

[30] T. Takagi and M. Sugeno, "Fuzzy identification of systems and its applications to modeling and control," IEEE Transactions on Systems, Man, and Cybernetics, vol.SMC15, pp.116132, 1985.

[31] S. Arora and Q. A. Kaur, "Modified edge detection technique using fuzzy inference system," Computer Application, vol.44, pp.9-12, 2012.

[32] J. Kennedy and R. C. Eberhart, "Particle swarm optimization," Proceedings of the IEEE Conference on Neural Networks 4, Piscataway, NJ, pp.1942-1948, 1995.

[33] P. Visalakshi and S. N. Sivanadam, "Dynamic task scheduling with load balancing using hybrid particle swarm optimization," International Journal of Open Problems in Computer Science and Mathematics, vol.2, pp.475-488, 1990.

[34] B. N. Potkin, A. L. Bartorelli, J. M. Gessert, R. F. Neville, Y. Almagor, W. C. Roberts, and M. B. Leon, "Coronary artery imaging with intravascular high-frequency ultrasound," Circulation, vol.81, pp.1575-1585, 1990.

[35] V. D. Heijde, "Radiographic imaging: the 'gold standard' for assessment of disease progression in rheumatoid arthritis," Rheumatology, vol.39, pp.9-16, 2000.

[36] C. Prins, L. Botes, F. E. Smit, D. J. Wheatley, and W. M. L. Neethling,"Acute coronary syndromes : pathophysiology and management. Implications for the South African population," Interim : Interdisciplinary Journal, vol.7, pp.198-219, 2001.

[37] webmd.com, "Acute Coronary Syndrome - Topic Overview," http://www.webmd.com/heart-disease/tc/acute-coronary-syndrome-topic-overview.

[38] B. F. Waller, C. M. Orr, J. D. Slack, C. A. Pinkerton, J. V. Tassel, and T. Peters, "Anatomy, histology, and pathology of coronary arteries: a review relevant to new interventional and imaging techniques-part I," Clinical Cardiology, vol.15, pp.451-457,1992.

[39] H. H. Wang,"Analytical models of atherosclerosis," Atherosclerosis, vol.159, pp.1-7, 2001.

[40] K. J. Overbaugh,"Acute coronary syndrome," American Journal of Nursing, vol.109, no.5 , pp.42-52, 2009.

[41] S. E. Nissen and P. Yock, "Intravascular ultrasound novel pathophysiological insights and current clinical applications," Circulation, pp.604-616, 2001.

[42] W. Schaberle, "Ultrasonography in vascular diagnosis," Springer, 2004.

[43] F. Ciompi, C. Gatta, O. Pujol, O. Rodriguez-Leor, J. M. Ferre, and P. Radeva, a,"Reconstruction and analysis of intravascular ultrasound sequences," New Advances in Biomedical Signal Processing, pp.231-250, 2011.

[44] S. D. Pye, S. R. Wild, and W. N. McDicken,"Adaptive time gain compensation for ultrasonic imaging," Ultrasound in Medicine and Biology, vol.18, pp.205-212, 1992.

[45] I. S. Gill and O. Ukimura, "Contemporary interventional ultrasonography in Urology," Springer. p.104. ISBN 978-1-84800-216-6. Retrieved 19 September 2012.

[46] G. Bianchi and R. Sorrentino, "Electronic filter simulation & design," pp.17-20, 2007.

[47] R. C. Gonzalez and R. E. Woods, "Digital image processing," Prentice Hall, Upper Saddle River, NJ 07458, 2002.

[48] R. Kubota, N. Suetake, E. Uchino, G. Hashimoto, T. Hiro, and M. Matsuzaki, "Polynomial-based boundary extraction of plaque in intravascular ultrasound image by using its local statistical information," ICIC Express Letters, vol.2, pp.387-393, 2008.

[49] B. Zielinski, "Hand radiograph analysis and joint space location improvement for image interpretation," Schedae Informaticae, vol.17/18 , pp.45-61, 2009.

[50] N. Umadevi and S. N. Geethalakshmi, "A brief study on human bone anatomy and bone fractures," International Journal of Computer Engineering Science , vol.1, no.3, December 2011.

[51] E. N. Marieb, "Human anatomy & physiology," San Francisco, Daryl Fox, 2004.

[52] webmd.com, "Arthritis basics," http://www.webmd.com/osteoarthritis/guide/arthritis-basics

[53] National Collaborating Centre for Chronic Conditions. "Rheumatoid arthritis: national clinical guideline for management and treatment in adults," London: Royal College of Physicians, February 2009.

[54] V. D. Heijde, "Plain X-rays in rheumatoid arthritis: overview of scoring methods, their reliability and applicability," Baillieres Clin Rheumatol, vol.10, no.3, pp.435-453, 1996.

[55] drsshealthcare.com, "Arthritis," http://drsshealthcare.com/disease/arthritis.php

[56] National health and nutrition examination survey III, " X-ray Procedures Manual," Westat, Inc., Maryland, August 1988.

[57] J. Edmonds and M. Lassere, "Better guidelines to rheumatoid arthritis therapy," Aust N Z J Med, vol.23, no.2, pp.143-145, 1993.

[58] D. Marr and E. Hildreth, "Theory of edge detection," Proceedings of the Royal Society of London. Series B, Biological Sciences, vol.207, no.1167, pp.187-217, 1980.

[59] J. Canny, "A computational approach to edge detection," IEEE Transactions on Pattern Analysis and Machine Intelligence, vol.PAMI-8, no.6, pp.679-698, 1986.

[60] K. Fukui, "Edge extraction method based on separability of image features," IEEE Transactions on Information system, vol.E78-D, pp.1533-1538, 1995.

[61] T. V. N. Rao and A. Govardhan, "Analysis and assessment of surface image texture mechanisms," Journal of Global Research in Computer Science, vol. 3, no.9, pp.6-11, 2012.

[62] J. A. Sethian, "Theory, algorithms, and applications of level set methods for propagating interfaces," In Press:Acta Numerica, August 1995.

[63] R. C. Eberhart and Y. Shi, "Comparing inertia weights and constriction factors in particle swarm optimization, Proceedings of the IEEE Congress on Evolutionary Computation, pp.84-88, 2000.

[64] I. M. Adame, R. J. V. D. Greest, B. A. Wasserman, M. A. Mohamed, J. H. C. Reiber, and B. P. F. Lelieveldt, "Automatic segmentation and plaque characterization in atherosclerotic carotid artery MR images," Magnetic Resonance Materials in Physics, Biology and Medicine, vol.16, pp.227-234, 2004.

[65] M. Li, C. He, and Y. Zhan, "Adaptive regularized level set method for weak boundary object segmentation," Mathematical Problems in Engineering 2012, pp.1-16, 2012.

[66] M. Leordeanu, R. Sukthankar, and C. Smichisescu, "Efficient closed-form solution to generalized boundary detection," European Conference on Computer Vision," LCNS, vol.7575, pp.516-529, 2012.

[67] V. Chalana and Y. Kim, "A methodology for evalution of boundary detection algorithms on medical images," IEEE Transactions on Medical Imaging, vol.16, no.5, pp.642-652, 1997.